ELABORATION ET CARACTERISATION DE QUELQUES DIELECTRIQUES AFORTE PERMITTIVITE AVEC APPLICATION EN MICROELECTRONIQUE :INFLUENCE DE LA STRUCTURE DU RESEAU SUR LEs PROPRIETESELECTRIQUES

Tito Busani

THESE

présentée par

TITO BUSANI

pour obtenir le grade de

DOCTEUR DE L'UNIVESITE JOSEPH FOURIER

(arrêté ministériel du 30 Mars 1992)

Spécialité : Physique des matériaux

ELABORATION ET CARACTERISATION DE QUELQUES DIELECTRIQUES A FORTE PERMITTIVITE AVEC APPLICATION EN MICROELECTRONIQUE : INFLUENCE DE LA STRUCTURE DU RESEAU SUR LEs PROPRIETES ELECTRIQUES

Date de soutenance : 20 Septembre 2006

Composition du jury

Messieurs	R. A. B. Devine	
	P. Gonon	
	J-L. Leray	Rapporteur
	R. Madar	
	P. Muret	
	J. Pelletier	
Madame	A. Vedda	Rapporteur

RESUME DES CHAPITRES
(LANGUE FRANÇAISE)

INTRODUCTION

Si l'on regarde seulement 80 années en arrière, on s'aperçoit que les premiers circuits électroniques réalisant une amplification de signal électrique étaient très simples. Ils se composaient d'éléments discrets comme des tubes à vide, des transformateurs, des résistances, des condensateurs et des fils de connexion. Avec le développement de cette technologie, apparurent les limitations. Par exemple, si les tubes étaient relativement légers, le poids des composants associés et des châssis était important. Les tubes dissipaient beaucoup de chaleur, demandaient un temps de préchauffage d'une à deux minutes et exigeaient de lourdes alimentations de tension continue supérieure à 300 V.

Pendant la 2e Guerre Mondiale, la réduction de la taille, poids et consommation des équipements électroniques militaires devint une nécessité. Avec l'accroissement de la complexité des fonctions ces paramètres devinrent rapidement inacceptables, en particulier sur les instruments embarqués sur avions ou à usage de l'infanterie. Ces impératifs dirigèrent le développement de composants électroniques de plus en plus petits, légers et efficaces.

En 1947, le premier transistor bipolaire (transfert resistor) par pointes à contacts redresseurs fut inventé par Bardeen et Brattain des laboratoires Bell. Suivit en 1949 la publication du classique article de Shockley sur les jonctions PN et les transistors bipolaires. Deux points de contact à la base d'un cristal de quartz triangulaire servant de support étaient réalisés avec 2 bandes de feuille d'or séparées de 50 μm et pressées sur la surface d'un semi-conducteur (germanium). La polarisation en inverse et en direct par rapport à un troisième contact sur le semiconducteur (la base) montrait un effet d'amplification.

La diode et le transistor à l'état solide ouvrirent la voie à la microélectronique moderne. La transition à partir des tubes se fit rapidement. Au fur et à mesure de la création de nouveaux types de diodes et transistors se fit le développement de nouvelles applications. La réduction en poids, taille et consommation fut impressionnante. Des circuits pesant jusqu'à 25 kg furent ramenés à quelques grammes par utilisation des composants à l'état solide. La baisse de consommation et des tensions de polarisation permit un allongement de l'autonomie sur batteries de moindre capacité et tension.

En 1954, Champin développa la première cellule solaire à jonction PN, alors qu'en 1957, Kroemer proposa le transistor bipolaire à hétérojonction, composant potentiellement le plus

rapide. En 1958, Esaki découvrit l'effet de résistance négative sur une diode fortement dopée, aboutissant à la mise au point de la diode tunnel. L'effet tunnel joue un rôle important dans les contacts métal/semiconducteur et dans les propriétés de transport à travers les couches fines isolantes. En 1959, Kilby eut l'idée d'un 'circuit intégré' monolithique et en réalisa plusieurs prototypes comme la fameuse bascule « flip-flop ». Les composants actifs étaient connectés par soudure et isolés par découpe, avec des diodes PN utilisées comme résistances. La même année, Hoerni inventa la technique de diffusion d'impuretés dopantes dans le silicium et les composants à effet de champ planaires utilisant l'oxyde de silicium. Fin 1959, Noyce fabriqua le premier circuit intégré (IC) utilisant des jonctions PN polarisées en inverse pour l'isolation entre transistors et recouvert d'oxyde de silicium gravé pour la prise de contact par évaporation métallique. Ces trois dernières innovations permirent le développement du composant devant jouer un rôle crucial dans les circuits intégrés: le transistor MOSFET (metal-oxide-semiconductor field-effect-transistor), intégré par Kahng et Atalla en 1960. Ce transistor avait une longueur de grille de 20 μm et une épaisseur d'oxyde de grille SiO_2 de 100 nm, obtenu par oxydation thermique. La clé du succès résidait dans les bons contacts sur source et drain obtenus par évaporation d'aluminium à travers un masque. Avec l'accroissement de complexité des IC la technologie passe du N-MOS (transistor MOS à canal N) au C-MOS (MOS N et P complémentaires) permettant la fabrication du composant de base en logique numérique, l'inverseur. Ce concept fut proposé en premier par Wanlass et Sah en 1963. L'avantage de l'inverseur CMOS est de ne consommer du courant que pendant la transition du niveau logique 0 à 1 ou inversement. Le courant de fuite en mode bloqué est très faible. Cette technologie CMOS domine actuellement le marché des IC.

En 1967, un point mémoire à deux composants fut inventé par Dennard, la mémoire dynamique à accès aléatoire (DRAM, dynamis random access memory). Ce point mémoire comporte un transistor MOSFET servant d'interrupteur et un condensateur de stockage de charge. La perte de charge du condensateur nécessite un 'rafraîchissement' périodique et consomme du courant: c'est une mémoire 'volatile', mais qui reste le choix principal de stockage d'information pour son cycle de lecture-écriture rapide. En 1984, Masuoka proposa un point mémoire permanent nommé flash-memory, moins rapide que les DRAM mais présentant une meilleure résistance mécanique que les disques durs. Elles sont utilisées dans le stockage d'information d'appareils alimentés sur piles. A peine dix après la faisabilité du

MOSFET et quelques années après la découverte des DRAM, Intel, une jeune compagnie fondée par Noyce et Moore proposa sur le marché les premiers circuits intégrés avec 100 à 5000 composants sur une même puce: une mémoire 1 kbit et un amplificateur fonctionnant à 750 kHz. Aujourd'hui le nombre de composants sur une puce a été multiplié par 64.000 dans des mémoires de 64 et 128 Mbit (100 millions de composants par puce). La réduction des dimensions a entraîné l'augmentation de transistors par puce (et donc par unité de surface), mais aussi la vitesse des circuits (fréquence d'horloge de quelques GHz sur les ordinateurs de bureau actuels).

Cette réduction des dimensions (en anglais 'scaling-down') est décrite par la loi empirique dite de Moore. Moore prévoyait que d'une génération technologique à l'autre la taille des composants serait divisée par 1,3 et que le nombre de composants sur une puce doublerait tous les 3 ans. Cette tendance s'est vérifiée, avec un léger ralentissement ces dernières années, devant l'accumulation de difficultés techniques croissantes.

Il n'y a pas de doute que le succès de la microélectronique est dû à l'utilisation du silicium et de ses propriétés remarquables. Le silicium de très haute pureté peut être obtenu par croissance de lingots monocristallins d'un diamètre de plus de 30 cm , longs de 1 m et pesant plus de 200 kg. La densité de défauts électriquement actifs dans ce silicium est parfaitement maîtrisée à un taux très faible, connu et caractérisé, ouvrant la possibilité de fabriquer des transistors mono-électron. Le germanium, utilisé à l'origine tient moins bien en température que le silicium (à bande interdite plus large). Le sable, source d'approvisionnement du silicium, est peu coûteux et abondant, peu sujet à la 'fièvre des marchés'.

Mais l'intérêt principal du silicium est sont oxyde, isolant quasi-parfait (résistivité d'environ 10^{16} Ω.cm) et idéal pour la grille des MOSFET. La croissance par oxydation thermique du Si donne des couches de SiO_2 exemptes de défauts et de faible rugosité, même pour des épaisseurs de quelques couches atomiques. L'interface Si/SiO2 est abrupt et les quelques défauts actifs électriquement dus à des liaisons pendantes peuvent être diminués par des recuits en fin de fabrication. Dans l'industrie, il est possible d'obtenir des épaisseurs d'oxyde de grille de moins de 5 couches monoatomiques (1,2 à 1,3 nm), nécessaires au contrôle du potentiel de canal dans les transistors submicroniques.

La diminution des dimensions entraîne la baisse des tensions d'alimentation, de 10 V sur les premiers MOSFETS à 1 V aujourd'hui et 0,7 V prévus en 2012. L'obtention de couches aussi fines exemptes de fuites justifie l'effort mondial de recherche observé sur le sujet.

Aux USA, l'association des industries du semiconducteur, projette la loi de Moore dans l'avenir et définit chaque année des objectifs pour la performance de IC. Ces objectifs sont résumés dans une feuille de route. Par exemple, pour l'année 2012, les prévisions donnent des dimensions critiques de 65 à 32 nm (demi-pas des lignes d'interconnexion), avec des longueurs de grille entre 25 et 18 nm. La règle de maigrissement impose une réduction de l'épaisseur d'oxyde (supposé être de silicium) de 1 nm à 0,6 nm (moins de 4 couches monoatomiques). Il y a là une claire limitation physique. Pour ces épaisseurs, les fuites par ezffet tunnel à travers l'oxyde deviennent significatives. Les travaux de Muller par microscopie électronique couplée à l'analyse des niveaux d'énergie des électrons à l'interface Si/SiO_2, ont montré que les fonctions d'onde électroniques de 0,7 nm de SiO_2 des deux côtés des interfaces (effet tunnel quantique). Pour ces épaisseurs le SiO_2 n'agit plus comme un isolant. En pratique la limite est de 5 monocouches atomiques, en tenant compte d'une rugosité de l'ordre d'une couche monoatomique.

La fin du SiO_2 comme isolant de grille semble atteinte. D'autres limitations à la loi de Moore avaient été identifiées par le passé, mais avaient été surmontés par les améliorations technologiques. Mais la limite physique d'épaisseur de SiO_2 ne peut pas être surmontée et une autre solution doit être trouvée. Une des possibles solutions est l'utilisation de matériaux de constante diélectrique supérieure à celle du SiO_2 de façon à obtenir la même capacité par unité de surface avec une épaisseur plus grande. Au milieu des années 90, l'industrie microélectronique investit fortement dans le développement de ces diélectriques à forte constante diélectrique , high k, et à les intégrer comme isolant de grille de transistor MOS ou de condensateur de stockage. Les objectifs à long terme dépendent du succès de cette recherche.

Le travail exposé dans cette thèse cible les nouveaux matériaux susceptibles d'être intégrés dans les mémoires et les applications à base de transistors MOS. Il est divisé en trois chapitres principaux.

Le premier chapitre traite des contraintes de fabrication des dispositifs. Nous abordons aussi l'état de l'art ainsi que les objectifs industriels à courte échéance. Ce premier chapitre est important pour donner au lecteur les bases technologiques pour comprendre pourquoi des investissements gigantesques sur ces matériaux sont consentis dans l'industrie microélectronique et la recherche associée.

Le second chapitre traite des méthodes de dépôt et croissance des isolants étudiés dans cette thèse. De même nous décrivons au mieux les moyens de caractérisation pour analyser les propriétés physiques et électriques de ces diélectriques. Quelques exemples de matériaux analysés aideront le lecteur à comprendre facilement notre méthode d'investigation scientifique.

Le dernier chapitre est une revue de mon travail publié dans des journaux scientifiques de renommée internationale ou d'exposés dans des conférences majeures. Ce chapitre 3 est sous-divisé en 3 sections. La première et deuxième traite de la compréhension des propriétés des silicates d'aluminium-lanthane et oxides de terre rare obtenus par différentes méthodes de dépôt et récuit. Les résultats ajoutés aux résultats de l'art antérieur donnent un aperçu significatif de notre recherche d'un matériau candidat potentiel comme isolant high k. La dernier section est dédiée aux oxydes de titane et de silicates de titane.

Pour terminer, en conclusion, nous résumons rapidement les objectifs atteints par ce travail et les points encore en cours d'investigation dans le laboratoire.

CHAPITRE I

LOI D'ÉCHELLE: LIMITATIONS PHYSIQUES ET TECHNOLOGIQUES

Ce premier chapitre décrit les différents problèmes rencontrés en microélectronique et qui sont liés, soit au semi-conducteur, soit à l'isolant ou au métal de grille. Il est découpé en trois parties.

Dans la première partie, on présente la loi de Moore, loi d'"échelle" bien connue, comme fondement économique de l'évolution de la microélectronique. Ensuite, on décrit les problèmes physiques et les difficultés économiques à surmonter pour remplir les objectifs de la loi de Moore. Ces problèmes sont bien évidemment caractéristiques de la technologie MOSFET : dissipation de la chaleur, augmentation des courants de fuite, et, bien entendu, travail de sortie.

La deuxième partie de ce chapitre a pour objectif de conduire le lecteur dans les problématiques spécifiques à l'oxyde de grille. Pour cela, après avoir introduit les concepts de diélectrique à forte permittivité (*high-k*) et d'épaisseur équivalente d'oxyde de silicium (EOT comme *equivalent oxide thickness*), on présente une analyse des problèmes les plus significatifs au plan physique et technologique liés à l'introduction de nouveaux matériaux de grille dans la chaîne de production de circuits intégrés silicium.

Enfin, la dernière partie de ce chapitre propose une présentation succincte des principaux et plus attractifs matériaux à forte permittivité étudiés à ce jour.

CHAPITRE II

TECHNIQUES D'ÉLABORATION ET DE CARACTÉRISATION

Ce chapitre est consacré aux techniques expérimentales utilisées lors de ce travail. L'objectif est de donner une vision générale de ces techniques en donnant leur principe, la manière de les utiliser et de les exploiter, et d'en extraire les informations utiles. Ce chapitre comporte deux parties, la première portant sur les techniques d'élaboration et le second sur les moyens de caractérisation.

Les procédés d'élaboration utilisés pour déposer ou faire croître les oxydes de grille ont été mis en œuvre dans une salle blanche niveau 3 du Centre de Haute Technologie des Matériaux à Albuquerque. Les outils utilisés sont décrits de manière détaillée, de même que les principaux paramètres expérimentaux accessibles lors de l'élaboration des couches minces d'oxyde. En particulier, les avantages et les limitations des techniques de dépôt et de recuit choisis dans cette étude sont argumentées et précisées.

Les techniques de caractérisation nombreuses et variées utilisées pour analyser les films font l'objet de la seconde partie. Toutes ces techniques ont été personnellement maîtrisées, sauf exceptions mentionnées dans le texte. Pour tous les outils de caractérisation utilisés, des exemples réels et concrets ont été donnés. Ces exemples font référence à la fois à la technologie Si/SiO_2 et aux technologies Si/high-k et ils sont directement reliés aux résultats expérimentaux que nous avons obtenus.

CHAPITRE III

RESULTATS

La première partie de ce chapitre est focalisée sur l'étude des alliages $LaAlO_3$ comme possibles candidats pour remplacer l'oxyde de silicium. Les travaux publiés sur le sujet sont nombreux, et les résultats sont divergents. On présente les différents procédés utilisés pour déposer l'oxyde et pour le caractériser. Enfin, on met en relation les propriétés électriques et physiques des oxydes étudiés, tout en essayant de comprendre leur comportement en relation avec les conditions de dépôt.

La deuxième partie est consacrée aux deux oxydes de terres rares Pr_2O_3 et Nd_2O_3. Ces oxydes sont de bons candidats comme des oxydes à forte permittivité. On décrit d'abord comment ils ont été déposés et caractérisés. On procède ensuite à une analyse pour montrer comment les propriétés électriques de ces oxydes sont liées à leur structure cristalline. De cette façon, il est possible de comprendre et de prévoir dans le détail le comportement physique et électrique des oxydes de terres rares.

La troisième partie est dédiée à l'oxyde de titane (TiO_2) et aux pseudo alliages TiO_2-SiO_2. On décrit succinctement les méthodes avec lesquelles ces oxydes ont été déposés et comment ils ont été caractérisés, et on montre l'importance de ces oxydes en microélectronique. On analyse tout d'abord les différentes phases de l'oxyde de titane, puis, en se référant aux travaux antérieurs, on cherche à comprendre les mécanismes physiques déterminant le comportement de tels oxydes et en particulier les problématiques liées au changement de densité par rapport à la variation de concentration de Ti dans les alliages mixtes TiO_2-SiO_2.

CONCLUSION

La microélectronique moderne nécessite une connaissance poussée des propriétés des matériaux quelle utilise en couches ultra-minces. Les objectifs ambitieux tels qu'établis par la 'loi de Moore' prévoient la réalisation de transistors et composants à l'échelle du nanomètre. Deux sortes de matériaux sont du plus haut intérêt : les métaux et les isolants. Le problème crucial qui se pose aujourd'hui est le remplacement du SiO_2 comme isolant de grille des transistors MOS. De tels isolants doivent avoir une forte constante diélectrique ('high k' en anglais). Nus montrons le grand nombre de paramètres jouant un rôle dans les procédés technologiques et les corrélations éventuelles entre certains de ces paramètres. Pour les isolants de grille, les défis technologiques se classent dans 3 catégories: en premier, ils doivent avoir une constante diélectrique élevée, en second, une bande interdite optique élevée pour éviter l'injection d'électrons dans le Si, en troisième une bonne stabilité vis-à-vis du Si. Ces contraintes peuvent être étudiées séparément mais sans jamais oublier leur possible interaction mutuelle. Pour un isolant en contact avec le Si, nous avons essayé de comprendre comment la structure de l'oxyde était corrélée à ses propriétés physiques et optiques et comment ces corrélations pouvaient influencer les applications en microélectronique. Il est évident que cette analyse et méthodologie peut être étendue à d'autres matériaux.

Nous avons étudié plusieurs oxydes que nous avons déposé ou fait croître par différentes techniques : méthodes assistées par plasma comme le PECVD), anodisation plasma ou pulvérisation cathodique. De plus, l' évaporation par canon à électrons et l'oxydation thermique ont aussi été utilisés. Nous avons travaillé en salle blanche de classe 1000 et atmosphère contrôlée pour minimiser la contamination de la surface des échantillons réduisant ainsi les risques de non reproductibilité des dépôts.

La caractérisation des oxydes a été menée avec une gamme étendue de méthodes et appareillages. Ces techniques sont essentielles pour déterminer les paramètres structurels et physiques fondamentaux des oxydes étudiés. La struxture des oxydes a été déterminée par, diffraction et réflexion X, EDS, FTIR, AFM, XPS et RBS. Pour compléter par les variables macroscopiques (constante diélectrique et indice de réfraction) qui sont obtenues par mesures électriques et ellipsométriques.

L'oxyde ternaire $LaAlO_3$ a été choisi pour sa constante diélectrique et sa stabilité avec le Si. Nous avons prouvé que la phase de haute constante diélectrique (ε=28) n'existe que pour les oxydes cristallins. Bien que les polarisabiltés ioniques de la phase amorphe et de la phase cristalline soient très proches, la grande différence des ε est due à la différence du volume moléculaire. Le $LaAlO_3$ en phase cristalline est plus dense qu'en phase amorphe. L'inconvénient est la température élevée de formation, au dessus de 800°C. Les essais d'obtention de la phase cristalline ont montré que les recuits au dessus de 700°C détériorent l'interface SI/oxyde et dégradent les propriétés électriques de la structure MOS. C'est une limitation sérieuse de ces oxydes pour des applications MOSFET.

Les oxydes de terres rares Pr_2O_3 et Nd_2O_3 sont aussi obtenus en phase amorphe ou cristalline. A 900°C, l'interaction oxyde/Si est faible. La constante diélectrique de la phase amorphe est nettement plus faible qu'en phase cristalline. Celle-ci prend deux formes différentes: cubique et hexagonale. La formation de l'un ou l'autre dépend du numéro atomique de la terre rare. La relation entre densité et structure est mise en lumière ainsi que l'influence sur les propriétés macroscopiques de l'isolant. La formation et la stabilité de ces phases dépend du procédé de dépôt, point très important dans la fabrication microélectronique.

Des oxydes mixtes SiO_2-TiO_2 ont été déposés avec différentes concentrations en Ti. Mais auparavant nous avons caractérisé l'oxyde de titane stoechiométrique. A hautes températures il présente une instabilité vis-à-vis du Si et une anisotropie finie dans ses propriétés macroscopiques. Sous la forme amorphe, il a un ε de 33. Les phases cristallines rutile et anatase sont très sensibles au traitement thermiques en dessous de 200°C. Pour des températures inférieures à 600°C, les oxydes mixtes n'ont pas de phase TiO_2 cristalline ou amorphe SiO_2, ni de ségrégation du TiO_2. La constante diélectrique et l'indice de réfraction ont une variation linéaire entre un maximum (TiO_2 pur) et un minimum (SiO_2 pur). Par exemple, l'alliage $Ti_{0.5}Si_{0.5}O_2$ a un ε de 27 avec une bande interdite optique estimée à 6.25. Mais un recuit de cet alliage au dessus de 600°C donne lieu à la ségrégation SiO_2 et TiO_2 ainsi que la probable formation nano-cristaux de rutile et/ou anatase.

Ainsi le remplacement du SiO_2 n'est pas impossible mais s'avère difficile. Nous avons discuté de ce problème et des compromis à faire et compris nettement que :

a) un oxyde de grille amorphe d' ε supérieur à 25 ne peut pas être obtenu à l'heure actuelle.

b) la plupart des candidats à ε élevé forment une couche interfaciale de SiO_2 à la transition oxyde/Si, ce qui est désastreux pour des EOT (épaisseur équivalente de SiO_2) inférieures à 1 nm. Imaginons deux oxydes l'un avec ε =12 et l'autre avec ε =25. Le premier est réalisable industriellement à l'heure actuelle. Traçons l' EOT en fonction de l'épaisseur réelle de l'oxyde (figure I). Le trait noir correspond à l'absence de couche intermédiaire, le bleu, vert et rouge à 0.1, 0.2, 0.3 nm d'épaisseur de couche intermédiaire de SiO_2. Nous constatons que pour les besoins prévisibles en 2016, à savoir un EOT de 0.45 nm, une couche parasite interfaciale de seulement 0.3 nm impose une épaisseur physique de moins de 2 nm pour ε =25 et de moins de 1 nm pour ε =12. Cette dernière épaisseur semble infaisable dans un environnement industriel avec ses contraintes de reproductibilité. Il est donc indispensable de viser des matériaux à très haute constante diélectrique pour relâcher la contrainte sur l'épaisseur et la couche interfaciale.

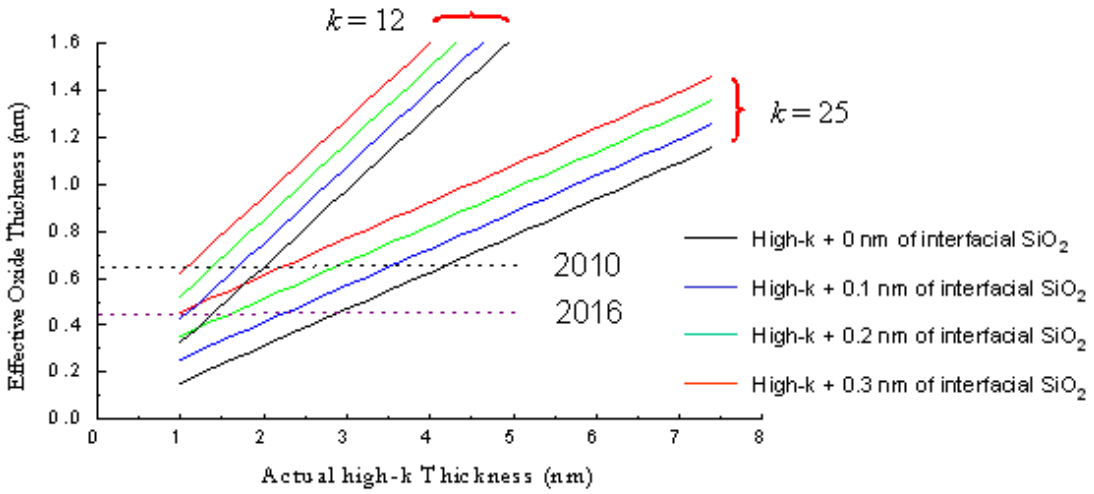

Figure I. *EOT versus the real oxide thicknesses. Different lines refer to different interfacial SiO_2 thicknesses at the interface high*-k/Si:

L'industrie de la microélectronique est consciente de ce problème. John Mestermacher, directeur commercial des matériaux innovants à Air Products, fait remarquer que les prévisions d'introduction des diélectriques à base d'hafnium dans les nœuds 65 sont retardées au nœud 45 nm ou inférieurs. En octobre 2005, David Lammers d'Intel disait: 'Il est fort improbable que nous soyons en mesure d'introduire des oxydes high k dans le nœud

45 nm'. Paul Angelo, responsable du développement 45 nm à IBM déclare: 'la dispersion de tension de seuil est mortelle…la communauté des chercheurs en matériaux high k doit obtenir des améliorations conséquentes avant que nous puissions les introduire en production'.

Nous espérons que ce travail aura contribué à l'amélioration de la connaissance des propriétés de ces oxydes à très haute permittivité.

INTRODUCTION

If one goes back only 80 years, the first electronic circuits enabling amplification were fairly simple. They were composed of independent elements such as vacuum tubes, transformers, resistors, capacitors, and wiring. Component limitations were soon identified as this technology developed. For example although vacuum tubes were lightweight, associated components and chassis were quite heavy. The vacuum tubes generated a lot of heat, required a warm-up time from 1 to 2 minutes, and therefore required hefty power supply voltages of 300 volts dc or more.

During World War II, the need to reduce the size, weight, and power consumption of military electronic equipments became important because of wide spread requirements for communication equipment. As systems became more complex, their size, weight, and power requirements rapidly increased until it was considered unacceptable, especially in aircraft and for infantry personnel. These factors drove the development of smaller, lighter, and more efficient electronic circuit components.

In 1947, the first point-contact transistor was invented by Bardeen and Brattain in the Bell Laboratories. This was followed by Shockley's classic paper on p-n junctions and bipolar transistors in 1949. Two point contacts at the bottom of a triangular quartz crystal were made from 2 strips of gold foil separated by 50 μm and pressed onto a semiconductor surface. The semiconductor used was the germanium. With one gold foil contact forward biased positively respect to the third terminal and the other gold foil reverse biased, transistor action was observed: the input signal was amplified. The solid-state diode and the transistor opened the door to microelectronics. The transition from vacuum tubes to solid-state devices took place rapidly. As new types of transistors and diodes were created, they were adapted to circuits. The reductions in size, weight, and power use were impressive. Circuits that earlier weighed as much as 25 kg were reduced in weight to just a few tens of grams by replacing bulky components with the much lighter solid-state devices. Power consumption also dropped significantly giving longer autonomy for battery powered circuits.

In the 1954, Champin developed the first solar cell using a p-n junction whilst in 1957, Kroemer proposed the heterojunction bipolar transistor, which potentially are the fastest semiconductor devices. In the 1958 Esaki observed negative resistance characteristics in a heavily doped p-n junction, leading to the discovery of the tunnel diode. The tunnel diode and the associated tunneling phenomenon are important for ohmic contacts and carrier transport through thin layers. In 1959, Kilby created the idea of a monolithic "integrated circuit" and by the end of that year he constructed several examples, like the famous flip-flop. Components were connected by hand- soldered wires and isolated by shaping and p-n diodes used as resistors. In the same year, Hoerni invented a technique to diffuse impurities into silicon to build planar transistors using SiO_2 as the gate insulator. At the end of 1959 Noyce developed the first integrated circuit (IC) planar transistor using a back-to-back p-n junction for isolation, a diode-isolated silicon resistor and SiO_2 as insulator with metal contacts evaporated on the surface. These last 3 novel inventions were the first step in the discovery of the most important device for advanced integrated circuits: the MOSFET (metal-oxide-semiconductor field-effect transistor) which was reported by Kahng and Atalla in 1960. The device had a gate length of 20 μm and a 100 nm SiO_2 gate oxide thermally grown on silicon. The two keyholes were the source and the drain contacts and the connection were obtained by evaporating aluminum using a mask for the pattern. As the complexity of the IC increased, technology has moved from the classic nMOS (n-channel MOSFET) to CMOS (complementary MOSFET) that employs both nMOS and pMOS (p-channel MOSFET) in order to form the logic component. The CMOS concept was proposed for the first time by Wanlass and Sah in 1963. The advantage of the CMOS technology is that logic elements draw significant current only during the transition from one state to another (from 0 to 1 using digital terminology) and draw very little current between, resulting in very low power consumption. This technology is today the dominant technology for ICs.

In 1967, an important 2 element circuit, the dynamic random access memory (DRAM) was invented by Dennard. The memory cell contains one MOSFET that serves as a switch to charge or discharge a storage capacitor. The DRAM is a volatile memory and consume relatively high power, but is still today the main choice among various semiconductor memories. In 1984, Masuoka discovered another important and widely used memory device: the flash memory. Flash memories offer fast read acces time (though not as fast as volatile

DRAM) but they are non-volatile. They also offer a better shock resistance than hard disks These characteristics explain the popularity of flash memories for applications such as information storage in battery-powered devices. Only ten years later than the discovery of the MOSFET and few years later than the discovery of the DRAM, Intel, a new company founded by Noyce and Moore, appeared on the market with the first large scale integrated device with 100 to 5000 components all on one chip: a 1 kilobit memory and a microchip working at 750 kHz. Since then, continuous evolution has increased the number of device components on a chip by a factor of 64,000 to a fully integrated 64 and also 128 megabit memory chip in which there are more than 100 million electronic components. Scaling down of the device size not only increased the number of the transistors per chip (and per surface unit) but also the speed of the circuits up to a few GHz in today's personal computers.

The scaling down process is well described by the "Moore's law". Moore predicted in the 1965 that for each new generation of memory chip and microprocessor unit on the market, the device size should reduce by 33, the chip size would increase and the number of components on a chip would quadruple every 3 years. So far this trend has shown no sign of stopping even though the increase has been slightly slower due to technological problems.

It is unquestionable that the success of microelectronics is due to the use of Si because of its physical properties. Silicon can be grown in single crystals more than 1 m long and 30 cm across, weighing approximately 200 kg. The purity of the crystals and the number of the electrically active defects are well controlled. The number of atomic crystal defects in sub-micrometer size MOSFETs is now limited to individual centers and these may be identified, characterized and counted, so that even single-electron transistors are possible. Although germanium was the initial semiconductor used to demonstrate transistor action, silicon has a wider band gap which means that silicon devices can operate at higher temperature. Inasmuch as silicon is a primary constituent of ordinary sand, it is a very inexpensive and abundant element. Thus, silicon is a low cost source material which is normally not subject to the "stocks market madness".

The very special feature, and perhaps the most important, of silicon, which makes it the semiconductor of choice for MOSFETs, is its oxide. Silicon dioxide (SiO_2) is an almost perfect insulator with a resistivity of ~ 10^{16} Ωcm. Insulating films of SiO_2 grown thermally on silicon are smooth with no holes throughout the thickness range even down to single atomic layers. The interface with silicon is abrupt and the active defects at the interface,

resulting from incomplete bonds can be removed using a post annealing process. In the commercial labs, it is now possible to produce MOSFETs and integrated circuits with gate oxides less than 5 layers thick (1.2-1.3 nm). Such thin films are required to maintain the current response of the transistor to lower voltages at the gate electrode resulting from device scaling.

Manufacturers need to lower the power supply voltages for individual components, if they are going to integrate even more devices onto a chip. The first MOSFET worked with a supply voltage of more than 10 V, 10 times higher than what it is used today and 15 times higher than the expected 0.7 volts for 2012. Development of "non-leaky", ultra-thin oxides for future devices now justifies the worldwide effort to make these almost atomic layer thickness gate oxides.

The Semiconductor Industry Association in the United States extrapolates Moore's law into the future and sets yearly targets for the performances of ICs. These targets are summarized in a roadmap. For the year 2012, the roadmap indicates that critical device size decreases from 65 nm to 32 nm, with a physical gate length from 25 nm to 18 nm. Consequently, the gate oxide (assumed to be SiO_2) thickness must be reduced from 1 nm (5 atomic layers) to 0.6 nm (less than 4 atomic layers). Clearly, there is a limit to this scaling down because the SiO_2 gate oxide is tending to zero thickness. Furthermore, for a thickness of less than 4 atomic layers of silicon atoms leakages currents through the oxide are significant. Muller, using an electron microscope in combination with a spectroscopic analysis of electron energy levels at the Si-SiO_2 interface showed that the electronic wavefunctions penetrate through 0.7 nm of SiO_2 from both interfaces (i.e. quantum tunneling occurs). This means that SiO_2 no longer acts as an insulator for that thickness. In practice the limiting gate oxide thickness must be a slightly larger than the theoretical limit, around 5 atomic layers of silicon, because the interface is rough at an atomic level.

The end of the road for SiO_2 as a gate insulator is now expected and has already began. In the past, various technological limitations to Moore's law have been predicted and all of these have been overcome by new developments, leading to silicon-based materials of unprecedented quality. However, the new limit due to oxide thickness cannot be simply overcome by technological modification. A fundamental change in technology is necessary.

One possible solution is to use an insulating film with a dielectric constant higher than that of SiO_2, so that a thicker dielectric can be deposited whilst maintaining the same capacitance

per unit area. In the mid-1990s, the microelectronics industry started to invest heavily in the development of so called high k dielectrics but to date only with limited success. For scaling of devices to continue to be a reality, the time has now come to introduce new dielectrics into the gates of MOSFETs and storage cell capacitors. Long-term goals will only be achieved it these new materials can be found.

The work reported in this thesis is mainly focused on novel high-k materials for both memories and MOS based device applications. It is divided in 3 major chapters. In the first chapter we discuss the main problems related to device fabrication. We also indicate the status of the art of modern industry and their goals for the near future. Thus, the first chapter is particularly important because it gives the reader the technological knowledge to understand why such huge investments are made every year in the microelectronic industry and research in general. In the second chapter, we illustrate the method used to deposit and grow the insulators that are the object of the investigation in this thesis. Also, we describe as best as possible the techniques of characterization used to analyze the physical and electrical properties of our dielectrics. Some examples, based on the materials analyzed, are used to help the reader to clearly understand our methodology of scientific investigation.

The last chapter is an overview of my published work in recognized international journals or presentations at major conferences. This chapter is also divided into 3 sections. The first is used to understand the lanthanum-aluminum silicates resulting from different deposition and annealing methods. These present data and some earlier data, give significant insight for our search for a possible useful high-k material. The second section is dedicated to titanium and titanium-silicate oxides. The work presented in these 2 sections provided a general idea of high-k material behavior and physical properties and lead us to focus our attention on rare-earth binary oxides, especially on Nd_3O_3 and Pr_2O_3. With the help of the published literature and our own work, we finally can elucidate the key parameters needed to be determined when searching for a novel gate oxide. Most importantly, a more organized physical method to enable selection of a new material instead of just "trial and error" emerges.

Finally, in the conclusion, we briefly summarize the objectives achieved in this work and the research that is currently in progress.

I. Scaling and Process Limitations

LOI D'ÉCHELLE: LIMITATIONS PHYSIQUES ET TECHNOLOGIQUES

Ce premier chapitre décrit les différents problèmes rencontrés en microélectronique et qui sont liés, soit au semi-conducteur, soit à l'isolant ou au métal de grille. Il est découpé en trois parties.

Dans la première partie, on présente la loi de Moore, loi d'"échelle" bien connue, comme fondement économique de l'évolution de la microélectronique. Ensuite, on décrit les problèmes physiques et les difficultés économiques à surmonter pour remplir les objectifs de la loi de Moore. Ces problèmes sont bien évidemment caractéristiques de la technologie MOSFET : dissipation de la chaleur, augmentation des courants de fuite, et, bien entendu, travail de sortie.

La deuxième partie de ce chapitre a pour objectif de conduire le lecteur dans les problématiques spécifiques à l'oxyde de grille. Pour cela, après avoir introduit les concepts de diélectrique à forte permittivité (*high-k*) et d'épaisseur équivalente d'oxyde de silicium (EOT comme *equivalent oxide thickness*), on présente une analyse des problèmes les plus significatifs au plan physique et technologique liés à l'introduction de nouveaux matériaux de grille dans la chaîne de production de circuits intégrés silicium.

Enfin, la dernière partie de ce chapitre propose une présentation succincte des principaux et plus attractifs matériaux à forte permittivité étudiés à ce jour.

I.1. SCALING

The semiconductor industry, in the last decades, had a massive growth without any comparison with all other industries. This is due to many reasons. A clear example is illustrated by the computer industry: everyone wants to replace a computer after 3 years because of speed improvements. The essential fact which has driven the successful growth of the computer industry, is that through industrial skill and technological advances one manages to make smaller and smaller transistors which go faster and faster.

Compare this situation with, for example, the automobile industry: no one would expect a car which goes five times faster and with five times larger capacity and possibly lower energy consumption, at the same price as the one which was offered five years ago. Again, this was possible in computer technology thanks to the continuing development of the basic device in the microprocessor and memory circuits: the Metal-Oxide-Silicon Field-Effect-Transistor (MOSFET). MOSFET's result from a very mature technology with relatively straight forward scaling capacity characteristics and, furthermore, the combination of complementary devices (p-channel and n-channel) enables a substantial lowering of circuit power consumption.

A third reason for MOSFET scaling is overall reduced area leading to reduced cost. Smaller MOSFETs can be packed more densely, resulting in either smaller chips or chips with more computing power in the same area. Since the cost of producing integrated circuits is highly related to the number of chips that can be produced per wafer, the price per chip is reduced.

Until the late 1990s, this size reduction resulted in great improvement in MOSFET operation with no deleterious consequences. The difficulties with decreasing the size of the MOSFET were typically associated with the semiconductor device fabrication process, until most recently when microelectronic companies realized that new materials will also have to be found and integrated in order to respect certain criteria.

I.1.1. Moore's law

Formulated in the early 60s, Moore's law states that the transistor density on an integrated circuit chip will double every 18 months. This empirical law drove the phenomenal growth of the semiconductor industry and appears still to guide the industry for the next generations

[www]. The main consequences of Moore's law are the scaling down of the devices: historically, the supplied voltage scales at 0.85 per generation and the gate length at 0.65/generation. Furthermore the gate length is expected to continue to scale at considerably less than half the lithography pitch[1] for future generations. Consequently the supplied voltage is expected to drop below 1 volt. This considerably impacts the design architecture of the transistors with the power supply voltage and the gate length. If we look at the roadmap [www] goals for the future, for example, we notice that by 2013 it is expected, for a DRAM process, that the physical gate length will be only 13 nm (Table I.1).

Table I.1. *Some of the most important parameters included in the microelectronic roadmap [www] for the coming years.*

Year of production	2004	2007	2010	2013
Technology node	90	65	45	32
DRAM ½ pitch (nm)	90	65	45	32
Physical gate length (nm)	37	25	18	13
Function/chip (Gbits)	4.29	17.18	34.36	68.72
Power supplied voltage (V)	0.9-1.1	0.8-1.1	0.7-1.1	0.6-0.9
Leakage current (A cm^{-2})	4.5×10^{2}	9.3×10^{2}	1.9×10^{3}	7.7×10^{3}
Oxide thickness (EOT) (nm)	1.3	0.9	0.7	0.6

Looking carefully at Table I.1, certain observations come directly to the attention of the reader. For example, in less than 10 years, the gate physical length is expected to decrease by a factor of 3 and the gate oxide (EOT) by a factor of 2. The power supply voltage is anticipated to vary from 1.1 V to 0.6 V with increase of the operational frequency of the

[1] In the simplified approximation of coherent illumination, the resolution *R* of a lithography system is conventionally quoted in terms of the smallest half-pitch of a grating that is resolvable as a function of wavelength λ and numerical aperture NA, as expressed by Rayleigh's equation, $R = k_1\lambda/NA$

where k_1 is the Rayleigh constant. For conventional optical lithography, the ultimate resolution limit is reached at $k_1 = 0.5$, the state at which only one set of diffracted orders can pass through the imaging optical system. Even as exposure wavelengths decrease from 248 nm to 193 nm and 157 nm, and numerical apertures increase from 0.5 to 0.6, 0.68, and 0.75, the resolution limit of $k_1 = 0.5$ stands firm with conventional optical lithography [Liebman]

chip by a factor 10. It is evident that there is a correlation between these variables, and in fact the roadmap is generated considering all the aspects that link those numbers.

Reduced voltage specifically calls for either reducing threshold voltage of the devices or reducing the channel length or both. In the simple model for a FET, the drive current initially increases linearly with the applied voltage V_D, then saturates to a maximum when V_D is equal to difference between the gate voltage V_G and the threshold voltage V_t is equal to $V_{D,\,sat} = V_G - V_t$, [Sze]. The expression for the drive current in saturation regime ($I_{D,\,sat}$) is given by [Sze]:

$$I_{D,sat} = \frac{W}{L}\mu C_{ox}\frac{(V_G - V_t)^2}{2} \qquad \text{I.1}$$

where

$$C_{ox} = \varepsilon_{ox} / d_{ox}. \qquad \text{I.2}$$

The capacitance of the oxide C_{ox} is given per unit area, μ is the channel carrier mobility, W is the width of the channel and L is the channel length, d_{ox} is the dielectric thickness and ε_{ox} is the oxide permittivity. Reduction of the channel length or increase of the gate dielectric capacitance will result in an increase of $I_{D,\,Sat..}$ The term $V_G - V_t$ is limited in range because a too large V_G creates a very strong electric field across the gate oxide. Consequently, reliability issues and working temperature condition can cause constraints in the choice of V_t. This threshold voltage cannot be easily reduced below 0.2 V because KT ~ 0.025 V at room temperature. The presence of fixed charge at the interface between Si and the gate oxide causes a miss alignment of the semiconductor Fermi energy level and the metal Fermi energy level (i.e. paragraph I.2.1 Figure I.6). Thus additional voltage is required in order to bring the Fermi levels into alignment [Sze]. This voltage is usually called "flat band voltage V_{FB}" for MOS capacitors.

Reducing the threshold voltage, unfortunately, may increase the current that goes through the channel when the transistor is in the off state (i.e. paragraph I.1.5 and Figure I.3), causing excessive power dissipation and a low I_{on}/I_{off} ratio. If channel length is reduced, the doping

level must be raised to reduce the magnitude of short channel effect. When the doping level is raised, more thermal carrier effects raise. Larger doping also means that there may be increased channel assisted junction breakdown. To reduce some of these problems the drain may need a more sophisticated doping profile, with a lightly doped region adjacent to the channel. However, this increases the channel resistance and trades performance for reliability. Greater oxide thickness helps to reduce hot carrier effects but it increases the short channel effect. However the oxide thickness is expected to decrease as the supply voltage decreases, to avoid short channel effects.
It appears relevant here to describe in detail some, if not all, the problems that one has to face when designing and fabricating a simple MOSFET.

I.1.2. Power dissipation and heat production

The previous section may be revisited in terms of power dissipation. The increasing density of MOSFETs on an integrated circuit chip is creating problems because of substantial localized heat generation that can impair circuit operation. Circuits operate slower at high temperatures, and have significant reduced reliability. Heat sinks and other cooling methods are now required for many integrated circuits including microprocessors. This situation will become dramatically evident for very advanced technologies

I.1.3. Process variation

The changes necessary to satisfy the parameter values cited in the Table I.1 will introduce a change in the process flow. It is important to understand, at this point, that a need expressed cannot necessarily become a reality because of technical difficulties. Some of these difficulties in the process variation includes:

- Si production will be based upon 300 mm diameter wafers. All industrial tools are expected to work with this standard Si wafer size, and in the near future probably on 450 mm [www]. A larger wafer allows an increase in the number of chips per wafer, so that the cost per chip decreases. It is understadable that replacing Si with a different material would be extremely expensive, and so all the technology prefers to remain on Si-based transistors.

- New materials can perhaps be made only using hazardous components (precursors)
- The conversion of the new geometries into binary arrays increases the metrology problems.
- Design difficulties: the transistor channels are reaching the quantum scale (few hundred's of atoms).

Figure I.1 has been taken from the presentation of Robert Madge (LSI Logic Corporation) at the Electronic Manufacturing corporate 2005 meeting. The complexity in the design in order to maintain the predictions of Moore's law is much higher than the industry capability. This is translated in a time shift between the required device complexity and the actual device productivity time.

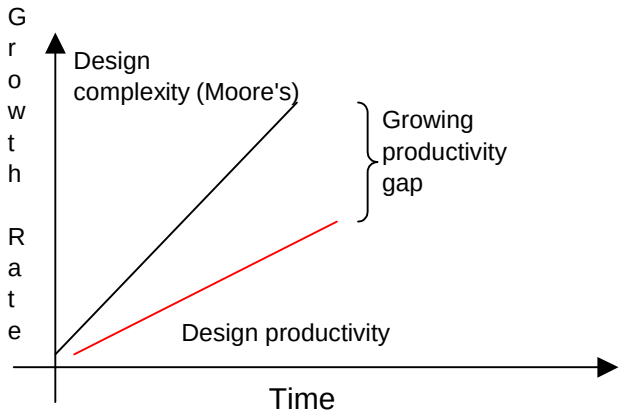

Figure I.1*. Gap between the design complexity predicted by the Moore's law and the actual productivity capability*

This picture explains how technology is already behind the prediction of Moore's Law. The technological limits, that have not been an issue since the earlier 90's, are becoming more relevant and are overtaking the physical aspects related to the roadmap.

I.1.4. Work function

The work function is the voltage required to extract an electron from the Fermi energy to the vacuum level. This voltage is between 3 to 5 Volt for most metals. The actual value of

the work function of a metal deposited onto silicon dioxide is not exactly the same as that of the metal in vacuum.

The primary criterion for the gate material is that it is a good conductor. Highly-doped poly-crystalline silicon is an acceptable, but certainly not ideal conductor, and it also suffers from some more technical deficiencies in its role as the standard gate material. So why use polysilicon instead of a metal like Al. There are a few reasons. The threshold voltage (and consequently the drain to source on-current) is determined by the work function difference between the gate and channel material. If there is no charge present in the oxide or at the oxide-semiconductor interface, the so called flatband voltage simply equals the difference between the gate metal work function, Φ_m, and the semiconductor work function, Φ_s :

$$V_{FB} = \Phi_m - \Phi_s = \Phi_{ms} \qquad \text{I.3}$$

For nMOS transistor switch-on threshold voltage, V_t, is then:

$$V_t = V_{FB} + f(\phi_f, C_{ox}, N) \qquad \text{I.4}$$

where N is the substrate doping concentration expressed in cm^{-3}, and ϕ_f is the bulk voltage.

In the past, when gate voltages were high (of the order of 3 V to 5 V), the high threshold voltage caused by the work function difference between a metal gate and silicon channel could still be overcome by the applied gate voltage ($|V_{GS} - V_t| > 0$, where V_{GS} is the gate-source voltage). However, as transistor sizes were reduced, the supply voltage was also reduced for various reasons (such as to avoid gate oxide breakdown, hot-electron stressing, power consumption reduction …). In consequence a device with such a high threshold voltage would not have been operational. Thus, poly-crystalline silicon was used as an acceptable gate material essentially because its similar chemical composition to the silicon channel resulted in a smaller V_{FB}. In inversion, the work function difference becomes close to zero, ensuring the transistor can be turned on at a lower voltage and that the on current is high. However, even heavily doped polysilicon is highly resistive (of the order of 1000 times more resistive than a common metal), which in turn will reduce the signal propagation speed through the material (and therefore will increase the time the transistor takes to switch from

'off' to 'on' or vice versa). A metal is combined into the top of the polysilicon to decrease the resistivity. Such an alloyed material is called silicide. Silicide - polysilicon layered materials have better electrical properties than polysilicon alone. Also, the threshold voltage is not significantly higher than polysilicon alone, because the material above the silicon channel, after the gate oxide, remains doped polysilicon.

Pure metal gates would be very desirable to eliminate dopant depletation effects and sheet resistance constraints. In addition using a metal can lower the required thermal budget by eliminating the annealing for dopant activation in the polysilicon electrodes. There are two approaches towards achieving successful integration of a metal electrode. The energy diagrams associated with the two approaches are shown in Figure I.2.

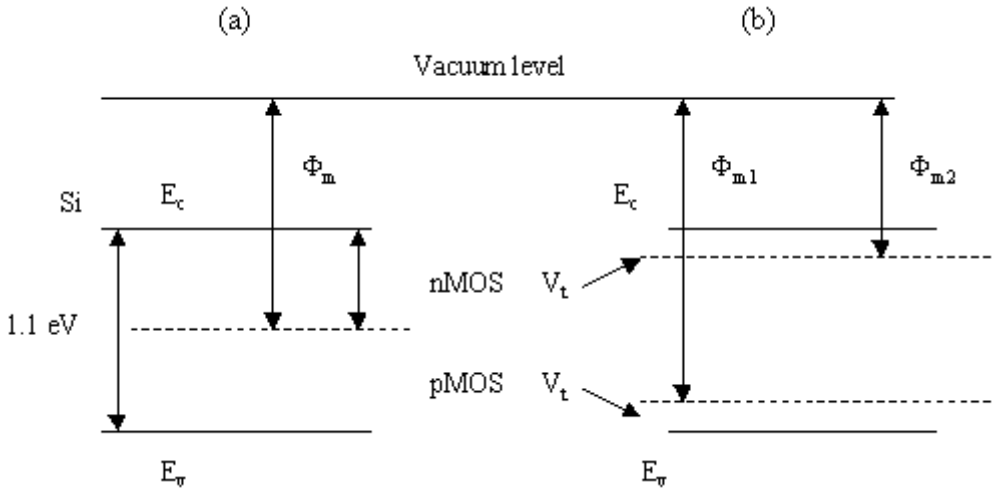

Figure I.2. *Energy diagrams of threshold voltage: a) using one midgap metal gate; b) using dual metal gates.*

a) The single midgap metal method uses a metal (i.e. TiN) that has a work function that places the metal Fermi level at the midgap of the silicon substrate (Figure I.2 a). The benefit in using midgap metals resides in the definition of the metal Fermi level (E_F). So that, the same energy difference exists between the Fermi level and the conduction and valence band energies (E_c and E_v) of the semiconductor. Consequently V_t can be made symmetric for both nMOS and pMOS. This provides a simpler processing scheme, since only one mask and one metal are required for the gate electrode for both types of transistor.

b) Two separate gate metal electrodes are introduced, one for pMOS and one for nMOS. In Figure I.2b we represent the energy diagram for this approach. We define Φ_{m1} and Φ_{m2} the work functions of the 2 metals. The 2 electrode metals are chosen in such a way that their Fermi levels line up favorably with the conduction and the valence bands of the silicon substrate. For example if we use Al as the metal for nMOS, and Pt as the metal for pMOS, we obtain for both types of transistor a $V_t \sim 0.2$ V. This is an ideal case that in practice is not feasible. For example, Al tends to form Al_2O_3 in contact with the oxide, so that an interfacial layer between the metal gate and the gate oxide occurs (this is not a problem if the oxide is really thick). Other metals such as Ta or TaN that have relatively low work functions are more attractive, especially for very thin oxide films. Pt also has its limitations. It is quite expensive, does not adhere well on many oxides, but it is inert with most of the oxides. Therefore it is a practical choice for some research studies, but not industrially acceptable. The same conclusions can be drawn for Au.

I.1.5. Leakage Current

The presence of the leakage currents degrades the electrical properties of the transistor and it increases the power that is dissipated. There are 3 main sources in transistors of leakage current:

a) Junction leakage: a current due to the increasing of the doping level in the substrate
b) Subthreshold leakage, a weak inversion current across the device
c) Gate leakage, a tunneling current through the oxide insulator.

The importance of these leakages for a gate length of 30 nm is represented in the following Table I.2.

Table I.2. *Typical leakage currents in MOSFETs device: junction current (I_{je}),total transistor leakage current per chip (I_{off}) and gate leakage (I_g).*

I_{je} (A/μm)	I_{off} (A/μm)	I_g (A/μm)
10^{-9} - 10^{-10}	10^{-8} - 10^{-7}	> 10^{-7}

In this paragraph, we describe these 3 sources of leakage.

a) **Junction leakage:** the cause of this leakage is due to the high doping concentration in the channel region required to maintain the threshold voltage V_t and to limit the short channel effects in aggressively scaled down devices. The proximity of the valence and the conduction band in the depletion region of the junction causes a parasitic tunneling current. In other words, the leakage junction current I_{je} increases with the doping concentration of the substrate It has been suggested that this leakage alone will limit scaling [Ghani] and increase the process complexity [Nakahara]

b) **Subthreshold leakage current:** this is a intrinsic leakage itself, and is probably one of the main problems facing continued scaling. The leakage current flows from the drain to source of a MOSFET when the transistor is supposed to be off ($|V_{GS}| < |Vt|$). As the transistor becomes smaller, a lower power supply voltage is required to reduce the dynamic power consumption, as we can show in Eq. I.5:

$$P = VI = ACV^2 f + I_{off} V \qquad \text{I.5}$$

where *f* is the chip operating frequency, C is the gate oxide capacitance and I_{off} is the total transistor leakage current per chip and A is the fraction of gates actively switching. The first part of the equation refers to the dynamic part or the active power, (the power that is consumed when the transistor is switching from an on-state to an off-state), and depends on the square of the supply voltage. The dynamic power arises from the repeated capacitance charge and discharge on the output of the hundreds of million of gates in today's chips. To maintain the performance of the chip (I_{sat} = constant), the power supply scales as well as V_t so that the principal source of the dynamic power dissipation is the chip frequency (i.e Table I.1).

The second part of the equation refers to the "stand-by" or off power and strictly depends on the transistor in off state. The difference between the off state and the on state is represented in Figure I.3. There is an inherent correlation

between the I_{on} and I_{off} currents, which means that neither of them can be set completely independently from the other: if the drive current is increased by reducing the threshold voltage, the leakage current will usually become higher, too. The following equation [Chandrakasan] describe the mechanism of the off state currents:

$$I_{off} = K_1 W e^{-V_t / nV_o} \left(1 - e^{-V/V_o}\right) \qquad \text{I.6}$$

K_1 and n are experimentally derived constants and V_o is voltage due to the thermal activation (kT ~ 0.025 V for room temperature) and it increases linearly as temperature increases. If I_{off} increases enough to build up heat, V_0 will also increase, further increasing I_{off} and possibly causing thermal runway. Eq. I.6 suggests that there are 3 ways to reduce the I_{off}. First, we could turn off the supply voltage V so that the $\left(1 - e^{-V/V_o}\right) = 0$. Second we can reduce W and third we can increase V_t. This last solution rises two problems. I_{off} is a negative exponential in V_t so that a small increment or fluctuation of V_t can lead to a dramatic variation of I_{off}. Furthermore the increasing of V_t decreases the operating frequency of the chip as described by the following equation

$$f = \frac{(V - V_t)^{\alpha}}{V} \qquad \text{I.7}$$

where α is an experimentally derived constant. A smaller *f* means a loss in performances. The reduction of I_{off} by 1/3 for SiO_2 in Very Large Scale Integration (VSLI) technology has been demonstrated by [Boris]

We finally observe that some of the variables that influence the I_{off} also influence the gate leakage current (Eq. I.8). For example if the supply voltage decreases the I_g decreases as well, but as already said the chip operating frequency would be lowered.

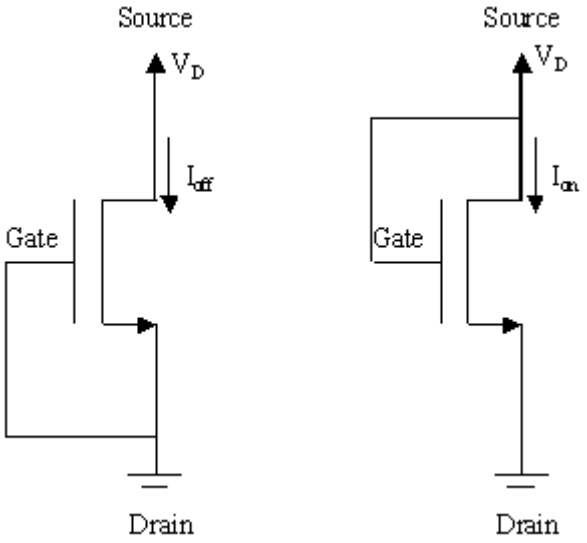

Figure I.3. *Definition of the I_{on} and I_{off} current for a MOSFET*

It is interesting to note in conclusion that, from what we said scaling causes the reduction of the supply voltage, so that the active power decreases but consequently the off power tends to increase, as has been demonstrated by Intel researchers in the following diagram (Figure I.4).

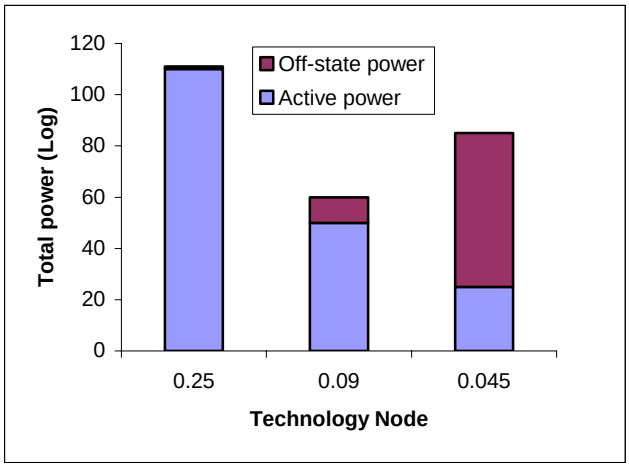

Figure I.4. *Power generated by transistors versus the technological node*

c) **Gate leakage:** As well as the leakage current component I_{off}, another important source of leakage arises as one thins the gate dielectric, current begins to leak

from the gate through the insulator film. This starts to happen around 1.5 nm for SiO_2 gate oxide thickness [Stathis]. For increased scaling, although there is some debate about the exact thickness when this will happen, a change in the transistor architecture to include high-k, will be necessary. The key factors that influence the gate leakage are given by [Chandrakasan] and shown in Eq. I.8

$$I_g = K_2 W \left(\frac{V}{d_{ox}} \right)^2 e^{-\alpha d_{ox}/V} \qquad \text{I.8}$$

where K_2 and α are experimentally derived constant. The terms of interest are the applied voltage V and the oxide thickness d_{ox}. Figure I.5 shows the behavior of the oxide leakage versus the gate voltage for different oxide thicknesses [Lee2]

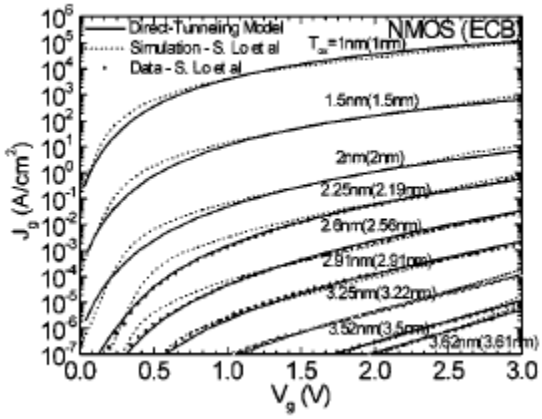

Figure I.5. *Oxide tunneling leakage versus the gate applied voltage and for a certain oxide thickness. The dotted lines are the experimental values and the dashed lines are the calculated values [Lee]*

Increasing the oxide thickness clearly decreases the oxide leakage. But increasing of the SiO_2 gate oxide thickness is not an option in order to achieve the goals required by the roadmap presented in Table I.1 Therefore, the research community is condemned to pursue the development of high-k dielectric gate insulators.

I.2. THE GATE OXIDE

Scaling requirements for the next 14 years have been well outlined in the ITRS roadmap [www]. Because technology used primarly the gate oxide thickness as a relevant parameter, and the material used to date has been SiO_2, the same terminology is retained for future generations. Requirements show (Table I.1), that if SiO_2 were to continue to be used one would require thicknesses which are physically unreasonable and approaching the monolayer. However, for such, a symbolism can continue to be used if we talk in terms of Equivalent Oxide Thickness (EOT). Here, one assumes that an alternative dielectric will in fact replace the SiO_2 and the EOT will be:

$$d_{SiO_2} = \frac{\varepsilon_{SiO_2}}{\varepsilon_{newdielectric}} d_{newdielectric} \qquad \text{I.9}$$

where d_{SiO2} is the thickness of silicon oxide, εSiO2 is the dielectric constant of silicon oxide, $d_{newdielectric}$ and $\varepsilon_{newdielectric}$ are the thickness and the dielectric constant of the possible substitute for SiO_2. As an example, if the EOT is 0.5 nm and one has available a dielectric of constant 40 then the appropriate $d_{newdielectric}$ would be ~ 5 nm.

On the basis of the foregoing discussion of scaling, it can be argued that the key element which to date has enabled scaling of Si-based MOSFETs is the dielectric formed by thermal oxidation: SiO_2. The use of **amorphous** thermally grown silicon dioxide as a gate dielectric and as a surface passivation layer [Frosch] [Stathis2] offers many advantages in CMOS processing including thermodynamic and electrical stability, a high-quality Si-SiO_2 interface as well as exceptional electrical insulation properties. These outstanding electrical properties clearly present a significant challenge for any alternative gate dielectric candidate. A variety of considerations must taken into account then:

- Relative dielectric constant
- Dielectric/semiconductor interface quality
- Intrinsic leakage current and reliability
- Tunneling current and band offset

- Thermal stability (phase change, morphology changes …)
- Process compatibility (deposition, etching, scale integration …)

The tunneling leakage current has already been discussed in the paragraph I.1.5. We will treat in the following the other issues, one by one.

I.2.1. Gate compatibility, dielectric constant and barrier height

The interfaces with both the gate and the Si channel region are particularly important in regard to the FET performance. These regions, represented in Figure I.6a, are typically of, but not necessary, ~ 0.5 nm. It is evident that these regions can modify the overall capacitance of the gate stack, especially if they have a thickness which is comparable to that of the gate dielectric. However, these regions can be used to obtain desirable properties. For example, in the case of polysilicon gates, the interface between the gate and the oxide can be used to block boron diffusion from the polysilicon gate. The interface between the Si channel and the gate oxide can be used to develop low trap densities (e.g. dangling bonds) and so minimize carrier scattering resulting in increased mobility.

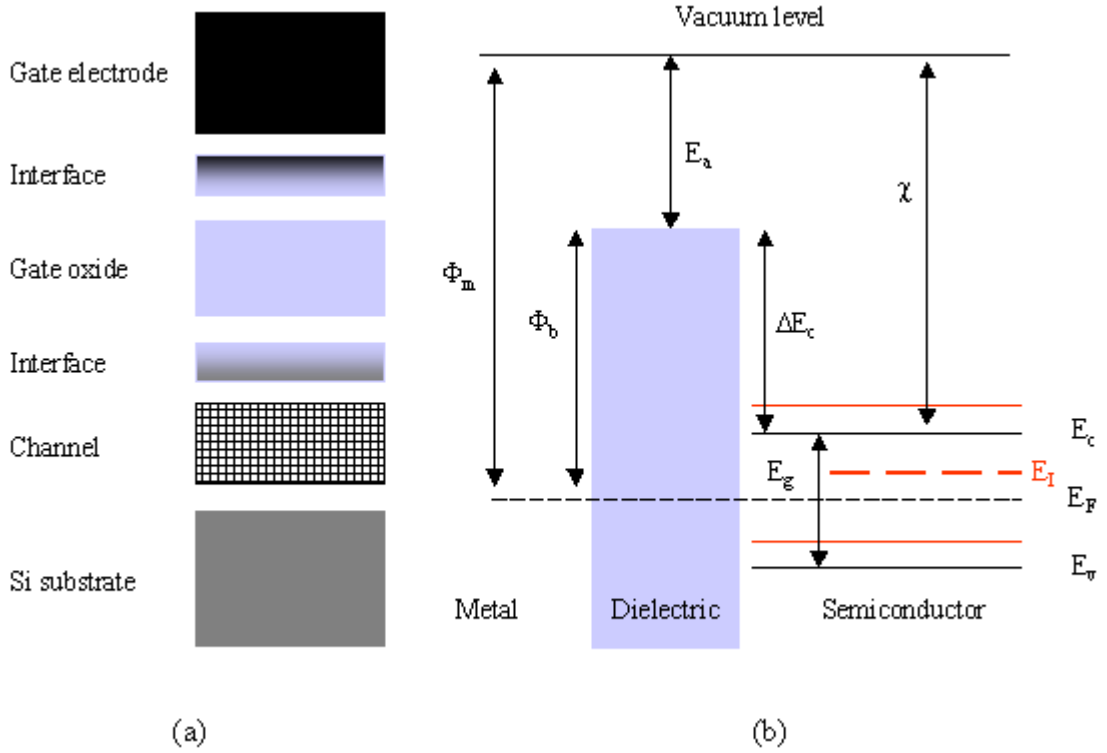

Figure I.6. *(a) Schematic structure of a Metal-Insulator-Structure (MIS) and (b) Energy band diagram for an ideal MIS. The red lines refer to a MIS structure with p doped semiconductor substrate.* Φ_m*, is the metal work function,* Φ_b*, is the potential barrier between the metal and the oxide,* χ *is the equivalent of the metal work function for the semiconductor and is known as semiconductor electronic affinity,* E_a *is the dielectric electron affinity,* E_g *is the semiconductor gap between the conduction band (*E_C*) and the valence band (*E_V*),* E_F *is the Fermi energy level and* E_I *is the intrinsic Fermi level.*

The required permittivity must be balanced, however, against the barrier height for the tunneling process. In the simplest approximation the barrier eight for carrier injection from the metal gate on semiconductor into the dielectric conduction band is:

$$q\Phi_b = E_{bh} = q\Phi_m - E_a \qquad \text{I.10}$$

where E_a is the dielectric electron affinity. For SiO_2, E_a is ~ 0.9 eV. For Al on SiO_2, Φ_m (Al) is ~ 4.1 eV, so the barrier eight E_{bh} is ~ 3.2 eV. For Si E_{bh} depends upon the semiconductor doping level [Sze]. For example for Al/n-Si and Al/p-Si junctions E_{bh} is ~ 0.2 eV and 0.92 eV respectively.

For an electron traveling from the Si substrate to the gate, the so called conduction band offset (ΔE_c) [Robertson] is given by:

$$\Delta E_c = q[S\chi - (\Phi_m - \Phi_b)] \qquad \text{With} \qquad 0 \le S \le 1 \qquad \text{I.11}$$

where χ is the semiconductor electron affinity and Φ_b is the barrier height that an electron sees when traveling from the gate to the Si substrate. S is a term that can modify the barrier height and it depends of the interface state density.

Expanded studies made by [Robertson2] include many more high-k materials (some of them are still under investigation). The results for some of these materials are given in Table I.3. If the experimental ΔE_c values for these oxides are much less than 1.0 eV, they will have to be excluded for gate applications, since electron transport (either thermal emission or tunneling) may lead to an unacceptably high leakage current. In fact, in order to obtain low leakage currents, it is desirable to find a gate dielectric that has a large ΔE_c value with respect to Si, as

it is the case of SiO_2. For the electron direct tunneling process the leakage current J_{DT}, increase exponentially with decreasing barrier height (**and thickness**) [Sze]:

$$J_{TD} = \frac{C_1}{d_{ox}} \exp[-2d_{ox}\sqrt{C_2(\Phi_b - V_{ox}/2)}] \qquad \text{I.12}$$

C_1 and C_2 are constants and V_{ox} is the voltage across the dielectric. For highly defective films, which have electron trap energy levels in the insulator band gap, electron transport may be governed by a trap-assisted mechanism such as Frenkel-Poole emission or hopping conduction [Dekker] [Yang]. Since the ΔE_c values for many potential gate dielectrics have not been reported in literature, the closest and crudest indicator of band offsets is the band gap (E_g) of the dielectric. A large E_g generally corresponds to a large ΔE_c, as is shown in Table I.3 Unfortunately many materials that have a large ΔE_c also have a large valence band offset. Table I.3 also indicates that E_g will be somewhat limited: the dielectric constant and the band gap of the materials follow an inverse relationship. The detailed equations linking the permittivity and the band gap are not trivial and will not be reported here.

Table I.3. *Relevant properties of some high-k insulators on Si [Wallace] [Robertson]*

Material	Dielectric constant (k or ε)	Band gap E_g (eV)	ΔE_c (eV) to Si	Crystal structure
SiO_2	3.9	8.9	3.2	Amorphous
Si_3N_4	7	5.1	2	Amorphous
Al_2O_3	9	8.7	2.8[a]	Amorphous
Y_2O_3	15	5.6	2.3[a]	Cubic
La_2O_3	30	4.3	2.3[a]	Hexagonal, cubic
Ta_2O_5	26	4.5	1-1.5	Orthorombic
TiO_2	80	3.5	1.2	Tetragonal (rutile, anatase)
HfO_2	25	5.7	1.5[a]	Monoclinic, tetragonal, cubic
ZrO_2	25	7.8	1.4[a]	Monoclinic, tetragonal, cubic

[a]Calculated by [Robertson]

I.2.2. Thermodynamic stability on Si and interface quality

In FET technology the interface with the silicon substrate plays a primary role and in most cases is the dominant factor that determines the overall electrical properties of the device. Although an extensive thermodynamic gas phase study [Hubbard] suggested that a prior number of binary high-k oxides were inert with respect to Si, almost all high-k metal oxide systems investigated so far (in the solid state) have unstable interfaces with silicon: they react to form an undesirable interfacial layer, after a silicide. Materials that could replace SiO_2 as a gate insulator therefore may require an interfacial reaction barrier. Any ultra-thin interfacial reaction barrier with EOT less than 2 nm must have the same quality uniformity and reliability qualities as SiO_2 does in the same thicknesses regime. Thus it is important to understand the thermodynamics of these systems, and attempt to control the interface with Si.

It is difficult to imagine a better interface than that of SiO_2, since typically interfaces have a mid gap interface state densities of $D_{is} = 2*10^{10}$ states/cm^2 or less. Most of the high-k/Si structures reported in the literature so far have $D_{is} \sim 10^{11}$-10^{12} states/cm^2 and exhibit a substantial flat band voltage shift $\Delta V_{fb} > 0.3$ V, most likely due to a fixed charge density of $\sim 10^{12}$ cm^{-2} or higher at the interface.

I.2.3. Process compatibility

The method by which the dielectrics are deposited in a fabrication process is another crucial factor in determining the choice of final film material.

The deposition process must be compatible with current or expected CMOS processing, cost and throughput. Since all of the available deposition techniques occur under non-equilibrium conditions, it may be possible to obtain properties which differ from those expected under equilibrium conditions. Furthermore, it is important to consider the various methods for depositing the dielectrics. Here we discuss only the most promising methods.

In order to understand the reasons that tend to eliminate some oxidation processes, it must first be remembered that the required film thicknesses, even of high-k materials, are probably, ultimately < 2 nm. The following requirements for the technologies used to deposit the materials are:

a) Possible low temperature deposition
b) Very large deposition uniformity (300 mm and in the near future 450 mm) [www]
c) Compatibility with Si processes
d) Safety: hazardous materials or precursors should be avoided
e) Very controlled in order to achieved very thin layers and controlled interfaces
f) Industrially convenient

Here we describe some of the techniques mostly used by the industries.

- **Physical vapor deposition** PVD (i.e. sputtering and evaporation), methods have demonstrated their superior competivity because the deposition process can be carried at low and high temperature and the material deposited is really uniform over a very large surface. The damage inherent to sputtered PVD processes, which can create unwanted interfacial states, seems to be the major disadvantage of this method. The CVD method is more successful even if the reaction kinetics of the precursors used in the process requires careful attention in order to control layer formation. The precursors used must also be tailored to avoid unwanted impurities in the film as well as permit an exact final composition of the deposited film (i.e. oxide stochiometry). Indeed these precursors may be the key requirement in order to control interface state formation to a level comparable to that of SiO_2.
- **Plasma Enhanced Physical Vapor Deposition** (PEPVD) are conceptually the same as PVD deposition processes. In addition to PVD, PEPVD uses a plasma source in order to activate the precursors and lower the deposition temperature.
- **Atomic Layer Chemical Vapor Deposition** (ALCVD) is used because of self-limiting chemistries employed to control film formation in a layer-by-layer fashion. The major limitation to ALCVD is the surface preparation and the resultant chemistry. This is wafer-by- wafer process.
- **Molecular Beam Epitaxy** (MBE) can easily grow a film layer of less than 1 nm but cannot utilize high oxygen background pressures. Consequently, incomplete oxidation due to incorrect oxygen stochiometry may appear as a challenge.
- **Pulsed Laser Deposition** (PLD) also is very useful because the film thickness control and stochiometry. It is also been used to deposit complex oxides without

fears of sub-stochiometry. Anyhow due to the incompatibility with the Very Large Scale Integration (VLSI), this technique has not been widely developed industrially.

I.2.4. Film morphology

Much of the success of SiO_2 in present day microelectronics technology arises because the films are amorphous and therefore able to be very flat and continuous. There are no grain boundaries as in a polycrystalline material and therefore the suspected leakage current due to the grains is absent. As shown in Table I.1, with the exclusion of the Al_2O_3, SiO_2 and Si_3N_4 all the high-k of interest will form a polycrystalline film either during deposition or upon a modest thermal treatment. Many of the high-k materials, if not all, have large dielectric constants only in the crystalline phase. If such materials are used as gate dielectrics it is to be anticipated that grain boundary leakage may be significant. Furthermore, the presence of adjacent crystals of different orientation may give rise to substantial surface roughness leading to a very non-uniform variation of the gate dielectric in the active channel region of the FET device (i.e. irreproducible properties).

It is important to note, however, that it has been shown for some materials that there is a suppression of crystallization for very thin oxide films. The extent of crystallization suppression for a given oxide depends on both oxide and substrate-in-contact composition and thermal processing.

Single crystal oxides obtained via MBE methods can, in principle, avoid grain boundaries while providing a good interface [Eisenbeiser] [Kwo], but these oxides require sub-monolayer deposition control, which can be obtained, indeed, only by MBE. Unfortunately MBE methods are not compatible with VSLI technology as was mentioned in paragraph I.2.3.

I.3. HIGH-k GATE OXIDE CANDIDATES

Hafnium oxide has a k value of about 15-25 for the crystalline phase [Wallace] [Kukly] and a value of 15 for the amorphous phase [Okada]. But the use of hafnium oxide presents fabrication challenges. For example, although SiO_2 can be formed on silicon by simple thermal oxidation, hafnium oxide must be deposited with sophisticated Chemical Vapor

Deposition (CVD) or Atomic Layer Deposition (ALD) techniques. Furthermore, because the deposition process involves volatilization, the hafnium molecule must be volatile, typically organic, precursor. Furthermore, these processes open the way to new technological issues. To be a successful precursor, a compound must be able to survive the volatilization process, but then be able to dissociate on command on the silicon substrate. It must also deposit properly on the substrate such that an amorphous rather than a crystalline film is formed. "You have a narrow window of stability with these precursors"! Amorphous HfO_2 means a low dielectric constant, which will put the end to the use of these materials in few years. Futhermore HfO_2 has demonstrated a limited but important reactivity with Si [Hubbard], which tends to results in a thin interfacial layer, and also has a low (~ 400 °C) crystallization temperature. To avoid this problem, different alloys of Hf based oxides have been brought to researched. The Hf-Al-O compounds do not show any improvement of the electrical characteristic, compared to the Hf oxide [Lee]. Hafnium titanate films, as the Hf content increases, the EOT decreases and the films crystallize anisotropically. But still an interfacial layer of pure SiO_2 grows between the mixed oxide and the Si substrate, with the consequence that an EOT smaller than 1.4 nm is not achievable [Li]. From the point of view of thermodynamic stability with Si, the most successful material has been HfSiO. Actually since 2003 Texas Instrument chose HfSiON as the material for the logic market. More recently ALD [Seokhoon] of HfSiON has also been demonstrated to produce a good control of the interface avoiding the thermal instabilities between the Si and the Hf-O bonds. Obviously the presence of the Si-O bonds in the HfO_2 matrix decreases the value of the dielectric constant, and, even if N_2 is added to increase the density of the oxide in order to obtain an higher value of k, the permittivity do not exceed the value of 11 [O'Connor]. No long term solution seems to appear for the Hf based compounds, so pure Hf oxide is actually leading the market for the moderate high-k.

Al_2O_3 (alumina) has many favorable properties as an alternate high-k material: since it is very stable against SiO_2 formation and, the optical bandgap is 8.7 [Wallace], it remains amorphous under the processing conditions of interest. The stability of alumina depends on the equilibrium condition of the process. The evidence of a layer of $AlSi_xO_y$ [Klein] has been found when studying films of Al_2O_3 deposited via CVD of 400 °C, which was not expected on the basis of the phase diagram [Hubbard]. Films of Al_2O_3 deposited using Atomic Layer

CVD (ALCVD) onto H-terminated Si, under non equilibrium condition, using trimethyl-aluminun and water as the precursor for Al and O, has been obtained without any interfacial layer. This is an important result because it demonstrates that it is possible to control the interface reaction and hence the deposition conditions. Unfortunately, the maximum k value was 7.

La_2O_3 was also found to be interesting, because its high dielectric constant of 27 and long term reliability [Wu]. Recently Guha et al investigated thin films (EOT of 1-1.4 nm) with low leakeage currents (~ 10^{-4}-10^{-7} A/cm^2) and with an amorphous SiO_x interfacial layer [Guha] and [Ono] found evidence for the interaction between Si and the La. It should be also underlined that lanthanum oxides are hygroscopic, a characteristic that reduces the long term reliability and makes processing management difficult.

A combination of both La_2O_3 and Al_2O_3 has attracted interest, as a good combination of a material with a high dielectric constant, high optical gap and certain stability with silicon [Xiang] [Li2]. [Park], using molecular beam deposition at 800 °C, was able to deposit an amorphous layer of $LaAlO_3$ although the leakage current density was very low, ~ 10^{-9} A/cm^2, A post annealing process in O_2 atmosphere, in order to remove the considerable flat band voltage, lowered the EOT to only 3 nm, probably due to interfacial SiO_2 layer formation between the oxide and the semiconductor. The post annealing in O_2 seems to improve the quality of the interface as recently [Miotti] had demonstrate on sputtered $LaAlO_3$ MOS capacitors. Once again, the dielectric constant moved from an expected value of 25 to 14, which indicates that the Si/oxide interfacial layer drastically reduces the dielectric properties of the high-k dielectric. In conclusion, the literature, as well as our studies are not that encouraging. The main reason is that the $LaAlO_3$ oxide tends to be highly reactive with the Si interface, resulting in the formation of silicide that is not limited to one or two interfacial layers.

Titanium dioxide is well known among the materials that have a refractive index (n) higher than Si_3N_4 (2.00), TiO_2 is one of the most quoted because it has demonstrated that it can be prepared using different techniques such as evaporation, ion implantation, sputtering and plasma enhanced chemical vapor deposition (PECVD), and it has always shown a value of n from 1.79 to 2.6 [Martin] [Busani]. This variability resides in the TiO_6 octahedral structure, the building block of rutile and anatase. In addition to all these properties, the main reason

that has maintained TiO_2 as an interesting material for research in the chip application is its dielectric constant, which span from 31 to 110 [Tang] [Scarel]. Unfortunately, the reason of such as wide range in the electrical properties is due to the crystalline phases of TiO_2. These phases usually form at low temperature (600 °C for the rutile, 250 °C for the anatase), which makes TiO_2 incompatible with the standard processes used by microelectronic industries. In order to obtain a high dielectric constant for amorphous TiO_2 and at the same time be capable to control the phase transition, CVD and PECVD seems to yield good results. These methods involve precursors such us $TiCl_4$ [Williams], TIPT [Frenck] and TEOT [Ha], and the use of these metallorganic compounds is the subject of 3 considerations: (i) $TiCl_4$ is hazardous and highly corrosive and requires special installation, (ii) Cl can be a major contaminant in TiO_2 and increases its optical absorption coefficient [Williams] [Frenck] and (iii) Ti is a transition metal and so it can have different stochiometries (TiO, Ti_2O_3). During the deposition O_2 gas should generally added to ensure the TiO_2 stochiometry, which involves a detailed knowledge of the process and all variables involved. Complete transistors using CVD gate dielectric were first reported by [Campbell] using Pt electrodes to prevent reaction of the gate interface. In these transistors, the device performance was limited by the formation of the interfacial oxide layer (due to the post annealing process), a relatively large interface state density ($10^{12}/cm^2$ eV) and hence higher leakage currents. Although the carbon role in high-k is not yet well understood [Campbell] attributed to carbon the formation of a relevant number of defect states, so that higher leakage currents. Thus a carbon free precursor for TiO_2 and in general for high-k materials, such as $TiCl_4$, is required. The resulting devices showed EOT of 2 nm and the leakage current were reduced by a factor of 10^2 compare to SiO_2 standard transistors. Transistor made by [Guo] using a TiO_2/SiN stacked gate dielectric with an interfacial barrier layer of Si_3N_4 (1.5 nm) showed an EOT < 2 nm. The barrier layer between the Si and the oxide was capable to minimize the formation of an interfacial layer of SiO_2 during post annealing process. These structures were stable till 900 °C, but at that temperature the capacitance and the leakage current deteriorate.

Rare-earth oxides such as La_2O_3, Pr_2O_3 and Gd_2O_2 are also very attractive materials for the microelectronic industry because they are very similar and gradually changing characteristics. These oxides are claimed to be thermodynamically stable with the Si interface [Hubbard]. The dielectric constant varies from 10 to 30 depending upon many factors such as

composition, crystallinity, deposition, annealing treatment ... RE oxides, in general, suffer of many technological problems that make them non usable in the standard process or standard applications. At high temperature (~ 900 °C), they tend to form a consistent interfacial layer [Ono] which is typically SiO_2 or RE silicate or a mixture of the two. The presence of the interfacial layer and its composition as well as its thickness is determined by the deposition process, the post annealing conditions and it contributes to increase the EOT and the interface state density defects. The film crystalline structure plays a significant role in both as grown and annealed samples. In particular it seems that it is necessary to increase as much as possible the crystallization temperature to avoid irreversible film modifications in the interfacial layer and in the oxide itself. For these reasons research in these oxides is focused on epitaxially grown RE oxides and RE compounds deposited using Molecular Beam Evaporation (MBE), (ALD) or Pulsed Laser Deposition (PLD) on various semiconductors (Si, SiGe and AsGa) [Schroeder] [Liu] [Dongfang] [Hong]. Therefore finally, we can say that, although a number of issues are addressed, RE oxides can be promising materials in micro or nano-electronic. The interfacial layer, if stabilize, can be engineered.

Even a high-k insulator that meets all the requirements imposed by the roadmap, if it can be found, and if it can easily deposited on silicon, one last consideration should be made before it can be processed: is that oxide reliable? The electrical reliability is a critical step because reliability projection comes from different operating conditions and test conditions. Thus the reliability is a matter of experience, which is not available for a new material in general.

One of the fundamental mechanisms for oxide breakdown in ultra thin SiO_2 was first describe by [Degraeve] in its percolation model. Breakdown in this model is described as the build up of many defects within the SiO_2 layer, where after a certain amount of stress, (either constant voltage or current through the oxide at a given temperature) a complete path of defects forms across the oxide thickness. This point defines breakdown, or the failure, of the oxide. While there is a general agreement about the percolation model and its application to VSLI technology [Boris], the defects, which act as precursors to breakdown are not well defined.

The choice of a high-k dielectric, which satisfies the strict reliability criteria, requires a well-characterized material system, a prospect not yet available for most of the alternate materials. The implications of the dependence of voltage acceleration extrapolation on dielectric thickness and the improvement of reliability projection arising from improved oxide

thickness uniformity have only been understood in the past 5 years, despite decades of research in SiO_2 [Stathis4] [Stathis5] This emphasizes the importance and the urgency to investigate the reliability characteristics of alternate dielectrics, as these materials, will certainly differ from SiO_2.

Preliminary projections determined by stress-induced leakage current (SILC), time-dependent dielectric breackdown and mean time to failure measurements appear to be encouraging for Al_2O_3. and HfO_2 films [Roussel] [Ma]. Similar measurements on ZrO_2 seem discordant, somewhat promising, somewhat less encouraging. Despite the excellent ten-year reliability projections at high applied voltage of 2.0 V reported for these materials, it is essential to carry out proper area scaling conversion. Scaling, as mentioned above, can significantly degrade the reliability projections.

We have seen as many factors that play a role in the simplest FET technology. Some of them are purely technological, others are physical, others are related to economical issues. The main information we extract from this short summary of the state-of-the-art are essentially two. First, the permittivities of many simple oxides has been measured on bulk samples and in same cases on thin films, but for more complex materials the dielectric constants are not as well known. There is also a wide range of permittivity values for the same oxide. These discrepancies can be attributed to many factors, including film thickness, method of film deposition and local electronic structure within the dielectric (morphology). Second is that the characterization and the film deposition processes are essential to understand the physical behavior of the oxides.

Considering these two information (dielectric constant and process/characterization) we have decided to investigate some high-k. The purpose of the following chapters is to understand the physical behaviour of those materials when in contact with Si and upon different operational conditions.

REFERENCES

[Boris] L. Boris and Y. Mitnick, IEEE Reliability Phys, Symp., **319** (1999)

[Busani] T. Busani and R. A. B. Devine, Sem. Sci. Technol., **20**, 870 (2005)

[Campbell] S. A. Campbell, D. C. Gilmer, X. Wang, M. T. Hisich, H. S. Kim, W. L. Gladfelter and J. H. Yan, IEEE Trans, Electron Devices, **44**, 104 (1997)

[Chandrakasan] A. Chandrakasan, W. Bowhill and F. Fox, Design of High-Performance Microprocessor Circuits, IEEE press (2001)

[Degraeve] R. Degraeve, G. Groesenken, R. Bellens, M. Depas and H. E. Maes, Thec. Dig. Int. Electron Devices Meet., pag. 863, (1995)

[Dekker] J. P. Dekker; A. Lodder, R. Zeller and A. F. Tatarchenko, *Solid State Comm.* **97**, 1013 (1996)

[Dongfang] Y. Dongfang and L. J. Xue, J. Appl. Phys., **93**, 9389 (2003)

[Eisenbeiser] K. Eisenbeiser, J. M. Finder, Z., J. M. Finder, Z. Yu, J. Ramdani, J. A. Curless, J. A. Hallmark, R. Droopad, W. J. Ooms, L. Salem, S. Bradshaw and C. D. Overgaard, Appl. Phys. Lett. **76**, 1324 (200)

[Frenck] H. J. Frenck, W. Kulisch, M. Kuhr and R. Kassing, Thin Solid Films, **201**, 327 (1991)

[Frosch] C. J. frosch and L. Derick, Proc. Electrochem. Soc., 457 (1957)

[Ghani] T Ghani, K Mistry, P Packman S Thompson; M Stettler, S. Tyagi, M. Bohr VLSI 174-5 (2000)

[Guha] S. Guha, E. Carter, M. A. Gribelyuk, N. A. Borjarczuk and M. A. Copel, Appl. Phys. Lett., **77**, 130 (2000)

[Guo] X. Guo, X. Wang, Z. Luo, T. P. Ma and T. Tamagawa, Tech. Int. Electron Devices Meet., **137**, 1999

[Ha] H. K. Ha, M. Yoshimoto, H. Koinuma, B. K. Moon and H. Ishiwara, Appl. Phys. Lett., **68**, 2965 (1996)

[Homg] M. Hong, J. Kwo, A. R. Kortan, J. P. Mannaerts and A. M. Sergent, Science reports, **283**, 1897 (1999)

[Hubbard] K. J. Hubbard and D. G. Schlom, J. Mat. Res., **56**, 228 (1196)

[Hubbard] K. J. Hubbard and D. G. Schlom, J. Mater. Res., **11**, 2757 (1996)

[Hubbard] K. J. Hubbard and D. G. Schlom, J. mater. Res., **11**, 2757 (1996)

[Klein] T. M. Klein, D. Niu, W. S. Epling, W. Li, D. M. Maher, C. C. Hobbs, R. I. Hedge, I. J. R. Baumvol and G. N. Parsons, Appl. Phys. Lett., **75**, 4001 (1999)

[kukly] K. Kukly, J. Ihanus, M. Ritala amd M. Leskela, Allp. Phys. Lett., **68**, 3737 (1996)

[Kwo] J. Kwo, M. Hong, A. R. Cortan, K. T. Queeney, Y. J. Chabal, J. p. Mannaerts, T. Boone, J. J. Krajewski, A. M. Sergent and J. M. Rosamilia, Appl. Phys. Lett., **77**, 130 (2000)

[Lee] P. F. Lee, J. Y. dai, K. H. Wong, H. L. W. Chan and C. L. Choy, Appl. Phys. Lett. **82**, 2419 (2003)

[Lee2] W. C. Lee and C. Hu, IEEE Trans. Electron Devices, **48**, 1366 (2001)

[Li] M. Li, Z. Zhang and S. A. Campbell, J. Appl. Phys., **98**, 54506 (2005)

[Li2] Ai-D. Li, Qi-Y. Shao, H. Q. Ling, J. B. Cheng, D. Wu, Z. G. Liu, N. B. Ming, C. Wang, H. W. Zhou and B. Y. Nguyen, Appl. Phys. Lett., **83**, 3540 (2003)

[Liebman] L. W. Liebman, M. S. mansfield, A. K. Wong, M. A. Lavin, W. C. Leipold and T. G. Dunham, IBM J. Res.& Dev., **45**, 651 (2001)

[Liu] J. P. Liu, P. Zaumseil, E. Bugiel and H. J. Osten, Appl. Phys. Lett., **79**, 671 (2001)

[Lucovsky] G. Lucovsky, Y. Wu, H. Niimi, V. Misra and J. C. Phillips, Appl. Phys. Lett., **74**, 2005 (1999)

[Ma] T. P. Ma, H. B. Bu, W. Wang, L. Y. Song, W. He, M. Wand. H. H. Tseng and P. J. Tobin IEEE Trans Dev. And Mat. Reliability, **5**, 1530 (2005)

[Martin] P. J. Martin, A. Bendavid and H. Takikawa, J. Vac. Sci. Technol. A, **17**, 2351 (1999)

[Miotti] L. Miotti, K. P. Bastos, C. Driemeier, V. Edon, M. C. Hugon, B. Agius and I. J. R. Baumvol, Appl. Phys. Lett., **87**, 022901-1 (2005)

[Nakahara] Y. Nakahara, VSLI symp., pag. 174, (1996)

[O'Connor] R. O'Connor, G. Hughes, R. Degraeve, B. Kaczer and T. Kauerauf, Semicond. Sci. technol., **20**, 68 (2005)

[Okada] T. Okada, M. Shajahan, K. Sawada and M. Ishida, Jpn. J. Appl. Phys., **44,** 2320 (2005)

[Ono] H. Ono, Appl. Phys. Lett., 78, 1832 (2001)

[Park] B. E. Park and H. Ishiwara, Appl. Phys. Lett., 82, 1197 (2003)

[Robertson] J. Roberson and C. W. Chen, Appl. Phys. Lett., **74**, 1168 (1999)

[Robertson2] J. Robertson, J. Vac. Sci. Technol. B, **18**, 1785 (2000)

[Roussel] P. Roussel; R. Degraeve, A. Kerber, L. Pantisano and G. Groeseneken, IEEE Intern. Reliability Phys. Symp. Proceeding 41st, 29 (2003)

[Scarel] G. Scarel, C. J. Hirschmugl, V. V. Yakovlev, R. S. Sorbello, C. R. Aita, H. Tanaka and K. Hisano, J. Appl. Phys., **91**, 1118 (2002)

[Hubbard] K. J. Hubbard and D. G. Schlom, J. Mater. Soc., **11**, 2757 (1996)

[Schroeder] T. Schroeder, T. L. Lee, J. Zegenhagen, C. Wenger, P. Zaumseil and H. J. Mussig, Appl. Phys. Lett., **85**, 1229 (2004)

[Seokhoon] K. Seokhoon, J. Y. Kim, J. Kim, J. Choi, H. Kang, C. bae and H. Jeon, Electrochem. Solid-State Lett., **9**, G40 (2006)

[Shannon] R. D. Shannon, J. Appl. Phys., **73**, 348 (1993)

[Stathis] J. H. Stathis, IEDM, pag. 167-70, (1998)

[Stathis2] J. H. Stathis, IEEE Trans. Device & Mater. Reliabil., **1**, 43, (2001)

[Stathis3] J. H. Stathis and D. J. DiMaria, Appl. Phys. Lett., **71**, 3230 (1997)

[Stathis4] J. H. Stathis, A. Vayshenker, P. R. Varecamp, E. Y. Yu, C. Montrose, J. Mckenna, D. J. DiMariaL.-K. Han, E. Cartier, R. A. Wachnik and B. P. Linder, Tech. Dig. VLSI Symp. pag. 94, (2000)

[Statis5] J. H. Stathis, B. P. Linder, R. Rodriguez and S. Lombardo; Microelec. Reliability, **43**, 1353 (2003)

[Sze] S. M. Sze, Physics of Semiconductor Devices, 2nd edition (Wiley, New York 1969).

[Tang] H. Tang, K. Prasad, R. Sanjines, P. E. Schimid and F. Levy, J. Appl. Phys., **75**, 2042 (1994)

[Wallace] R. M. Wallace, Appl. Surf. Sci. 231-232, **543** (2004)

[Weir] B. E. Weir, M. A. Alam, J. D. Dube, P. J. Silverman, A. Ghetti, F. Baumann, P. Diodato, D. Monroe, T. Sorsch, G. L. Y Timp, Y. Ma, M. Brown, Semicond, Sci Technol., **15**, 455 (2000)

[Williams] L. M. Williams and D. W. Hess, J. Vac. Sci. Technol., **A1**, 1810 (1983)

[Wu] Y. H. Wu, M. Y. Yang, A. Chin, IEEE Electron Device Lett., **21**, 341 (2000)

[www] http://public.itrs.net

[Xiang] W. Xiang, H. Lu, L. Yan, H. Guo, L. Liu, Y. Zhou, J. Jiang, H. Cheng and Z. Chen, J. Appl. Phys., **93**, 533 (2003)

[Yang] Y. S. Yang, S. J. Lee, S. H. Kim, B. G. Chae and M. S. Jang, J. Appl. Phys., 84, 5005 (1998)

II. Instruments and Characterization Techniques

TECHNIQUES D'ÉLABORATION ET DE CARACTÉRISATION

Ce chapitre est consacré aux techniques expérimentales utilisées lors de ce travail. L'objectif est de donner une vision générale de ces techniques en donnant leur principe, la manière de les utiliser et de les exploiter, et d'en extraire les informations utiles. Ce chapitre comporte deux parties, la première portant sur les techniques d'élaboration et le second sur les moyens de caractérisation.

Les procédés d'élaboration utilisés pour déposer ou faire croître les oxydes de grille ont été mis en œuvre dans une salle blanche niveau 3 du Centre de Haute Technologie des Matériaux à Albuquerque. Les outils utilisés sont décrits de manière détaillée, de même que les principaux paramètres expérimentaux accessibles lors de l'élaboration des couches minces d'oxyde. En particulier, les avantages et les limitations des techniques de dépôt et de recuit choisis dans cette étude sont argumentées et précisées.

Les techniques de caractérisation nombreuses et variées utilisées pour analyser les films font l'objet de la seconde partie. Toutes ces techniques ont été personnellement maîtrisées, sauf exceptions mentionnées dans le texte. Pour tous les outils de caractérisation utilisés, des exemples réels et concrets ont été donnés. Ces exemples font référence à la fois à la technologie Si/SiO_2 et aux technologies Si/high-k et ils sont directement reliés aux résultats expérimentaux que nous avons obtenus.

II.1. DEPOSITION TOOLS

In this section we describe the systems we have used to deposit and to grow either the oxide films or metal films. Particular attention has been paid to the ECR plasma reactor, because of its versatility for our applications.

II.1.1. Plasma deposition tools

II.1.1.1. General considerations

Many plasma geometries and plasma discharges have been developed over the last decades. The multi-dipolar microwave ECR and Distributed ECR (DECR) [Pelletier] [Pelletier2] [Arnal] was studied and developed for the first time by [Petit 85] and [Pichot 88]. Conventionally DECR, which combines multipolar magnetic field confinement and microwave excitation at ECR, appeared particularly well suited to the design of large area plasma sources. In a typical design the production of a plasma is obtained by applying, with a linear applicator or antenna, the microwave electric field along a multipolar magnetic structure providing the magnetic field intensity required for ECR coupling. However, attenuation of a traveling wave along the antenna leads to nonuniform plasma generation. The production of uniform plasmas therefore requires standing waves with constant amplitude along the linear applicators.

In order to circumvent the limitations of DECR plasmas, one possibility lies in the extension of the distribution concept, from an array of linear DECR plasma sources to a two-dimensional network of elementary ECR plasma sources. In this way, large area bi-dimensional plasma sources can be developed without any size limitation.
This objective can be achieved with multi-dipolar plasmas [Lacoste] whose principles are described as follows:

1. Uniform low-pressure plasmas are produced from a network of elementary, independent plasma sources sustained at ECR. These sources are described in detail by [Lacoste].

2. Distribution of microwave power in the elementary plasma sources is required. These plasma sources can be fed with microwaves, either from many microwave supplies driven independently, or from many independent microwave circuits after division of the microwave power delivered by a unique, high power microwave supply. Each microwave power transmission line includes a circulator with its matched load to absorb reflected power, a tuner for impedance matching, a matched vacuum feed-through, and a coaxial line.
3. The micro-wave multipolar plasma combines the concepts of plasma confinement using a multipolar magnetic structure and micro-wave excitation. For an electromagnetic wave of frequency ν and a static magnetic field **B,** perpendicular to the electric field of the electromagnetic wave, the gyration frequency of the electrons in the magnetic field is equal to the frequency of the microwaves (Electron Cyclotron Resonance ECR condition).

$$B = 2\pi\left(\frac{m_e}{e}\right)\nu \qquad \text{II.1}$$

In practice ν is the microwave frequency and B is the intensity of the magnetic field **B**, m_e is the electron mass and e is the electron charge.

The ECR source offers several advantages and process opportunities as compared to the more common parallel plate or rf-discharge or as compared to the conventional chemical process:

- High plasma density with low sheath potentials is created, so that the plasma density can attain values well above those of low-frequency rf-discharges.
- The ion impact energy with respect to the substrate can be controlled independently of the power source used to excite the plasma driven dc or rf source.

The use of multi-dipolar plasma sources in addition to ECR also offers the following advantages:

- Reduced magnetic field interactions between magnets.
- Reduced microwave interactions between elementary plasma sources. Therefore, the microwave power can be adjusted independently for each elementary source.

- Dense plasmas at any microwave frequency. Due to the propagation conditions of microwaves within the plasma, the plasma density is in fact limited to the critical density $n_c = \omega^2 \varepsilon_0 m_e / e^2$whose value is $n_c = 7.5 \times 10^{10}$ cm^{-3} at the microwave frequency $f_0 = \omega / 2\pi = 2.45$ GHz. ε_0 is the free space permittivity, m_e and -e are the electron mass and charge, respectively. The multi-dipolar sources produce plasmas with densities much higher than the critical density.
- Reduced edge effects. The possibility to adjust the microwave power injected to the elementary plasma sources at the periphery of the reactor allows compensation for the enhanced plasma losses at the network boundaries.
- Plasma breakdown at very low pressure (below 10^{-4} Torr).
- The perfect coupling of microwaves with the plasma in the region of ECR absorption, in addition to the perfect confinement of the fast electrons, allows plasma breakdown at a very low levels of microwave power (a few watts or less).

The diffusing plasma produced by a single elementary plasma cannot provide uniform surface treatments. Therefore these elementary plasma sources must then be assembled in different ways, e.g. networks of sources with alternate or identical magnetic polarities, rectangular or hexagonal networks, or other combinations. Examples of two-dimensional planar networks have been already presented in detail by [Lacoste]. The elementary plasma sources can also be assembled in a three-dimensional network, e.g. at the periphery of a cylindrical plasma reactor, as demonstrated by [Bechu], where the diffusing plasma in the central volume is produced from two rings of 10 elementary plasma source.

II.1.1.2. The Electron Resonance Plasma Reactor

The experimental multi-dipolar plasma reactor used to deposit or grow the materials we have studied in this thesis, is shown schematically in Figure II.1.

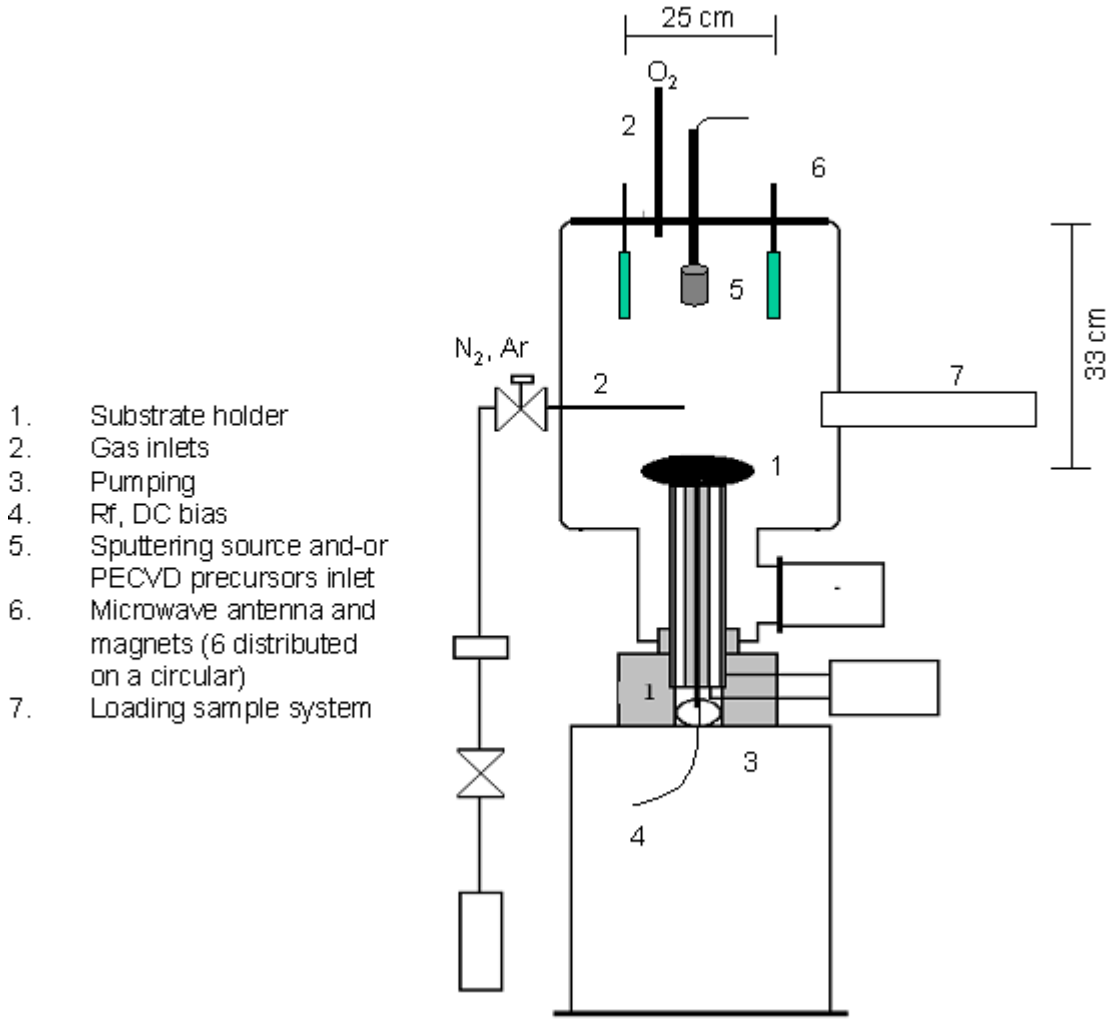

Figure II.1. *Cross-section of the ECR reactor.*

The reactor is composed of two chambers: the small one (the load lock on the right side of Figure II.1) is used to introduce the sample into the main deposition chamber. The first chamber does not have an independent pump for the vacuum but is constantly flushed with dry N_2.

The reactor is cylindrical, it is made of steel and 2 pumps are used to maintain the vacuum with a background pressure ~10^{-7} torr (~10^{-5} Pa). The main chamber contains different parts, which make the reactor versatile for different methods of deposition or growth:

1. A system of 6 elementary plasma sources sustained by microwaves at ECR is used to create the plasma. This particular geometry allows generation of a dense plasma. The magnets create a magnetic field B of 0.12 Tesla. This intensity of B is strong enough

to create, at the 2 poles of the antennas, the ECR conditions at a 2.45 GHz. The microwave power is supplied using 6 magnetic antennas themselves. The power of the generator is variable from 0 to 700 W and is distributed on the 6 applicators.

2. The substrate holder is electrically isolated from the rest of the chamber and is connected to an rf generator. It is possible to use the generator to independently apply a voltage to the sample surface so that ions in the plasma can be used to simultaneously densify the depositing film or (using O or N for example) to induce electrochemical growth of dielectrics (i.e. plasma assisted oxidation).
3. An rf sputtering probe (Taurus II), connected to an independent rf generator, is also available positioned in the center of the reactor top plate. This system can be used to sputter either metallic or dielectric materials.
4. 3 independent gas pipelines are available supplying O_2, N_2, Ar and SiH_4 for the plasma generation.

The combination of the different tools added to this reactor chamber makes our multi-dipolar plasma very versatile. Indeed it is possible to deposit or grow the materials in many different ways:

1. PECVD and also Low Pressure PECVD. The gas line can be eventually heated up if the precursor has a very low vapor pressure.
2. The Taurus II rf sputtering source allows traditional sputtering.
3. The substrate can be polarized and a material can be oxidized using the neutral oxygen created in the ECR plasma. This electrochemical method is available both in constant current and voltage. This technique is well known as plasma anodization [Peeters]

II.1.2. Electron Beam Evaporation tools

II.1.2.1. Electron beam fundamentals

In evaporation, the substrate is placed inside a vacuum chamber in which a block (source) of the material to be deposited is also located. The source material is then heated to the point where it starts to boil and evaporate or sublime. High vacuum is required to allow the

molecules to evaporate freely in the chamber, and they subsequently condense on all surfaces. There are different technologies of evaporation available to usually differing simply in method used to heat the material to be evaporated. In e-beam evaporation, an electron beam is aimed at the source material causing localized heating and evaporation. The advantage is that multi-constituent targets and also materials that have a high melting point can be easily evaporated. Furthermore the diameter of the target as well as the diameter of the electron beam can be extremely small, providing an economical advantage for the selected material.

However, it should be noted that the electron beam energies used are typical of those in an X-ray source and the radiation generated during the deposition process can damage the dielectric layers as they deposit. A post annealing process is typically used to remove the defects.

II.1.2.2. The CHA reactor

The CHA Mark 40 is a high vacuum stainless steel deposition tool consisting of two main parts: the vacuum system and the deposition chamber:

1. The vacuum system consists of a cryogenic pump with a pumping speed of 3000 l per second of air, a liquid nitrogen cooled baffle and liquid nitrogen reservoir with a cryo panel (LN_2 trap). The cryo pump and the LN_2 trap combined together allow us to reach a pumping speed of 15,000 l/sec, and a base vacuum of 10^{-7}–10^{-8} torr in less then 2 h.
2. The deposition chamber is equipped with 4 crucibles that can be filled with 4 different materials. This allowed deposition of different film on the same substrate, without open the chamber. An adjustable angle planetary fixture is installed to hold 12 four inch substrates and is designed to ensure uniformity of the deposited material on any kind of substrate in the limit of 1%. 4 quartz lamp heaters of up to 16 kW are installed to enable heating of the wafers to temperatures of 320 °C maximum (if required during the deposition). The electron gun operates with a CHA industries SR-10D power supply at a constant voltage of 10.2 kV and a current up to 1 A. The electron beam source is equipped with electromagnets to move the beam longitudinally and laterally so that it is possible to position the electron beam over

the entire area of the evaporation using a sweep controller. The maximum and minimum current delivered to the electromagnet determines the amplitude of the sweep. The amplitude and the frequencies of the sweep are adjustable by the operator. These parameters, properly programmed aid uniform distribution of the evaporation material upon the substrate.

The CHA Mark 40 can operate in automatic or in manual mode. The deposition process, once the sequence of the different deposition steps is set up, is fully automatic [CHA].

II.2. DIELECTRIC GROWTH AND ANNEALING TOOLS

II.2.1. The oxidation furnace

Thermal oxidation is generally carried out in either ultra-dry O_2 or so-called "wet" oxygen. For the case of Si, typically the temperature is raised to 800 – 1100 °C. This is also the only method of thin dielectric film which actually consumes some of the substrate as it proceeds. The growth of the film is due to the diffusion of oxygen though the growing film to the substrate/dielectric interface. As the thickness of the oxidized layer increases, the diffusion of oxygen to the substrate becomes more difficult: a parabolic growth regime defines the diffusion process, so that the film thickness depends on the square of the oxidation time. This is the classical process used to form silicon dioxide on a silicon substrate.
The thermal oxidation of different materials has been carried out using a horizontal quartz tube furnace situated in the CHTM clean room of class 1000 (Chapter II.4). Several samples of 2" maximum diameter can be loaded into the chamber, and an O_2 (dry oxidation) gas line is connected to allow the dry oxidation process. The temperature of the chamber was chosen as a function of the desired growth rate and final growth thickness.

II.2.2. The diffusion furnace

The diffusion furnace is an independent furnace, but with the same characteristics of the oxidation furnace. The main difference is that this furnace uses N_2 and O_2 gases to perform annealing processes instead of oxidation growth.

II.2.3. The Rapid Thermal Annealing

Rapid Thermal Annealing (RTA) RTP-600S [MPTC] is an alternative to standard furnace annealing. Its advantages include short heat-up and cool-down annealing times (from one second to 5 minutes), precise control of the annealing profile, wafer-to-wafer process cycle repeatability and energy efficiency. The heating cycle is controlled by a micro-controller that can be programmed. A maximum of 50 cycles are allowed for each user program. A typical annealing cycle is shown in Figure II.2.

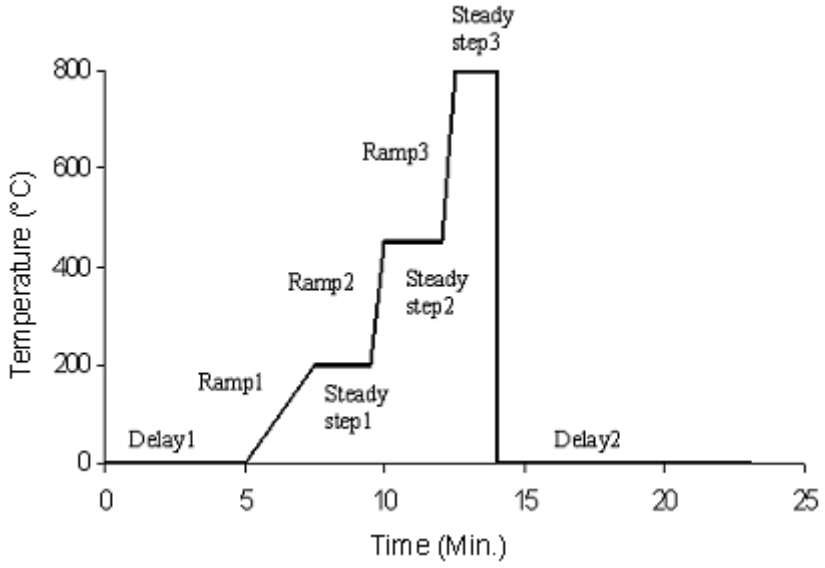

Figure II.2. *RTA standard cycle for an annealing temperature up to 800 °C.*

The delay step is a period during the cycle when the lamps in the oven are off and a purge gas is flowing into the system. Delays are used most frequently at the beginning and at the end of the cycles, respectively just after the door of the chamber is closed, and before opening it again.

The ramp step is a period of time during the cycle when temperature is rising or falling from one steady temperature to another. The Figure II.2 illustrates 3 programmed ramp steps. The first one is used to pre-heat the quartz lamps. The second one is necessary in all processes above 800 °C which cannot be easily controlled. Therefore a 30 seconds pre-heat

step at 400 °C is used before ramping (the 3rd ramp step) to the final desired temperature of 800 °C.

The steady step is a period of time during the cycle when the temperature is kept constant for a specified period of time

The RTP-600S system consists of a heating chamber unit with integrated computer control system and software. The wafer to be processed is placed on a quartz tray, which slides into a rectangular quartz chamber. The chamber is actually the annealing furnace: argon, nitrogen, oxygen, H_2 10%/balance N_2 ("forming gas") are the available gases. Two banks of lamps, one above and one below the quartz chamber, provide the energy to heat the sample.

The temperature stability is 2 °C, a maximum heating rate of 200 °C /s and cooling rate of 150 °C /s and a maximum dwell temperature of 1100 °C.

II.3. CHARACTERIZATION TOOLS AND TECHNIQUES

In this section we describe the different tools and the different methods we used to analyze the physical, electrical and optical properties of the materials we have studied in this thesis. Chapters II.3.1, II.3.2 and II.3.3 relate respectively to the ellipsometer, infrared and X-ray techniques and also provide some examples of the measurements. These methods of characterization were indispensable for our work, thus more details are provided.

II.3.1. Ellipsometry

Ellipsometry is a very old optical technique for studying surfaces and films. In microelectronics, it is widely used because it is a non-destructive and non-contact method of characterization, which implies reproducibility and almost no contamination of the surfaces that are analyzed.

The physical principle is based upon change in the polarization when a light beam passes from one medium into another that is not totally transparent. A part of the light is reflected and a part is not, so that the intensity of the reflected beam and its polarizability change. The ellipsometer studies this changes through the amplitude and the phase of the reflected beam. In fact, the amplitude and phase are the only physical variables that the ellipsometry tools

can determine. Thus information like the refractive index of the material and the thickness are determined *indirectly*.

II.3.1.1. General theory

The general theory of ellipsometry is described in Appendix A.

II.3.1.2. The Gaertner L125B

The ellipsometric instrumentation requires the following:

1. A monochromatic light source: typically a *laser light beam*
2. An optical element to convert un-polarized light into linear polarized light: polarizers are used in different ways. If it is used to convert unpolarized light to polarized light, it is called "*polarizer*". If it is used to determine the state of polarized light by locating the null it is called an "*analyzer*" [Spottiswoode].
3. An optical element to convert linear polarized light into an elliptically polarized light: the element used is an anisotropic optical element and it is typically called a "*quarter-wave plate*". The velocity of the wave depends on its orientation. Thus the wave plate has a fast and slow axis, both of which are perpendicular to each other and to the direction of propagation of the wave. The component of the wave which is aligned with the fast axis passes through the optical element faster than the component aligned with the slow axis. If the 2 components of the wave were in phase before passing through the wave plate (i.e. linearly polarized), then they will be out of phase when they emerge (elliptically polarized). If the thickness of the wave plate is chosen such as the phase difference is exactly 90° the wave plate is called *quarter-wave plate* or QWP.
4. A reflection from the sample of interest: The reflection is indispensable for reflection ellipsometry. The reflection of an electromagnetic wave can induce a phase shift from 0 to 360° and can attenuate the vector components of the wave.
5. The analyzer
6. A detector to measure the light intensity (or to determine the presence of null): photomultiplier or photodiodes are universally used for these purpose.

7. Calculation facilities to interpret the results in term of an assumed model

The ellipsometer used is a Gaertner L-125B , it shown schematically in Figure II.3.

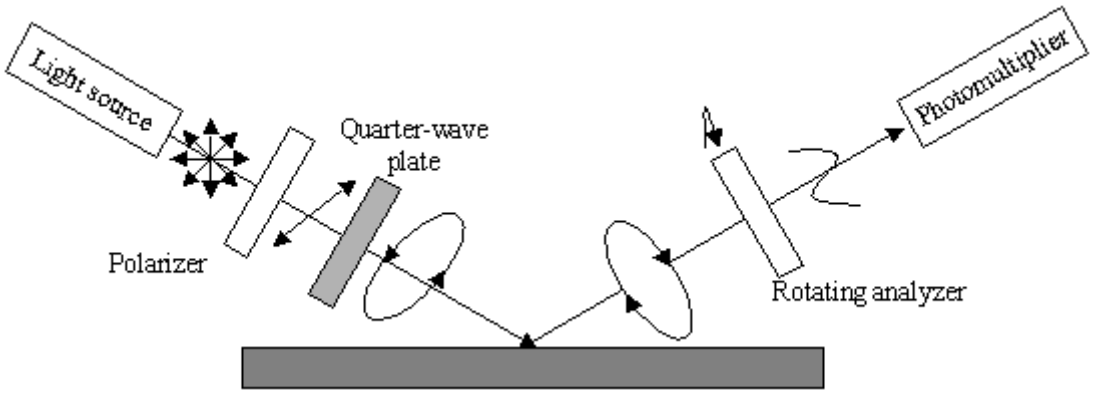

Figure II.3. *The Gaertner L-125B. In this type of ellipsometer only the analyzer rotates.*

This instrument is a photometer, which means it uses the values of the light intensity. In this case the polarizer is set at the fixed value of 45°. The laser beam is a red laser working at λ = 632.8 nm and the incidence and reflected angles are 50 or 70° and can be chosen independently. The QWP is fixed with the fast axis perpendicular to the plane of incidence. Only the analyzer rotates. The intensity I measured as a function of time t by the photomultiplier can be expressed as:

$$I(t) = I_0\left[1 + \alpha \cos 2A(t) + \beta \sin 2A(t)\right] \qquad \text{II.2}$$

where

$$A(t) = 2\pi ft + A_c \qquad \text{II.3}$$

with f is the angular frequency of the rotation and A_c is the constant phase offset. I_o is the average intensity and α and β are the Fourier coefficients. [Aspnes] showed that for a rotating analyzer instrument, the optimum precision is obtained when the incident beam on the rotating analyzer is circularly polarized. To obtain that condition the instrument itself

works with and without the QWP. Typically Ψ (Psi) is measured without QWP in place and Δ is measured with and without the QWP (depending of the value obtained). Ψ and Δ are defined in Appendix A. The Fourier coefficients α and β are given by

$$\alpha = -\cos 2\Psi \qquad \text{and} \qquad \beta = \sin 2\Psi \cos \Delta_m \qquad \text{II.4}$$

where Δ_m is the measured phase difference between the parallel and the perpendicular components of the light arriving to the analyzer. These equations can be also written as:

$$\cos \Delta_m = \pm\sqrt{\frac{\beta^2}{1-\alpha^2}} \qquad \text{and} \qquad \tan \Psi = \sqrt{\frac{1+\alpha}{1-\alpha}} \qquad \text{II.5}$$

If the QWP was not used, before the reflection the 2 components have no phase shift, so that the reflection phase shift is $\Delta = \Delta_m$. If the QWP was in place and the light incident on the sample was circular polarized, then it is necessary to add a retardation to the QWP to measure the value. Making measurements in both configurations allows one to determine both negative and positive values of Δ, for the most precise value of the angle.

II.3.1.3. An example

Most of the quantities we need to measure have been previously tabulated in handbooks. Unless the material is extremely reproducible (such as a single silicon crystal) the value of the optical constants depends on the crystalline structure, grain size, deposition method, etc. The value of the refractive index, n, for polycrystalline silicon can vary from 3.85 to 4.6 and the k value spans from 0.02 to 0.3 depending on the deposition temperature [Chandrasekhar]. This underlines the importance of measuring the substrate parameters prior to investigation of the film that we would like to study.

The substrate information

We assume a substrate (medium 3) covered or not covered by a thin film (medium 2 of thickness d) as shown in Figure II.4

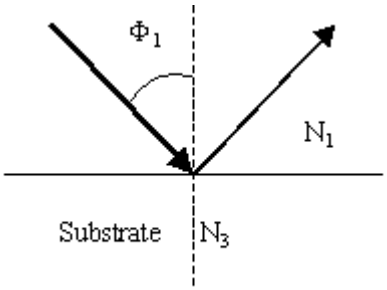

Figure II.4a. *A light beam reflected from a substrate medium 3*

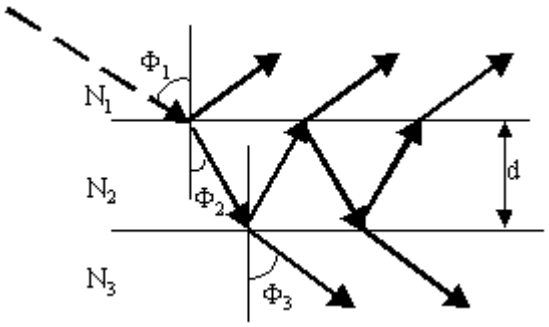

Figure II.4b. *Reflections and transmission schema of an electromagnetic wave passing through multiple mediums and surfaces. d is the thickness of the films and the medium 3 is the substrate*

To determine the properties of the film (n_2 and d) we must know first something about the substrate, more preciously the optical constants $N_3 = n_3\text{-}ik_3$. The complex value of ρ (defined in Appendix A) can be calculated from Eq. A.8 adapted to the scheme in Figure II.4b. Thus a value of N_3 is deduced using Eq. A.10. The problem of the substrate generally resolves into 2 different kinds of situations that can be represented in Figure II.4.

1. The substrate is a bulk material: this is the case of Figure II.4a. The ellipsometer has the software program to measure it. The program simply calculates n_3 and k_3 considering the substrate as an absorbing layer. The equations in Appendix A can be easily adapted to this case by changing the subscript identities.
2. A film of material with $k \neq 0$ can be considered an absorbing layer or a substrate, depending upon its thickness. Suppose that we are going to deposit an absorbing material onto a substrate gradually. When the absorbing layer thickness is zero, the Δ/Ψ values correspond to those of the substrate material. When the film is very thick, Δ/Ψ will be representative of the bulk deposited material. As we progress from no film, to a thin film to a thick film then, Δ/Ψ will move from the value characteristic of the substrate to the value of bulk film material. This behavior can be visualized schematically from Figure II.4b. N_3 is the substrate medium index and N_2 is the medium we are depositing. When the N_2 medium becomes thick enough the

structure can be analyzed as describe in the precedent section and represented in Figure II.4a. We show this in Table II.1.

Table II.1. *Variation of the optical indices for a stoichiometric film of LaAl deposited onto a Si substrate. The 0 nm thickness corresponds to the Si substrate. The 50° and 70° are the angles of incidence* Φ_1*, n and k are the components of the refractive index for an absorbing layer and* Ψ *and* Δ *are the angles in degrees measured by the instrument.*

	$\Phi_1 = 70°$				$\Phi_1 = 50°$			
	n	k	Psi (Ψ)	Del (Δ)	n	k	Psi (Ψ)	Del (Δ)
0nm	3.899	0.081	177	11	3.878	0.075	32	179
50nm	1.571	0.902	21	55	1.5	0.916	24	138
125nm	2.461	0.399	6	300	2.565	0.412	25	188
190nm	2.649	1.356	15	103	2.685	1.462	31	161
260nm	2.531	1.639	18	103	2.504	1.6	31	159
380nm	2.6	1.787	19	107	2.570	1.782	32	159
470nm	2.581	1.961	21	109	2.519	1.958	32.88	158
580nm	2.530	2.070	22	109	2.496	2.041	33	158
700nm	2.521	2.113	22	109	2.532	2.147	34	158
1121nm	2.497	2.211	23	110	2.465	2.262	34	158
1425nm	2.497	2.187	22.63	109.94	2.496	2.181	33.91	157.93

In this case we have deposited a film of LaAl (i.e. Chapter III) onto silicon. To be really careful in determining the values of Ψ and Δ, we performed 2 different measurements: one with the angle of incidence (coupled with the angle of the analyzer) at 50° and one at 70°. We will not discuss the evolution of the angle but we invite the reader to focus his attention on the evolution of the n and k indices as a function of the material (LaAl or medium layer 2 if we refer to the Figure II.4) thickness. After the LaAl reaches a thickness greater than 1000 nm, the n and k values do not seem to evolve, so that we can confirm that the Si+LaAl film can be considered as a monolithic substrate. So n=2.497 and k=-2.187 are the indices of the effective substrate comprised of our "bulk" deposited material.

The transparent film information

Now we consider having a substrate covered with a film as suggested in Figure II.4b. Medium 1 is the air, medium 2 is a thin layer of SiO_2 and medium 3 is our substrate (Si+LaAl). We shall call a film transparent if the extinction coefficient $k_2 = 0$. With the given values of n_3, k_3, n_2 and k_2 and thickness d we can use the equations given in Appendix A to calculate the expected value of Ψ and Δ. Figure I.5 illustrates the Δ/Ψ trajectory for SiO_2 on a Si+LaAl substrate. An unknown thickness of silicon dioxide can be determined by comparing the measured values of Δ and Ψ with this curve. For a film with k = 0 (i.e. SiO_2), the thickness d is given by:

$$d = \frac{\lambda}{2\sqrt{n_2^2 - \sin^2 \Phi_1}} \qquad \text{II.6}$$

where λ is the wavelength of the light beam. For a Δ = 109.1 and Ψ = 22.83 and n_2 = 1.46 (typical value for thermally grown SiO_2) the thickness is d=283 nm. For larger thicknesses the trajectory in Figure II.5 retraces the same path (periods). Thus to determine the actual thickness from Ψ and Δ it is necessary to know the appropriate period, which means to have an idea of the thickness. Different methods can be used to estimate this, such as oxidation time, deposition time, alpha-step measurements …

In Eq. II.2 we notice that the period depends on λ , on the angle of incidence and on the index of the film. If one has the liberty to vary either the wavelength or the angle of incidence, a different set of possible thicknesses would be obtained. The value that matches both lists is then the correct value. Unfortunately our instrument does not provide an automated system to change λ so that we cannot carry out ***spectroscopic*** measurements.

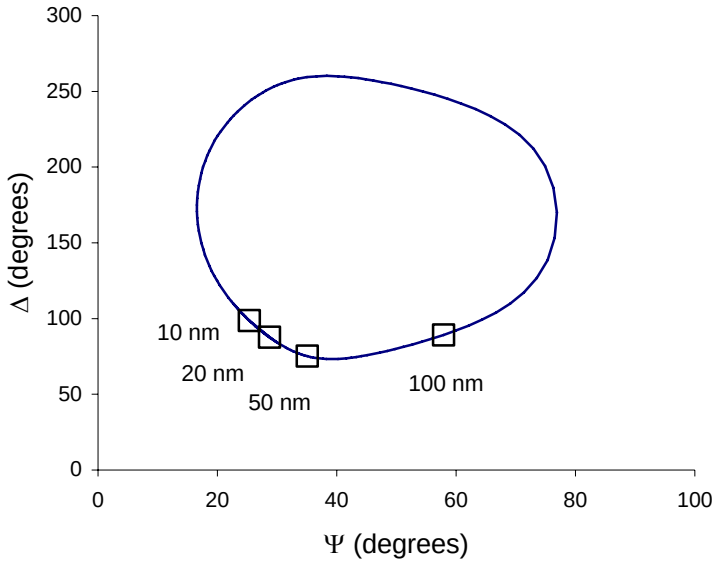

Figure II.5. *Δ/Ψ trajectory for SiO_2 deposited on a Si+LaAl substrate with an angle of incidence $\Phi_1 = 70°$ and a light wavelength of 632.3 nm. The solid line indicates the Δ/Ψ trajectory, and the square dots represent the increment of thickness of SiO_2.*

Figure II.5 shows the Δ/Ψ trajectory for a specific refractive index (1.46). Other values of the index n_2 would give different trajectories as shown in Figure II.6.

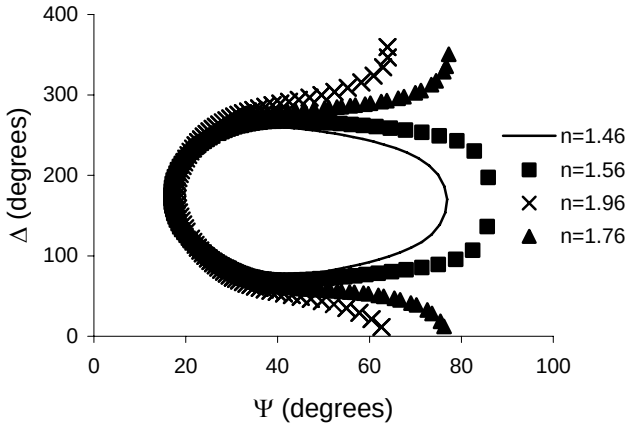

Figure II.6. *Δ/Ψ trajectories for films with different indices of refraction n_2 on a substrate medium of Si+LaAl. Only one period per refractive index is shown.*

Finally we analyzed the case in which both n_2 and d are not known.

Δ/Ψ gives us two numerical values, so that is possible to calculate two variables or constants that are unknown. If the material we investigate is transparent (most oxides are transparent at λ = 632.8 nm) $k_2 = 0$ so that $N_2 = n_2$. Figure II.6 can be used to fit the value of Δ/Ψ to determine both the thickness and the refractive index of the material.

The optical properties of all sample measured have been analyzed using the methods described above and considering that:

1. The [Gaertner] ellipsometer allows only single-wavelength measurements λ = 632.8 nm
2. Thicknesses of 40 nm or smaller are almost impossible to measure, if one does not know the refractive index of the film. In this case the software program coupled with the ellipsometer requires introduction of the refractive index, which becomes a constant and not a variable. The same can be done if one knows the thickness of the material and is just interested to see the differences in the refractive index.
3. Both the refractive index n and the thickness d can be measured for a transparent film (k = 0), respecting the limits described in the above sections 1 and 2.

Thus no further details other than the results will be provided in the ensuing chapters.

II.3.2. Infrared absorption

The term "infra red" covers the range of the electromagnetic spectrum between 0.78 and 1000 μm. In the context of infrared spectroscopy, wavelength is measured in "wavenumbers" which have the units cm^{-1}.

It is useful to divide the infrared region into three sections; *near*, *mid* and *far* infrared (Table II.2). The most useful IR region for vibrational studies in solids lies between 4000 – 400 cm^{-1}.

Table II.2. *The Infrared spectrum*

Region	**Wavelength range** (μm)	**Wavenumber range** (cm^{-1})
Near	0.78 – 2.5	12800 – 4000
Middle	2.5 – 50	4000 – 200
Far	50 –1000	200 – 1

II.3.2.1. General Considerations

IR radiation does not have enough energy to induce electronic transitions in dielectrics as one observes with UV radiation. Absorption of IR is restricted to compounds with small energy differences in the possible vibrational and rotational states. This fundamental one-phonon absorption process is associated with the electrostatic motion of opposite charges which produce an oscillating electric field with which the incidence radiation can couple. Materials like the fused silica or the sapphire are considered ionic (or at least only partially covalent). Normally, the infrared photons couple only to the transverse vibrational modes of the network since the electric and magnetic fields associated with the photon are perpendicular to the direction of propagation. For normal incidence, then, longitudinal excitations (i.e. in the direction of the propagating wave) are not possible. If the incident light is not normally incident to the plane of the film, the electric field associated with the vibrational mode can be dissociated into two mutually orthogonal components, one of which is now in the direction of the normal to the film and therefore excites longitudinal modes (longitudinal optic, LO modes). The remaining component is at 90° and so excites the transverse vibrations (transverse optic, TO, modes) [Berreman 63].

In Table II.3 we tabulate the acoustic and optical phonon frequencies for the homopolar (single compound) covalent material, silicon. For a molecule to absorb IR, the vibrations or rotations within it must cause a net change in the dipole moment of the molecule. The alternating electrical field of the radiation interacts with fluctuations in the dipole moment of the molecule. If the frequency of the radiation matches the vibrational frequency of the molecule then radiation will be absorbed, causing a change in the amplitude of molecular vibration.

Table II.3. *Absorption mode assignment in silicon [Johnson]*

Wavenumber (cm^{-1})	Peak energy (eV)	Phonon
1448	0.1795	3TO
1378	0.1708	2TO+LO
1121	0.1614	2TO+LA
964	0.1195	2TO
896	0.1111	TO+LO
819	0.1015	TO+LA
740	0.0917	LO+LA
689	0.0756	TO+TA
610	0.0702	Lo+TA

Various types of vibrations may be considered: stretching, bending and rocking. Details of the geometrical configurations and optical frequencies associated with these vibrations are described in appendix B.

II.3.2.2. The Nicolet 760 spectrometer

The spectrometer used was a Nicolet 760, equipped with a Michelson interferometer. Fast Fourier transform analysis is employed. The schematic of the instrument is shown in Figure II.7.

The chamber in which the sample is loaded is purged constantly with N_2 gas, so that the CO_2 and water absorption lines in the IR spectra are minimized or totally eliminated. Both the KBr beam splitter and the KBr detector allowed measurements over the spectral range 400 to 7000 cm^{-1} (0.25 to 1.4 μm). The resolution in the wavelength for all measurements was set to ± 2 cm^{-1}

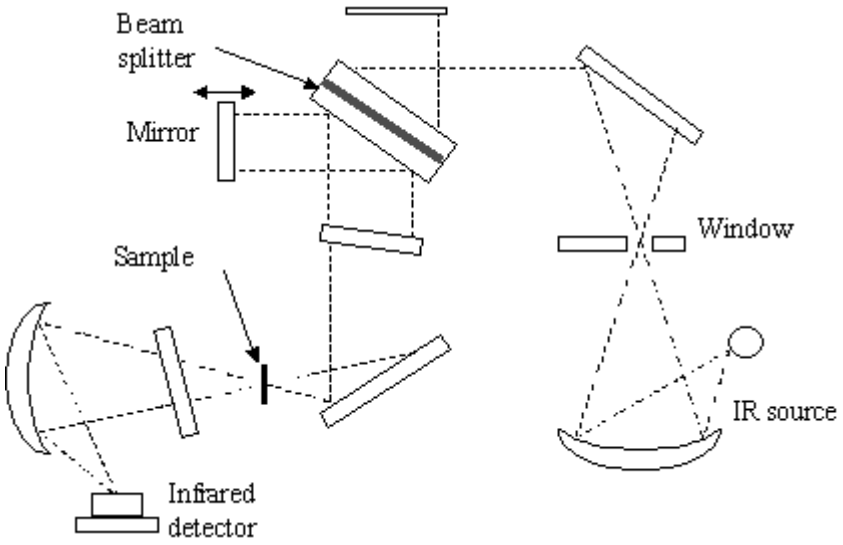

Figure II.7. *Schematic view of the Nicolet 760 IR spectrometer.*

II.3.2.3. An example

The IR region of interest for the oxides that we have analyzed ranges from 400 to 4000 cm^{-1}.

Absorption bands in the region from 400 to 2500 cm^{-1} can arise from stretching vibrations between hydrogen and some other atoms with a mass of 19 or less. The 2700 - 1850 cm^{-1} region is usually associated with multiple bands or with limited types of functional groups. The 1950 to 1450 cm^{-1} region exhibits IR absorption from a variety of double-bonded functional groups. Finally the 1300 to 350 cm^{-1} region is the most important region and is termed "**the fingerprint region**". Absorptions in this region include the contribution from complex interactive vibrations and network vibrations. A good match between the IR spectra of 2 compounds in the fingerprint region strongly indicates that they have the same molecular structures.

The Table II.4 summarizes the location of the most common IR bands of interest in the microelectronic materials.

Table II.4. *Location of some IR bands of interest.*

IR Frequency region (cm^{-1})	Type of bond
4000 - 2500	O - (atom with mass of 19 or less) stretching
3300 - 2800	C - H stretching
2260 - 2100	C ≡ C
2260 - 2220	C ≡ N
2000 - 1900	C = C = C
2250 - 2100	Si - H
1870 - 1550	C = O stretching
1690 - 1620	C = C and C = N
1650 - 1400	C - C stretching within the ring
1660 - 1260	NO_2 containing groups, asymmetric and symmetric stretching
1300 - 350	O stretching, rocking and bending for most known oxides

We consider a 2 or a 4" Si wafer with a film of SiO_2 thermally grown on its top, polished surface using the furnace describe in the chapter I.1.2 and using a pure O_2 atmosphere. The growth temperature was 900°C and the oxide thickness was 79.8 nm. Since both front and back surfaces of the wafer were oxidized, a dilute solution of 1:1 HF and de-ionized H_2O was used to de-oxidize the un-polished surface.

For each sample, we measure at least 4 spectra:

1. The substrate spectra (Figure II.9a) also called reference or background spectra. This measurement consists in cleaving a piece of the Si wafer after removing the oxide from both the polished and un-polished surfaces then measuring the IR absorbance in two different ways
    - The IR incidence bean is perpendicular to the oxide surface, so that only the TO vibrations are observed.
    - The IR incidence beam is 65° inclined compare to the oxide surface, so that both TO and LO vibrations are observed. The reason of the choice of the 65° is to maximize the intensity of the LO peak.

2. The sample spectra (Figure II.9b) contain both the background and the oxide. Obviously for the oxide we also have 2 different IR absorbance measurements:
    - The IR incidence beam is perpendicular to the oxide surface, so that only the TO vibrations are observed.
    - The IR incidence bean is 65° inclined compare to the oxide surface, so that the TO and LO vibrations are observed.

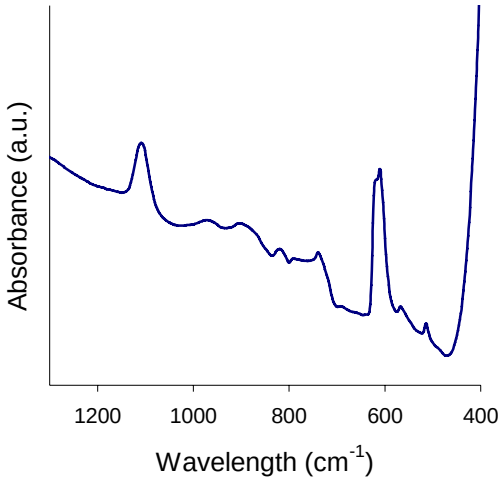

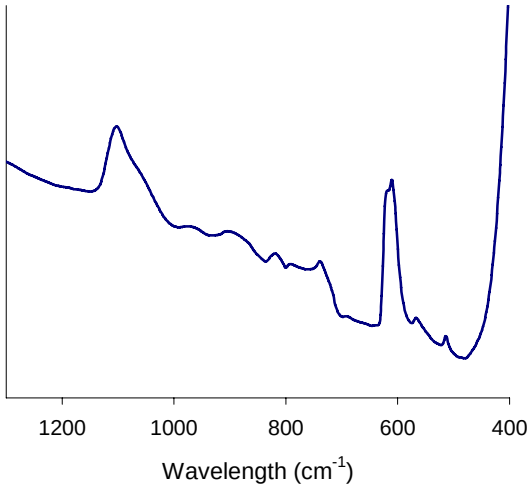

Figure II.9a. *Si absorbance spectra, or reference spectra for the measure that we are concerned about.*

Figure II.9b. *Si+SiO_2 absorbance spectra.*

The measurements were obtained in the ***transmission*** mode. The spectra typically shows the *absorbance* (A), which is defined by the following equation

$$A = \log\left(\frac{1}{T}\right) \qquad \text{II.7}$$

where T is the transmission coefficient.

To obtain only the spectrum associated with SiO_2, the absorbance reference spectra were subtracted from the sample spectra.

The subtraction process is extremely critical, because an over estimated subtraction or an underestimated subtraction can produce artificial absorbance peaks. In Figure II.10 we show 3 different subtractions using the same reference and the same sample. Spectrum "a" is the sample when the Si background was over subtracted, spectrum "b" is the sample when the Si background was under subtracted and spectrum "c" is the correct subtraction absorbance.

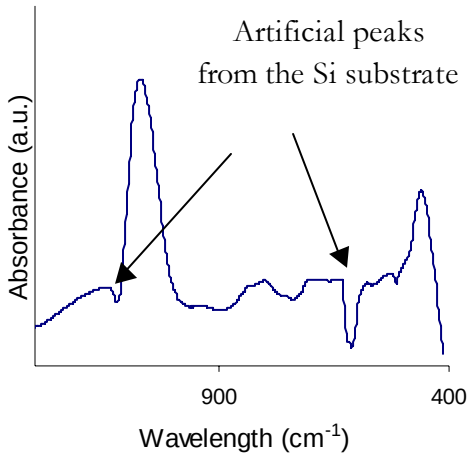

Figure II.10a. *SiO_2 spectrum after an over subtraction of the Si substrate. The SiO_2 thickness is 48 nm.*

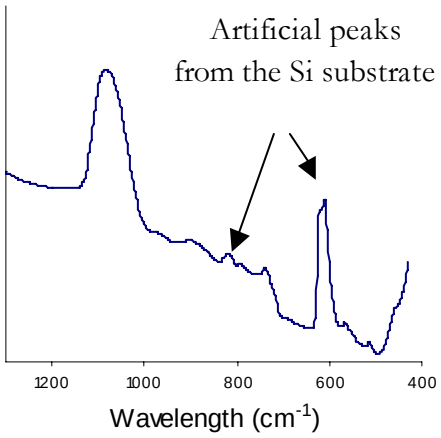

Figure II.10a. *SiO_2 spectrum after an under subtraction of the Si substrate. The SiO_2 thickness is 48 nm.*

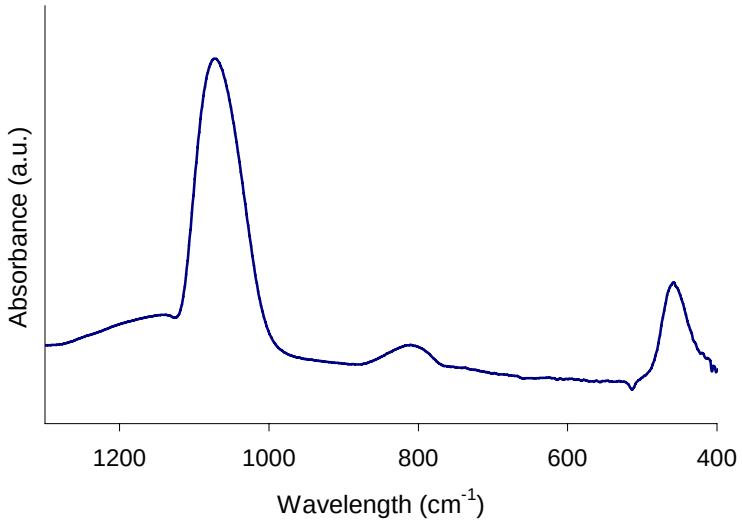

Figure II.10c*. SiO_2 spectrum after a correct subtraction of Si substrate. The thickness of the SiO_2 is 48 nm Only 3 absorbance resonance peak are associated with the SiO_2 structure.*

For the substrate, the Si -Si vibration is located at 607 cm^{-1} and the oxygen interstitial stretching mode in the Si matrix is at 1105 cm^{-1}. Figures II.10a and II.10b clearly show how an incorrect subtraction of the Si peaks does not remove the lines originating from the substrate. A correct subtraction shown in Figure II.10c does remove the Si substrate associated lines and leads to a good representation of the oxide structure.

Using the Si substrate gives us a great advantage. Since Si is a well-known material the structure and the IR active modes are well known.

We next consider a room temperature deposited TiO_2 film on silicon. After deposition the sample received post-annealing at 800 °C in N_2 atmosphere for 30 min. The Si -O peak at 1100 cm^{-1} changed because the oxygen concentration in the Si changed due to the annealing process, so that in fact the Si reference can induce the effects presented in the Figures II.10a and II.10b. There are 2 solutions for this undesirable effect:

- during the subtraction process we focus our efforts on trying to minimize the 607 cm^{-1} peak instead of the 1100 cm^{-1}
- The Si reference is subjected to the same post-annealing treatment.

We better understand the reasons that lead us to carefully obtain a reference spectrum for each sample that is made from a different Si wafer. The amount of impurity in the Si substrate, such as the oxygen, changes as well as the Si wafer thickness (we will see later how the thickness is associated with the intensity of the IR absorbance peak). Therefore the best approximation is to use a piece of Si of the same wafer as the sample in the background subtraction process.

Interpretation of the IR spectrum for a "standard" case: SiO_2. The IR technique actually allows to obtain information about the structure of the material, its density and the bridging bond angle or the distance between the atoms (Si –O -Si for example). For amorphous silica the frequencies of vibration of the atoms have been given by [Lehmann]. Using the central and non-central force model [Lehmann] it is possible to predict the vibrational frequencies of the different network modes. For the TO asymmetrical stretching frequency ω_{TO} of oxygen in SiO_2, it is given by:

$$\omega_{TO} = \frac{1}{2\pi c}\sqrt{\frac{2}{m}\left(\alpha \sin^2\left(\frac{\theta}{2}\right) + \beta \cos^2\left(\frac{\theta}{2}\right)\right)} \qquad \text{II.8}$$

Where m is the mass of the oxygen atom expressed in kg, θ is the angle of the Si -O -Si bond and α and β are the central and non-central force constants expressed in Nm^{-1}, c is the velocity of light. Values of $\alpha = 613$ and $\beta = 102$ Nm^{-1} were estimated from experiment by [Devine]. If we assume θ = 144°, we conclude that the TO vibrational mode is expected at 1090 cm^{-1}. The same procedure can be applied to determine the frequencies of the other vibrational modes [Lehmann].

In Figure II.11 we show the spectrum for a 79.8 nm thick SiO_2 film grown on Si at 900 °C. We notice that the location of the stretching mode (1072 cm^{-1}) is slightly displaced from the value of 1090 cm^{-1} [Mozzi 69]. The reason for this displacement may be found in two effects a) the film density depends upon the growth conditions and particularly the growth temperature; b) multiple reflections within the thin film lead to a "geometric" shift of the absorption peak. The latter effect, which is preponderant in thin dielectric films, was studied in detail by [Martinet].

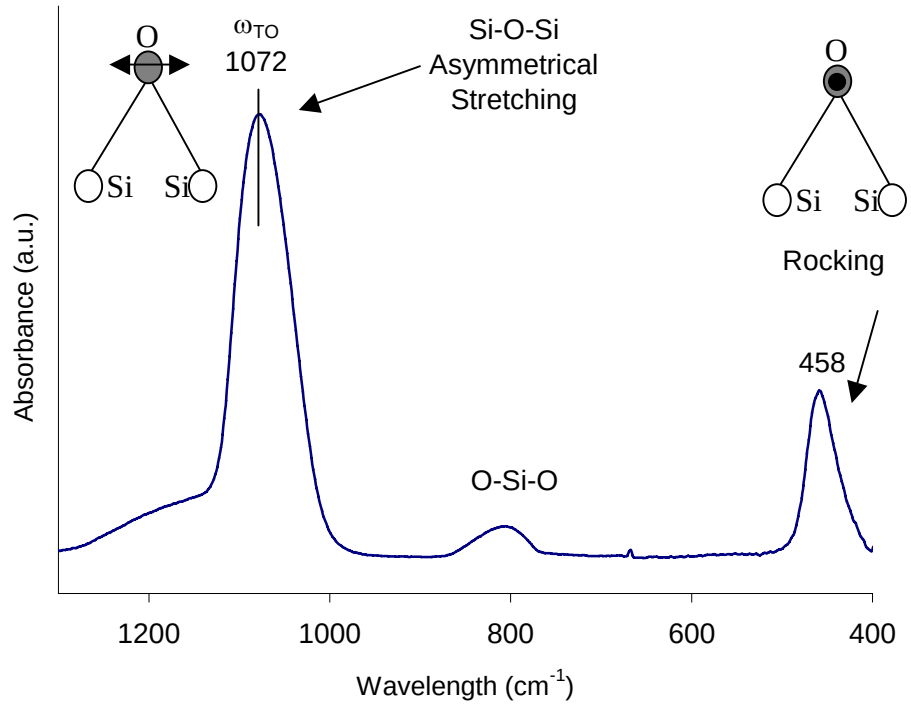

Figure II.11. *Measured SiO_2 IR absorbance spectrum for normal incidence for an oxide of 79.8 nm.*

The FWHM is a measure of the crystallinity of the sample. As a general rule, more the sample is amorphous more the FWHM will be larger.

We analyze now the peaks that are not normally excited for normal incidence. If the 2 following conditions exist:

- the thickness of the oxide respects the following equation:

$$\frac{2\pi d_{ox}}{\lambda_0} << 1$$

  where λ_0 is the wavelength of the incident beam in vacuum,

- the incident beam is not perpendicular to the oxide surface, but forms an angle with the normal vector to the surface or the incident beam is p polarized (the electric field vector lies in the incidence plane),

it is possible to measure the LO vibrational peaks, if they exist. For SiO_2, an important LO asymmetrical stretching is expected at 1255 cm^{-1}. A less intense peak at 505 cm^{-1} is also expected to be associated with the bending mode.

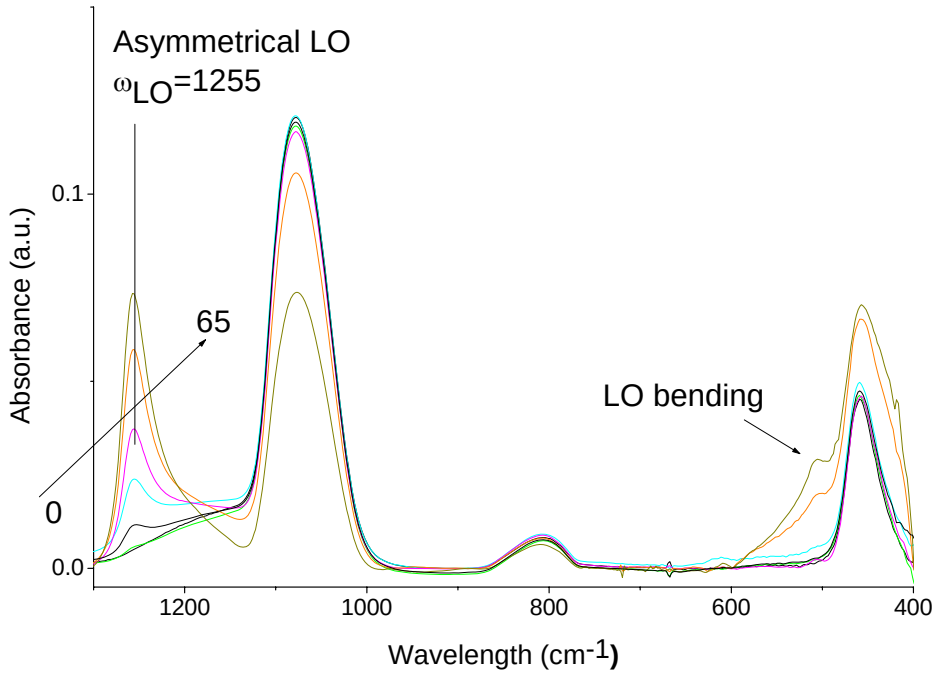

Figure II.12. *Oblique incidence IR absorbance spectra of SiO_2 film 79.8 nm thick. The angles of incidence were 10,20,30,40,50,65 degrees. The maximum intensity for the LO peak corresponds to an incident angle of 65 degrees.*

In Figure II.12 we show a typical SiO_2 spectrum when the angle of incidence is varied from 0 to 65°. Our experience shows that the maximum intensity of the LO peak is detected for an angle of 65°. This experiment clearly shows how the LO peak depends on the angle of incidence. [Lehmann] also published the formulae for LO peaks.

Figure II.12 also shows that the effective FWHM of the LO peak is smaller than the FWHT of the TO peak and that the TO peak intensity decreases with the angle of incidence whilst the LO increases.

The thickness of the material can also be approximately estimated using the IR absorbance. As a general rule we use the TO asymmetrical stretching mode because it is the most intense peak which is proportional to the density of the material and to a coefficient that takes into account the oscillator strength of the material. Then, if the density of the material is known, the thickness is known. In Figure II.13a we show the IR absorbance spectra for 2 different SiO_2 thicknesses in the region of 900 - 1200 cm^{-1} and also we trace the intensity of the IR absorbance with the SiO_2 thickness in Figure II.13b.

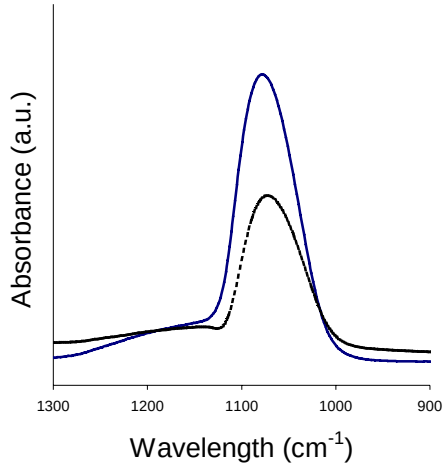

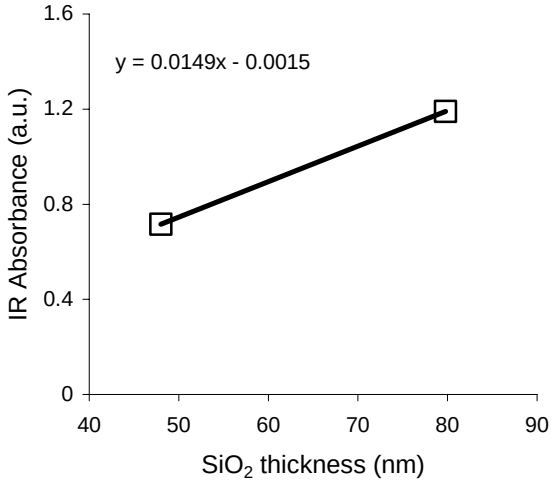

Figure II.13a. *The IR absorbance spectra for two different SiO_2 thicknesses: the dotted line is for 48 nm of SiO_2 and the solid line is for 78.9 nm of SiO_2.*

Figure II.13b. *The IR symmetrical TO peak intensity versus the thickness of the SiO_2.*

The equation for the line in Figure II.13b indicates that, when the SiO_2 thickness is 0, the intensity of the IR beam is 0.0015. This value can be considered as "noise" for our instrument. We conclude that at least 1 nm of SiO_2 is measurable. Extensive studies of the relationship between the intensity of the LO and TO and the SiO_2 thickness can be found in the literature [Martinet]

In conclusion from both TO and LO peaks (from normal and oblique IR beam incidence) we can retrieve the following information about the films:

- Studing the active LO and TO modes in the region of 1400 - 350 cm^{-1}, we obtain enough information to characterize the structural and molecular properties of the oxide.
- The TO mode can been used to estimate the thickness of the oxide.
- The LO mode can been used to obtain information about the roughness of the oxide (this will be discussed in the chapter III)
- We did not investigate the relation between the thickness of the sample and the position of the vibrational frequencies. This information is available in [Devine].

II.3.3. Electrical analysis

The aim of this paragraph is to give an understanding of the main variables that we have used during our studies. The dielectric constant and the leakage currents that characterize a gate oxide are generally measured using a Metal Oxide Semiconductor capacitor structure such as that illustrated in Figure II.14.

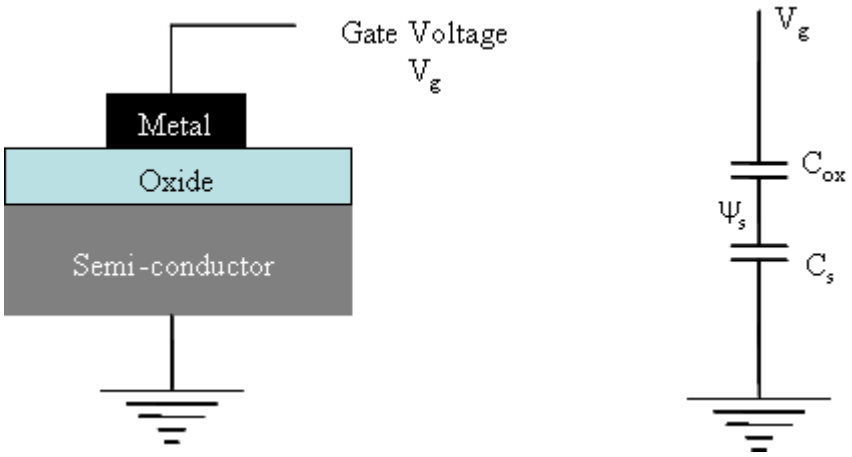

Figure II.14. *Ideal MOS capacitor. C_{ox} is the capacitance of the oxide, C_s is the semiconductor capacitance and ψ_s is the surface potential of the semiconductor.*

II.3.3.1. The Keithley 590 analyzer

The Keithley Model 590 C - V Analyzer measures capacitance versus voltage (C - V) and capacitance versus time (C - t) characteristics of semiconductor devices. The Model 590 has been tailored to the requirements of semiconductor device testing. The test frequencies can be chosen as either 100 kHz or 1MHz, the measured capacitance between 10 pF to 10 nF and conductance between 0.1 nS to 1 μS. The instrument is equipped with internal software to correct for errors from cables, connection and switching paths.

II.3.3.2 Capacitance versus voltage analysis C(V)

Referring to the Figure II.14, the MOS characteristic can be simply determined by measuring the capacitance C (the oxide capacitance C_{ox} and the semiconductor capacitance C_S) versus the gate voltage V_G (Figure I.15).

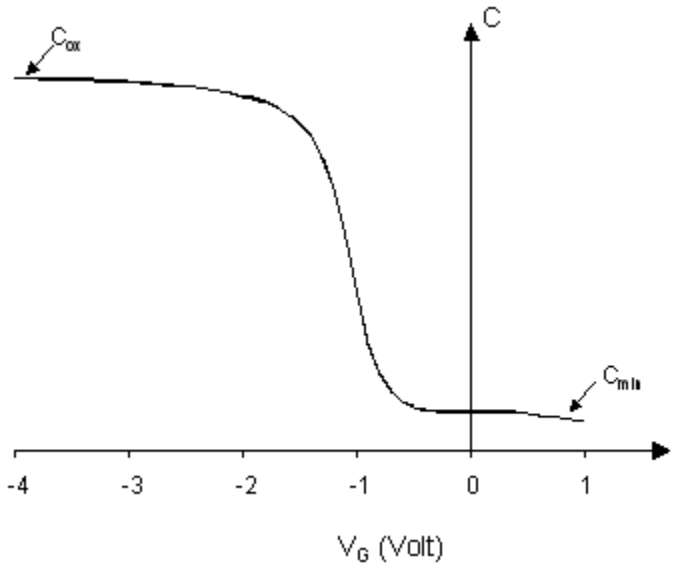

Figure I.15. *MOS capacitance characteristic C(V) for a SiO_2 gate oxide of 48nm.*

For the range of dielectric thickness that we used (a few tens of nm) C_{ox} and C_{min} are easily measurable and the relation between the oxide thickness d_{ox} and the capacitance is given by the equation II.9,

$$C_{ox} = \frac{\varepsilon_{ox}\ \varepsilon_0\ S}{d_{ox}} \qquad \text{II.9}$$

where S is the surface area of the metal gate contact. C_{min} allows measurement of the inversion capacitance of the semiconductor, which is in series with the oxide capacitance.

$$\frac{1}{C_S} = \frac{1}{C} - \frac{1}{C_{ox}} \qquad \text{II.10}$$

We can also calculate the depletion length region W_{SC} of the semiconductor:

$$C_S = \frac{\varepsilon_{SC}\ \varepsilon_0\ S}{W_{SC}} \qquad \text{II.11}$$

where ε_{sc} is the semiconductor capacitance. W_{SC} is related to the concentration of the dopant (N_a):

$$W_{SC} = \sqrt{\frac{2\ \varepsilon_0\ \varepsilon_{SC}\left(2\ \psi_B\right)}{q\ N_a}} \qquad \text{II.12}$$

where Ψ_B is defined by equation II.13.

$$\psi_B = \frac{kT}{q} \ln \frac{N_a}{n_i} \qquad \text{II.13}$$

where n_i represents the intrinsic concentration of the silicon.

Equations II.12 and II.13 provide the value of the substrate dopant concentration, N_a (ideally supposed uniform), in the silicon.

Now we are able to trace the ideal MOS capacitance characteristic. When we say ideal, we assume that there are no charges at the interface between the oxide and the silicon (no interface states) and no charges present in the oxide. This ideal curve is traced in red and dotted line in Figure II.16, while in black we show again the measured SiO_2 capacitance on silicon represented in Figure II.15.

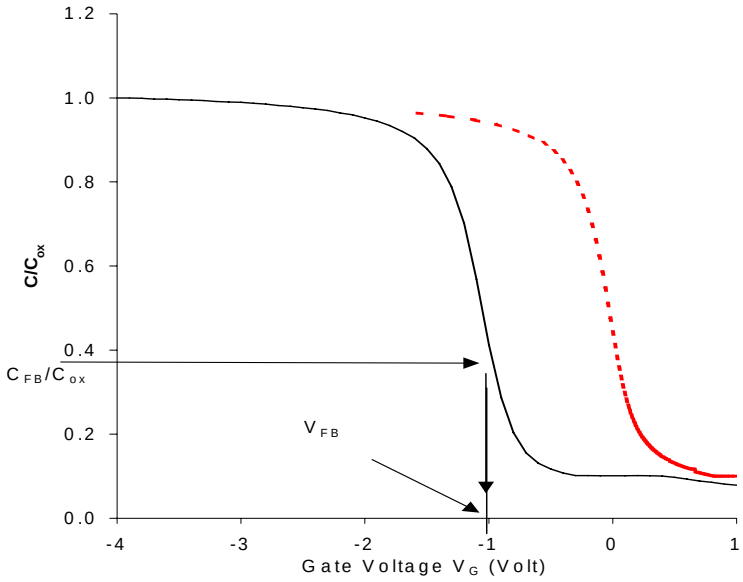

Figure II.16. *C(V) of an ideal MOS capacitor (red dotted line) and for the measured 48nm SiO_2 MOS (black line).*

The main difference between these 2 curves is represented as a shift of the gate voltage. The voltage used to determine the differences in the V_g is called the flat band voltage V_{FB} which can be determined as follows. First we define the Debye length L_D and the flat band voltage V_{FB} as:

$$L_D = \sqrt{\frac{\varepsilon_{sc}\varepsilon_0 (kT/q)}{qN_a}} \qquad \text{II.14}$$

$$\frac{1}{C_{FB}} = \frac{1}{C_{ox}} + \frac{L_D}{\varepsilon_{SC}\ \varepsilon_0\ S} \qquad \text{II.15}$$

where T is the temperature expressed in K, and k is the Boltzmann constant. We deduce, from the experimental curve shown in Figure II.16 the value of C_{FB}/C_{ox} and so we can graphically deduce the value of $V_{FB.}$

V_{FB} is a fundamental variable in the MOS characterization, because it is related to:

- The difference of the work functions Φ_{ms} of the metal used for the gate contact and the semiconductor. Some numerical values of the work functions are published by [Sze]
- The charges in the oxide or at the interface between the oxide and the semiconductor. These first charges can be "fixed" or "mobile". In the latter case this would be due to mobile, charge species in the oxide. If the experimental curve is "stretched" compare to the ideal curve, a further charge source is evidenced and this is related to the defect states located at the interface between the semiconductor and the dielectric. If the experimental curve is just simply shifted, only fixed charge in the oxide is present. It is also possible to have a combination of the 2 effects. Unfortunately a simple C(V) does not enable full analysis of the charges. The V_{FB} can be expressed as:

$$V_{FB} = \Phi_{ms} - \frac{Q_{ox}}{C_{ox}} \qquad \text{II.16}$$

where Φ_{ms} is defined in the chapter I.1.4 (Eq. I.3).

Equation II.16 gives the value of the charge density assuming no interface states.

NB: the instrument permits measurement of the conductance G at the same time that the capacitance is acquired.

II.3.3.3. Current versus voltage analysis I(V)

Current versus voltage I(V) measurements were used to determine the electrical characteristics of the oxide, for example, the leakage current for a chosen voltage and the maximum electric field E_c which the oxide will tolerate before breakdown. As a general rule the leakage current density (A cm^{-2}) at an applied electric field of ± 1 MV cm^{-1} was taken as a measure of the film quality consistent with the considerations outlined in the ITRS roadmap [www].

II.3.4. X-rays

X-rays are an extremely short wavelength, high energy form of electromagnetic radiation which finds many applications in science and medicine. X-rays are defined as having a wavelength of between 10^{-5} Å to 100 Å. Most applications however, use X-rays of between 0.1 Å to 25 Å. Germanium or the lithium doped silicon (Si(Li)) semiconductor detectors are commonly used to detect the X rays in scattering experiments. Modern energy dispersive instrumentation provides excellent and rapid capability for the qualitative identification of elements in a variety of sample types. The positions and intensities of the spectral peaks provide qualitative and quantitative information. Furthermore, X-ray spectrometry is one of the few techniques, which can be applied directly to solid samples of a wide variety of forms and it is not destructive.

II.3.4.1. XRD used for Bragg diffraction analysis

From the morphological crystallography [Dana] one defines "**A crystal** as the regular polyhedral form, bounded by smooth surfaces, which is assumed by a chemical compound, under the action of its interatomic forces, when passing, under suitable conditions, from the state of a liquid or gas to that of a solid". This definition implicitly means that a crystal is the normal form of all solids and chemical compounds. If we also recall the [Antonoff] definition of the crystal "A crystal is a homogeneous, anisotropic body having the natural shape of a polyhedron", we deduce that the internal properties of a crystal depend on the direction, as is observed experimentally.

A natural consequence of what we have said is that in general a crystal is heterogeneous and anisotropic. When the crystals that compose an isotropic material are randomly oriented, we

say that the material is **polycrystalline**. Its properties are the average of the single crystals properties, which compose the material.

II.3.4.1.1. General theory

The terminology and the theory of Bragg diffraction are illustrated in Appendix C.

II.3.4.1.2. The Scintag Pad V diffractometer

The Division Analytical Facility Scintag Pad V X-ray Powder Diffractometer is a theta-2theta goniometer instrument. It is fitted with a Cu X-ray tube with two beam slits, a four-sample automated sample holder with sample spinning capability, and a low-noise liquid-nitrogen cooled germanium detector with two detector slits. The X-ray tube has a filter wheel allowing one to manually select a single filter. The wheel has filters made of vanadium, manganese, iron, nickel (this is the default filter which is used to remove Cu k-beta radiation), zirconium, or open tube (i.e. no filter).
The goniometer can be scanned in a normal mode (i.e. theta and 2theta are scanned in synchronism), or independent theta and 2theta scans can be performed. Rocking curve scans can be acquired using the independent scanning capability .
The instrument is currently fitted with a set of beam and detector slits that balance the needs of angular resolution and intensity for typical runs.
The instrument is capable of very rapid scans for identification of powders that are simple in composition. Much slower scans are usually required for the analysis of complex mixed phases, thin film samples, high resolution work, cell refinement, or identification of trace impurities. Two scan modes are possible, a continuous scan mode which integrates counts over a small angular range (for rapid scans), and a step-scan mode that is used for slower scans and any precision work.
Data collection and processing is controlled using a standard pc computer which contains a data base of the JCPDS [www2] powder diffraction files. Diffraction spectra are plotted and can be saved as .TXT files and so compared with spectra in the databases.

In a typical diffraction measurement the X-ray tube is positioned at an angle θ with respect to the surface of the sample and the detector is positioned exactly at 2θ. This type of measurement is usually termed "(ω, 2θ) coupled angle".

II.3.4.1.3. An example

We want to analyze $LaAlO_3$ deposited on a Si (100) substrate. We have deposited the $LaAlO_3$ using the tools described in chapter II.1.1. The film was scanned in ω, 2θ using continuous scanning as shown in Figure II.17.

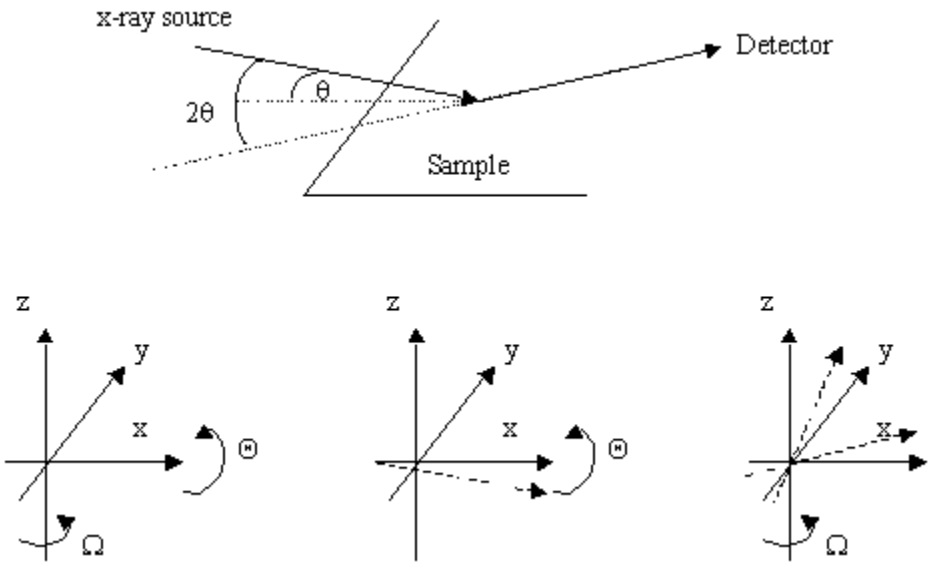

Figure II.17. *Schematic arrangement for a ω, 2θ measurement. The angle ω is actually equal to θ, which is the angle of incidence of the X-ray beam. We also show the axes in which the sample lay, and the possible rotations (Ω and Θ) that the operator can use to analyze the crystallinity of the materials. Ω is the rotation of XY plane around Z axes, and Θ is the rotation of ZX plane around Y axes.*

The reason of the choice of the continued scanning measurement instead of the step scan is because this material has a good XRD sensitivity, so that the signal is well discriminated with respect to that coming from the substrate. In this kind of scanning, particular attention should be taken to align the detector angle and the X-ray source angle as these two angles must be coupled *(goniometer alignment)*. Curve "a" in Figure II.18 is representative of this

XRD measurement. In the region of 30-40° a broad and not very intense peak appears. This peak indicates an amorphous structure and we can conclude that this $LaAlO_3$ sample is in its amorphous state. We also notice that in the region of 60-70° few narrow peaks appear. These are associated with the Si substrate mono-crystalline cubic structure; in particular there is a strong peak at 69.4° which corresponds to the (400) plane reflection. The observation of this peak provides evidence that the sample and the goniometer have been aligned correctly.

The sample was subsequently annealed at 900 °C in order to understand the evolution of the structure following thermal treatment. Usually this treatment induces phase changes in the $LaAlO_3$, so that a polycrystalline structure forms. Curve "b" in Figure II.18 shows new narrow peaks present in the XRD pattern. In order to understand if these peaks are related to $LaAlO_3$ crystal reflections, we need to know the structure of the $LaAlO_3$. $LaAlO_3$ is usually present in a stable rhombohedral crystal geometry tabulated under the perovskite compounds as R3m. We obtained a piece of single crystal of $LaAlO_3$ which was subsequently ground in order to make a powder. This powder was spread onto a Si mono-crystalline (100) substrate and measured. The results are represented in curve c of Figure II.18.

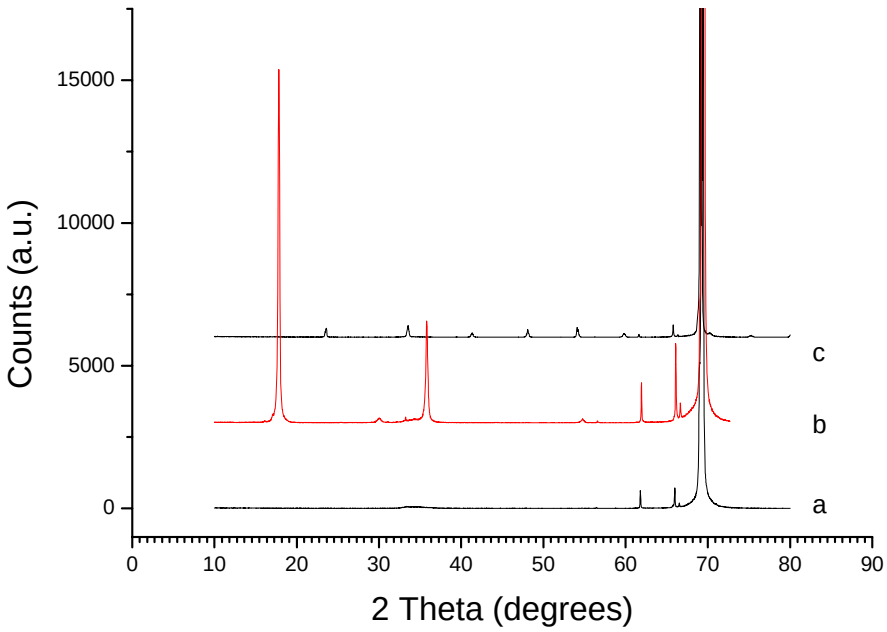

Figure I.18. *XRD patter for a) LaAlO3 deposited on mono-crystalline Si (100), b) $LaAlO_3$ after 900 °C annealing in an O_2 atmosphere and c) powder of single-crystal $LaAlO_3$ spread on Si (100).*

The existence of just a few narrow lines indicates that the sample is crystalline. No broad peak is now present in the region of 30-40° and the Si (400) pattern is still visible, which indicates that the powder is thin enough to let the X-ray beam reach the substrate and also that the peaks in the region of 60-70° are really related to the mono-crystalline Si. Each of the lines in Figure II.18b are assumed to come from the reflections from the rhombahedral planes. First we consider the region of interest in 2θ. In this case we have choose the region between 10 to 60° because the most intense lines are within this range. Obviously the region between 60 to 70° cannot be investigated because of the intense Si pattern. Then we consider all possible planes that can give a reflection. These planes are presented in the table II.5.

Table II.5. *Diffraction parameters in the region of 2θ = 10-60° for a rhombohedral geometry and for the $LaAlO_3$ single crystal powder. The instrument error is estimated to be ±0.05°.*

Rhombohedral planes			Measured $LaAlO_3$ powder	
2θ (°)	(hkl)	d_{hkl} (nm)	2θ (deg.)	d_{hkl} (nm)
23.445	012	0.379	23.6	0.3767
33.386	110	0.268	33.626	0.2663
39.369	021	0.2287		
41.205	202	0.2189	41.442	0.2177
41.289	006	0.2185		
47.972	024	0.1895	47.8	0.1901
52.550	211	0.17402		
54.030	122	0.1695	54.27	0.1689
54.099	116	0.1693	54.27	0.1689
59.670	300	0.1548		
59.701	214	0.1547		
59.798	018	0.1545		

We compare the tabulated 2θ with the 2θ measured. If the angles are close and inside the error of the instrument (±0.05°) we assume that the lines correspond to specific crystallographic planes. In doing this we should also consider:

1. The grain size should be greater then 40 nm
2. The relative intensities of the lines should have a certain value (due to the fact that some planes have a better reflection than other for a certain wavelengths of the X-ray beam
3. We do not consider distortions or displacements of the diffraction lines due to possible strain, stress or distortions of the lattice, from the ideal structure

Thus we can easily use the Bragg equation C.6 in appendix C and determine the lattice plane spacing. Finally using the equation given in Table C.1 in Appendix C we can also calculate the lattice parameters. We obtain a = 0.5326 and c = 1.305 nm which results in a rhombohedral cell volume of 0.321 nm^3. The ideal fundamental cell has a volume of 0.326 nm^3, which is close to our experimental value. This indicates that the $LaAlO_3$ lattice structure is close to the ideal case, and that no distortion in the diffraction peaks is present. We conclude that our $LaAlO_3$ single crystal powder can be used as a good reference for comparison with other samples. Now we return to Figure II.18. We notice that the peaks of curve "b" do not match the lines of curve "c" except for the peak at 54.3° which can, then, be associated with rhombohedral $LaAlO_3$. The others peaks must be due to different compounds like silicides or segregated Al_2O_3 and LaO_2. In fact both 17.98° and 35.91° peaks and their intensities can be associated with the Al_2O_3 tetragonal structure.

The intensity of the peaks and the relative intensities between the various peaks is not random but can help us to understand if a line really belongs to a certain structure. As a general rule the integrated intensity of a reflection (hkl) and not just the amplitude of the peak should be taken. Usually the integrated intensities are recorded on a scale of 100 for the strongest line. The intensities of the lines are more useful when the material under analysis is a mixture of different compounds or when different phases of the same compounds can co-exist. In Figure II.18 there is clear evidence that the lines in the region of 60-70° are associated with the Si (100) cubic planes so an investigation of the (hkl) intensities is not really required for this regime. On the other hand, pattern "b" in Figure II.18 is not well defined. A study of the intensities of the peaks (and not just their position in 2θ) indicates

that some of the crystalline structure belongs to the tetragonal Al_2O_3 confirming the hypothesis advanced above on the basis of angular arguments alone.

The high temperature annealing of deposited, amorphous dielectric films will in general result in crystallization in a polycrystalline form for temperatures < 1000 °C. Growing or annealing materials on top of mono-crystalline substrates can furthermore induce a ***preferential orientation*** in the polycrystalline film so that all orientations of the crystallites are not randomly distributed. XRD is also a powerful technique which may be used to understand the polycrystallinity of the materials. As an example we deposited Ti oxide onto Si(100) with the assistance of a -41 V rf bias and then annealed it at 600 °C for 30 min in N_2. The polycrystallinity of the films was studied by varying the sample orientation (i.e. tilting the plane of the sample surface in a direction at 90 to the incident beam direction) [Cullity]. The results for deposited films of TiO_2 annealed at 600 °C for 30 minutes in N_2 are shown in Figure II.19. We have decided to represent the spectra only in the 24-30° 2θ range, because the two crystalline phases of TiO_2 (rutile and anatase) have their most intense peaks which are associated with their (110) and (101) crystallographic plane in this range. The solid line is the spectrum observed for the sample when it is rotated either 5, 15, 45 or 90° in the xy plane (Ω rotation – Figure II.17). The diffracted peak intensities do not vary with angle within the limits of experimental measurement. The relative intensities of the anatase and rutile lines is equal to 3.35. The dashed line is the result of 5° rotation in the zy plane (Θ rotation Figure II.17). The total intensity changes because of the focusing error [Cullity] which goes to 0° when Θ is > 10°. The ratio of the intensities of the two lines is now equal to 3.1, very close to the value obtained from the Ω rotational experiments. We conclude that the rutile and anatase lines resulted from randomly oriented, polycrystalline TiO_2, i.e. at least for this case there was no preferential orientation.

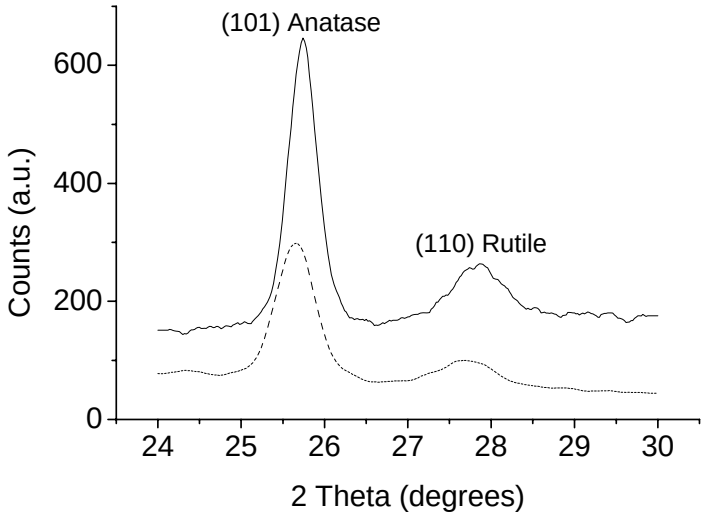

Figure II.19. *Example of the intensity change in films containing anatase and rutile simultaneously, XRD lines due to the rotation of the sample in the Θ direction (dotted curve). When the sample is perfectly parallel to the XY plane the intensity has its maximum. The intensity decreases when the sample is rotated in the direction of Θ but the ratio between the crystalline phases remain the same. This indicates the material is composed of randomly oriented polycrystals.*

This method may, however be used to remove undesired peaks that come from the substrate, such as those in the region of 60-70° due to the intense Si (100) reflection (Figure II.18).

NB: the procedure described in this section usually has been performed almost automatically using the help the Jada software that is provided with the Scintag Pad V diffractometer. The software is also linked to the Jade database, so most of the known compounds and their phases are tabulated.

I.3.4.2. XRD used for reflectivity

This technique is also known as small angle X-ray incidence or glancing incidence X ray scattering

I.3.4.2.1. Theoretical considerations with an example

Reflectivity measurements, usually called X-ray grazing incidence (GIXA), are very useful to obtain information about the density, the roughness and the thickness of thin films. The raw data cannot be used to obtain this information so a fit process is performed. The software we have been using is WinGixa, and the X-ray instrument is a Philips.

In this experiment a collimated X-ray beam is incident on a flat sample surface at almost grazing incidence and one measures the intensity of the scattered beam as a function of the scattered angle. Clearly, for perfect grazing incidence the beam is transmitted and received essentially unscattered (this condition is in fact used to align the collimated source beam and detector. Subsequently, the incident angle and scattered angle are varied minutely and the scattered intensity measured. When the beam penetrates the sample surface completely, the scattered beam intensity drops to zero. An examples of reflectivity patter in given in Figure II.20. The material analyzed was a film of Nd_2O_3 deposited at 280 °C in the CHA evaporator (Figure II.20a) and then annealed ex-situ at 800 °C for 30 min in N_2 atmosphere (Figure II.20b). A small amount of O_2 was introduced in the chamber during deposition in order to assure the stoichiometry of the oxide film. The thickness d_{ox} and the density ρ of the materials can be extrapolated manually with the support of the equations II.17 and II.28.

$$\delta = \frac{\vartheta_c^{\,2}}{2} = 4.1516 * 10^{-6} \frac{\rho}{ME^2} \sum_{j=1}^{N} C_j f_{1j} \qquad \text{II.17}$$

$$d_{ox} = \frac{\lambda}{2\Delta\alpha} \qquad \text{II.18}$$

where δ is associated with the dispersion, θ_c is the critical angle, E is the energy in keV of the X-ray, ρ is the density in g/cm^3, M is the molar weight [g/mol] of a compound of N different atoms, C_j is the number of atoms of type j per molecule, f_{1j} are the atomic scattering factors for atoms of type j, λ is the wavelength (nm) of the X-ray, $\Delta\alpha$ is the angular period of the oscillation and d_{ox} is the thickness of the oxide. $\Delta\alpha$ is shown in Figure II.20a. In this way, we can compare with the thicknesses data obtained using the ellipsometry.

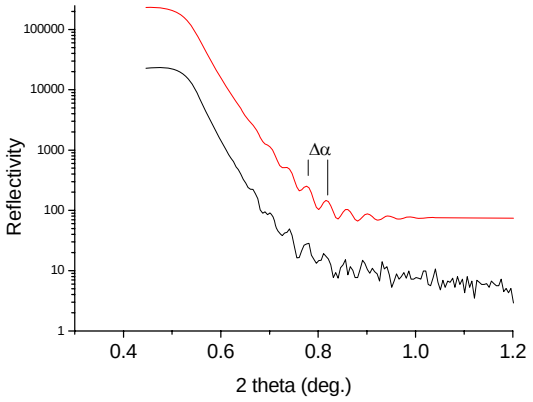

Figure II.20a. *As deposited Nd_2O_3 at 280 °C using the CHA. The red curve is the results of the simulation and the black curve is the raw data.*

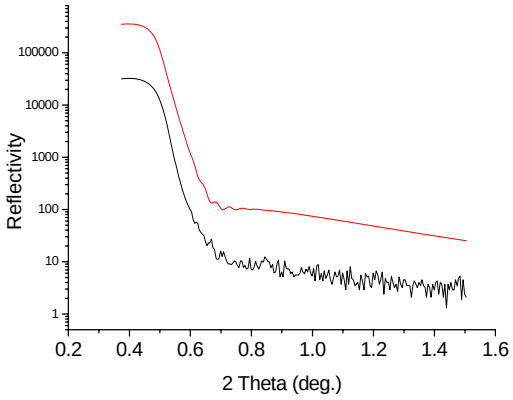

Figure II.20b. *Ddeposited Nd_2O_3 at 280 °C using the CHA and annealed at 800 °C in N_2 atmosphere for 30 minutes. The red curve is the results of the simulation and the black curve is the raw data.*

Finally measuring the angle at which the intensity of the reflectivity is equal to ½ of the maximum value (low angle region) we can also deduce the density. The red lines in Figure II.20 are representative of the fit performed on the raw data (black line). The reason in using a fit software resides in the extra information we can retrieve from the reflectivity [Stoev]. In particular, for our studies, the roughness of the film is essential information. The equation becomes more complicated [Stoev] and it is not discussed further in this thesis. For the as deposited Nd_2O_3 (Figure II.20a), we obtain from the fit a value of ρ of 5.85 g/cm^3, an average roughness of 2.9 nm and a thickness of 92.4 nm. Now we consider Figure II.20b, which refers to annealed Nd_2O_3. One notices that the oscillations have almost disappeared and that the slope of the curve is "less stretched". These 2 effects are respectively due to the increasing roughness and a variation of the density. In fact from the simulated curve (red curve in Figure II.20b) we found that the thickness of the annealed oxide was 81.8 nm, the density and the roughness increased respectively to 7.017 g/cm^3 and to 3.9 nm. This information indicates that important changes have taken place in the oxide during the annealing. These changes will be discussed in the chapter III.

II.3.4.2.2. The Philips MRD high-resolution diffractometer

The X-ray Philips X'Pert MRD diffractometer is a four-circle system with a horizontal, high-resolution Ω-2Θ goniometer (320 mm radius). An open Eulerian cradle provides two additional axes of rotation (-90° < Ψ < 90°, and -360° < Φ < +360°). The X-ray source is a long-fine-focus, ceramic X-ray tube with Cu anode. The diffractometer is equipped with an incident beam monochromator, offering pure K_{α_1} radiation. This allows the crystallographer to perform very accurate diffraction experiments without the need for mathematical $K_{\alpha 2}$ stripping procedures.

Normal operating power is 45 kV, 40 mA (1.8 kW). The sample stage accepts monolithic specimens of a wide variety of shapes and sizes.

In the Grazing-Incidence geometry, the X-ray source is used in line-focus. The incident beam optic is typically a fixed divergence slit assembly. Alternatively, the hybrid monochromator may also be utilized. The detection system consists of a 0.27 radian parallel plate collimator, a graphite monochromator and proportional counter detector. Applications include phase analysis of polycrystalline thin film samples and X-ray reflectivity (XRR).

II.4. CHTM FACILITIES

CHTM is housed in a new (1997), $14M, 60,000 sq. ft. building provided by the State and University of New Mexico with state-of-the-art cleanroom and laboratory facilities for advanced research in microelectronics and related areas. A separate crystal growth facility with integrated safety systems houses MOCVD reactors.

II.4.1. Semiconductor Processing

The Center for High Technology Materials (CHTM) Facility houses a 3500 square foot cleanroom with four bays and associated service chases. Cleanroom temperature and humidity is controlled by a sophisticated digital control network.

- The first bay is designated for photolithography rated at class 100. Housed in this bay are two UV Karl Suss MJB-3 mask aligners, a microscope with a CCD camera and thermal printer, two spinner stations, a develop bench, several ovens for photoresist baking, a metal lift-off station, and two solvent benches. The remaining three bays are rated at class 1000.

- The second bay houses an acid and a base wet bench, an AlphaStep 500 profilometer, two Technics reactive ion etchers with desired gas capabilities, a rapid thermal processor, a rapid thermal annealer, and an oxygen plasma photoresist descummer.
- The third bay is dedicated to a Reactive Ion Beam Etching system, and two electron beam metal evaporators. It also contains an inspection SEM.

The fourth bay has an ellipsometer, a Plasmatherm inductively coupled plasma etcher utilizing chlorine, boron trichloride, silane, hydrogen, argon, and nitrogen process gases. A second tool, a Plasmaquest electron cyclotron resonator plasma processor utilizing argon, silane, hydrogen, nitrogen and oxygen process gases. Thirdly, a Mark 40 CHA evaporator dedicated to dielectric film growth, and lastly, a Samco plasma enhanced chemical vapor deposition system dedicated to silicon nitride film growth.

REFERENCES

[Alonso] M. Alonso and E. J. Finn, "Quantun and Statistical Physic", Addison-Wesley Publishing Company, pag. 36 (1968)

[Antonoff] G. Antonoff, J. Phys. Cjem., **48**, 95 (1944)

[Arnal] Y. Arnal, A. Lacoste and J. Pelletier, Le Vide, **297**, 258 (2000)

[Aspnes] D. E. Aspenes, J. Opt. Soc. Am. **64**, 639 (1974)

[AutoProbe] Park Scientific Instruments, 1171 Borregas Avenue Sunnyvale, California 94089 (USA)

[Berreman] D. W. Berreman, Phys. Rev., **130**, 2193 (1963)

[Bechu] S. Béchu, O. Maulat, Y. Arnal, D. Vempaire, A. Lacoste and J. Pelletier, Surface & Coatings Technol., **186**, 170 (2004)

[CHA] CHA industries, 3565 Haven Avenue, Menlo Park, California 94025 (USA)

[Chandrasekhar] S. Chandrasekhar, A. S. Vengurlekar, S. K. Roy and V. T. Karulkar, J. Appl. Phys., **63**, 2072 (1988)

[Cullity] B. D. Cullity, "Elements of X-ray diffraction" chapter 8, Addison-Wesley Publishing Company (1956)

[Dana] E.S. Dana, "A textbook of mineralogy" 4th edition Wiley, New York, pag. 7 (1962)

[Devine] R. A. B. Devine, J. Non-Cryst. Solids, **152**, 50 (1993)

[Ewald] P. P. Ewald, Z. Crystallogr., **56**, 129 (1921)

[Gaertner] Gaertner Scientific Corporation 1201 Wrightwood Avenue, Chicago, Illinois, 60614 (USA)

[Johnson] F. A. Johnson, Proc. Phys. Soc. (London), **73**, 265 (1959)

[Lacoste] Lacoste, T. Lagarde, S. Bechu, Y. Arnal, J. Pelletier, Plasma Sources Sci. Tech., **11**, 407-412 (2002)

[Lehmann] A. Lehmann, L. Shumann and K. Hübner, Phys. Stat. Sol., **117**, 689 (1983)

[Martinet] C. Martinet and R. A. B. Devine, J. Non-Cryst. Solids, **189**, 96 (1995)

[Mikami] M. Mikami and S. Nakamura, Phys. Rev. B, **66**, 155213 (2002)

[Mozzi] R. L. Mozzi, B. E. Warren, J. Appl. Crystallogr., **2**, 164 (1969)

[MPTC] Modular Process Technology Corp. 2233 Paragon Drive, San Jose, California 95131 (USA)

[Peeters] J. Peeters and Li Li, J. Appl. Phys., **72**, 719 (1992)

[Pelletier] J. Pelletier and T. Lagarde, Thin Solid Thilms, **241**, 240 (1994)

[Pelletier2] J. . Pelletier, T. Lagarde and Y. Arnal, J. Physique IV, **8**, 121 (1998)

[Petit 85] B. Petit, Thesis, Université Joseph Fourier, Grenoble (1985)

[Pichot 88] M. Pichot, A. Durandet, J. Pelletier, Y. Arnal, L. Vallier, Rev. Sci. Instrum., **57**, 1072 (1988)

[Spottiswoode] W. Spottiswoode, "Polarization of light" Macwilliam Co. London, (1874)

[Stoev] K. Stoev and K. Sakurai. The Rigaku Journal, **22**, 14 (1997)

[Sze] S. M. Sze, "Physics of semiconductor devices" J. Wiley & Sons, (1981)

[Tobar] M. E. Tobar, J. Krupka, E. N. N. Ivanov and R. A. Woode, J. Appl. Phys, **83**, 1604 (1998)

[www] http://public.itrs.net

[www2] http://www.icdd.com/

[α-step] Tencor Instrument, 2400 Charleston road, Mountain View, California 94043 (USA)

III RESULTS

RESULTATS

La première partie de ce chapitre est focalisée sur l'étude des alliages $LaAlO_3$ comme possibles candidats pour remplacer l'oxyde de silicium. Les travaux publiés sur le sujet sont nombreux, et les résultats sont divergents. On présente les différents procédés utilisés pour déposer l'oxyde et pour le caractériser. Enfin, on met en relation les propriétés électriques et physiques des oxydes étudiés, tout en essayant de comprendre leur comportement en relation avec les conditions de dépôt.

La deuxième partie est consacrée aux deux oxydes de terres rares Pr_2O_3 et Nd_2O_3. Ces oxydes sont de bons candidats comme des oxydes à forte permittivité. On décrit d'abord comment ils ont été déposés et caractérisés. On procède ensuite à une analyse pour montrer comment les propriétés électriques de ces oxydes sont liées à leur structure cristalline. De cette façon, il est possible de comprendre et de prévoir dans le détail le comportement physique et électrique des oxydes de terres rares.

La troisième partie est dédiée à l'oxyde de titane (TiO_2) et aux pseudo alliages TiO_2-SiO_2. On décrit succinctement les méthodes avec lesquelles ces oxydes ont été déposés et comment ils ont été caractérisés, et on montre l'importance de ces oxydes en microélectronique. On analyse tout d'abord les différentes phases de l'oxyde de titane, puis, en se référant aux travaux antérieurs, on cherche à comprendre les mécanismes physiques déterminant le comportement de tels oxydes et en particulier les problématiques liées au changement de densité par rapport à la variation de concentration de Ti dans les alliages mixtes TiO_2-SiO_2.

III.1. $LaAlO_3$: A HIGH-*k* MATERIAL?

$LaAlO_3$ is considered to be a potential high-k material because of its dielectric constant of ~ 25 [Xiang] and optical band gap of ~ 5 eV and thermal stability up to 2100 °C. A phase transition from cubic to rhombohedral structure occurs at 500 °C and hence, when the $LaAlO_3$ films are cooled down from relatively high deposition or growth temperatures to room temperature, it is very difficult to preserve the ideal cubic structure.

The dielectric constant is mostly isotropic [Samara] so no effects due to the preferential direction in the crystal growth would be expected. There is significant confusion over the value of the dielectric constant of films of this material. $LaAlO_3$ and $LaAlO_xN_y$ amorphous films have been deposited by pulsed laser deposition (laser ablation) [Lu] onto Si substrates and Pt films with Si substrate maintained at 700 °C. In the case of Si substrates, film/substrate interaction was evidenced leading to very low dielectric constants ~ 4.9, in the Pt case, k ~ 25-27 is quoted. Electron beam evaporation methods have also been used [Park] in which the films were deposited onto heated Si substrates (temperatures up to 800 ºC) and values of k ~ 21-25 quoted. This result is surprising since, for the same range of substrate temperatures, [Lu] data shows clear evidence for significant film/substrate interaction under these conditions and the development of an unidentified interfacial layer and correspondingly reduced dielectric constant. Similar conclusions are arrived at from annealing studies presented by [Busani] [Devine]. Furthermore, attempts to reproduce the electron beam evaporated film [Devine] experiments of [Park] [Park1] resulted in low dielectric constant values and evidence in the remnant target material (single crystal $LaAlO_3$) in the form of blackened areas where the electron beam had impacted and given rise to preferential evaporation. Such preferential evaporation is common in almost all binary or mixed oxides since one cannot since there is a tendency for the electron beam to preferentially remove oxygen.

Finally, films deposited by sputtering from stoichiometric $LaAlO_3$ targets [Devine] onto Si substrates at room temperature resulted in dielectric constants in the range 11 – 13. Other sputtering results [Kang] yield a value of k ~ 8.1 although in this case a 750 ºC anneal was performed and, again, this has been demonstrated to result in measurable film/substrate interaction.

In this work we have performed a series of measurements to try to clarify the situation regarding the dielectric constant of amorphous $LaAlO_3$

III.1.1. Structure and physical properties of $LaAlO_3$

Lanthanum-aluminate crystallizes in a perovskite ABO_3 structure. In the ideal case such as $SrTiO_3$ the lattice is cubic, but, depending upon the A and B the fundamental cell can be slightly distorted so that the symmetrical cubic structure is lost. The Goldschmidt tolerance factor t allows determination of the stability of the ABO_3 structures [Goldschmidt]:

$$t = \frac{(r_a - r_o)}{\sqrt{2}(r_b + r_o)} \qquad \text{III.1}$$

where r_a and r_b are the ionic radii. If t=1 the structure is perfectly cubic ($P_{m\bar{3}m}$ space group) , while if $t < 1$ a rhombohedric or orthorhombic distortion appears. The BO_6 octahedra are now not perpendicular with respect to the crystallographic axes and can order themselves periodically (Figure III.1). One of the consequences of this distortion of the cubic cells is a change of the B-O-B bond angle, which is obviously 180° for t = 1 and reduces to 156° for a value of t = 0.75 which is the limit of stability for this system [Ramirez].

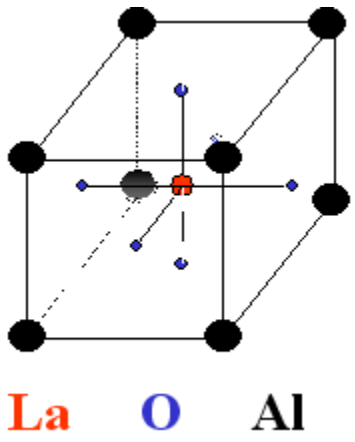

Figure III.1. *$LaAlO_3$ fundamental cell without any distortion of the octahedral AlO_6.*

$LaAlO_3$ with $PrAlO_3$ and $NdAlO_3$ are perovskite structures with a rhombohedral deformation. [Geller] catalogues these perovskites in the $R_{3m} = D^5_{3d}$ group while for [Derighetti] and [Rango] the space group is the $R_{3c} = D^6_{3d}$ with 2 rhombohedral needed to make the fundamental cell. The R_{3c} structure can be obtained from the simple cubic perovskite (P_{m3m}) by rotation of the adjacent AlO_6 octahedra in opposite directions around the $(111)_c$ plane. The AlO_6 octhaedra are non-linearly reproduced but with a constant bond length of the Al-O of 0.190 nm. The length of the La-O bonds for the oxygen atoms of the first coordination sphere is approximately 0.250 nm.

The magnetic, optical and electrical properties of $LaAlO_3$ are strongly dependent on the process used to synthesize the material, which can induce small differences in the rhombohedral distortions. This concerns in particular the first order Raman spectra that is allowed exclusively because lattice distortions since no Raman-active modes are anticipated in the ideal perovskite (P_{3m3}). The 123 cm^{-1} Raman symmetric mode (A_{1g}) involves atomic motion that causes the rhombohedral distortion [Abrashev] and its position in energy can be used to measure the degree of distortion. In the same way, if the rhombohedral distortions are small, the A_{2u}-E_u mode separation in the infrared spectra should be small (compared to LO-TO splitting). These modes are coupled and generate 3 IR-active modes which are visible in the regions of 200, 370 and 700 cm^{-1}.

In the following paragraphs we endeavor to understand the process conditions that influence the optical and electrical properties of $LaAlO_3$/Si system, and how these variables are correlated.

III.1.2. $LaAlO_3$ deposited and grown films

$LaAlO_3$ was grown or deposited on p-type crystalline Si (100) substrates and also Si (111). Significant differences were not observed in using one Si orientation or the other. We therefore report only the conclusions drawn for oxides deposited or grown on Si (100) substrates.

For all samples the Si substrate was initially rinsed in 50:50 HF:H_2O, then blown dry. This is to remove most of the surface contaminants and also the native oxide.

$LaAlO_3$ oxides were deposited or grown using the following procedures:

a) $LaAlO_3$ sputtered on Si(100).

Thin $(La_xAl_{1-x})_2O_3$ films were deposited at room temperature by sputtering from a stoichiometric polycrystalline $LaAlO_3$ target using a 13.56 MHz radio frequency (rf) sputtering source (TORUS 2) with an Ar/O_2 gas mixture. Details of this tool can be found in Chapter II.1.1.2. The main problem with the sputtering process is to insure a sputtering ratio of La/Al close to 1 and La-Al/O close to 0.3 This is for 2 reasons:

- The target should remain stoichiometric for further deposition processes
- To deposit a stoichiometric $LaAlO_3$

In order to do this a simulation was performed using the SRIM software [Srim]. The software allows choice of the target and the plasma gases and it calculates the number of sputtered ions from the target (for each species) for any chosen incident ion energy. In the first approximation we assumed a pure Ar plasma. Table III.1 shows the results of the simulation.

Table III.1. *Sputtering simulation of $LaAlO_3$ single target. The first 5 columns refer to a pure Ar atmosphere sputtering, which means only the Ar ions sputtered the surface of the target. The last two rows are for a mixed Ar and Oxygen atmosphere, respectively with a ratio of Ar/O equal to 75/1 and 75/5.*

Ion Energy (keV)	Number of La sputtered	Number of Al sputtered l	Number of O sputtered	La/Al	La/O	Al/O
0.1	0.0731	0.0638	0.2863	1.1457	0.255	0.222
0.11	0.0798	0.0725	0.32	1.100	0.249	0.226
0.12	0.0807	0.0817	0.3645	0.9877	0.221	0.224
0.13	0.0876	0.0921	0.3645	0.9511	0.224	0.235
0.175	0.0789	0.0793	0.3467	0.9949	0.227	0.228
0.22	0.1315	0.1514	0.6550	0.868	0.20	0.231
0.175	0.1091	0.1185	0.5102	0.92	0.213	0.2322
0.175	0.197	0.202	0.5339	0.975	0.369	0.3783

The ratio of La/Al ions sputtered from the target is close to the unity in the case of 0.17 keV Ar ion energy. We also notice that the ratio between the Al or the La and the oxygen is never

close to the ideal value of 0.33 but it is always smaller. This indicates that more oxygen is sputtered from the $LaAlO_3$ target, which eventually becomes sub-stoichiometric in oxygen. In order to minimize the effects of this problem a small quantity of oxygen was introduced into the chamber with the argon. The two gas line are physically separated and the gases mixed together only inside the ECR reactor chamber. But does the presence of oxygen change the La/Al sputtering ratio? Unfortunately the SRIM software only allowed us to introduce, in the sputtering ion parameters, one type of gas and not a mixture of different gases. To approximately simulate the actual two gas situation we have calculated the sputtering rates for each gas in turn then summed the total effect of both gases using a weighting function equal to the ratio of gas flow actually used experimentally. The results of the simulation for a ratio of Ar/O_2=75/1 and 75/5 is represented in the Table I.1 respectively in the last 2 rows. The optimal ratio between the Ar and the oxygen should be 75/5, ratio so as to ensure stoichiometry of the sputtered O, La and Al ions from the $LaAlO_3$ target.

The introduction of a small amount of oxygen in the chamber is not without consequences. [Xiang] has been previously demonstrated that oxygen can play a role on the deposition rate and the stoichiometry of the sample. Thus different samples were deposited with and without the presence of the oxygen in the argon atmosphere and the different results were compared. A summary of the different experimental conditions is given in the Table III.2.

Table III.2. *Different samples of $LaAlO_{33}$ deposited onto Si wafer using different deposition parameters.*

Distance (cm)	Rf (volt)	Pressure (mTorr)	Gases (sccm)	Voltage and Power	Deposition rate (nm/min)	n_{ox}
15	-	10	Ar=75, O_2=5	175/23	-	-
15	-	5.5	Ar=75, O_2=5	175/23	-	-
15	-	2	Ar=75, O_2=5	175/23	-	-
9	-	5.5	Ar=75, O_2=5	175/23	0.303	1.358
11	-	5.5	Ar=75, O_2=5	118/12	0.17	1.41
11	-	5.5	Ar=75, O_2=5	220/30	0.34	1.625
11	-	5.5	Ar=75, O_2=5	175/23	0.215	1.55

11	-	5.5	Ar=75, O_2=2	175/23	0.299	1.32
11	-	5.5	Ar=75, O_2=0	175/23	0.69	1.758
11	-50	5.5	Ar=75, O_2=5	175/23	0.433	1.783
11	-70	5.5	Ar=75, O_2=5	175/23	0.46	1.780
11	-90	5.5	Ar=75, O_2=5	175/23	0.412	1.802
11	-100	5.5	Ar=75, O_2=5	175/23	0.406	1.801
11	-110	5.5	Ar=75, O_2=5	175/23	-	-

Table II.2 indicates that different parameters should be considered during the deposition. If one of these parameters is not correct we can even result in the situation in which no oxide is deposited. For our oxides the main parameters that we have considered are:

- **Distance** between the target and the Si substrate, where the $LaAlO_3$ is deposited
- **R F**: voltage that is applied on the back face of the substrate
- **Pressure**: is the total pressure of all gases during the deposition
- **Gases**: is the flow rate of gases used, expressed in standard cubic centimetre (Sccm)
- **Voltage and power**: is the voltage applied on the target
- **Deposition rate**: measured in nm/min is the rate at which the oxide deposits on the substrate
- **Refractive index (n_{ox})**: the optical refractive index measured ex situ at 632.8 nm.

The shaded rows refers to sample that has been used for further analysis. The criteria used in our choice were: the homogeneity of the deposited $LaAlO_3$ on Si wafer, the higher refractive index (which indicates that the structure itself may be denser and may be crystalline) and the stoichiometry of the films.

b) $LaAlO_3$ growth on Si(100) after LaAl deposition

To try to circumvent any possibility that the sputtered films were sub-stoichiometric, $LaAlO_3$ films were grown by oxidation of deposited, stoichiometric LaAl alloy. LaAl was deposited by sputtering a stochiometric target of LaAl. The sputtering was performed using the same criteria as desribed above. We were able to oxididize sputtered LaAl films using two techniques:

a) Anodic oxidation of the LaAl. Details of this method were describe by [Peeters] and by [Martinet] and details about our sample can be found in [Busani2].

b) Thermal oxidation of LaAl carried out at 700 °C in pure O_2. Details of the results can also be found in [Busani2]

The main problem that arises with these two oxidatation methods is when the oxygen reaches the interface between the high-k and the silicon substrate, oxidation must be stopped immediately in order to avoid any SiO_2 formation.

In the case of thermal oxidation the oxygen diffusion into Si was controlled by depositing a layer of Si_3N_4 before depositing the LaAl film [Busani2].

In the case of anodic oxidation it turns out that the oxidation of Si is quite difficult [Martinet]. In any event, by controlling the variation of the anodisation voltage we were able to halt the process before the formation of SiO_2. In Figure III.2a we show the variation of the anodisation voltage versus time (i.e. which is essentially a function of the thickness of the oxide film), and in Figure III.2b the corresponding IR spectrum.

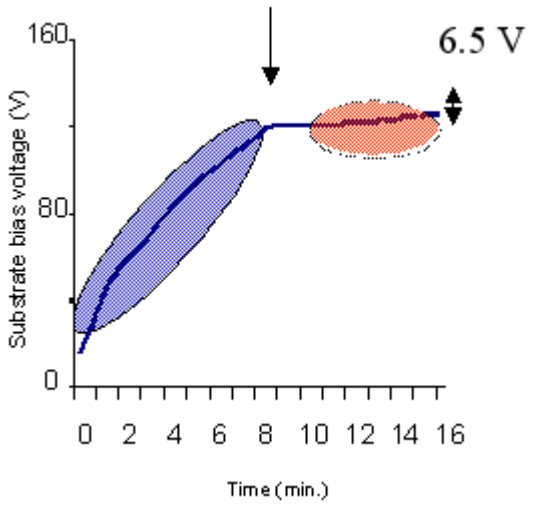

Figure III.2a. *Anodic oxidation of LaAl. The voltage across the oxide increases as the thickness of the growing oxide increases. The blue region refers to LaAl oxidation. The red region refers to Si substrate oxidation after complete oxidation of the top LaAl film.*

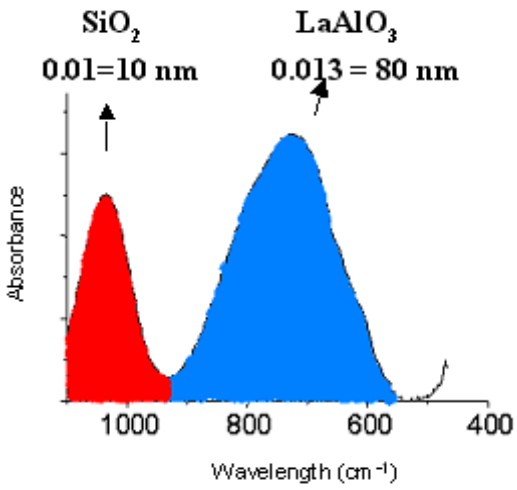

Figure III.2b. *Normal incidente IR spetrum of the anodic $LaAlO_3$ presented in Figure III.2a. The red area centered at 1060 cm^{-1} corresponds to an estimated 10 nm of SiO_2.*

We notice that the formation of the SiO_2 (red area) is associated with a slowly increasing voltage in the red region of Figure III.2a. We also observe that in Figure III.2a between the red and the blue regions there is a transition of about 2 minutes in which the voltage does not appear to increase. To avoid any SiO_2 formation, the anodic oxidation should be stopped in that region.

III.1.3. Thermal annealing

Annealing was carried out in order to increase the density or to re-crystallize the oxide and to remove the oxide trapped charge that can compromise electrical properties. Re-crystallization can improve the dielectric constant (chapter III.1) but can also change the morphology.

To improve re-crystallization, all samples were annealed in the range of 700 to 1000 °C in N_2 atmosphere using both a standard horizontal diffusion furnace and rapid thermal annealing furnace (Chapter II.2). To reduce the charge, annealing at 400 °C in N_2 for 30 min was also carried out. More details are provided in [Busani] and [Busani2].

For temperatures < 700 °C differences respect to as-deposited (amorphous) samples were not observed. For temperatures greater than 700 °C a re-crystallization process begins as well as an interaction with the Si or Si_3N_4 + Si substrate. The presence of the Si_3N_4, however serves to limit the interaction between Si and $LaAlO_3$. This behavior has been observed in all samples and it is the cause of increasing the surface roughness has shown in the AFM pictures presented in Figure III.3. The average roughness before the annealing treatment was less than 1 nm (Figure III.2a), after thermal treatment it increases to 18 nm (Figure III.2b) and [Busani]. For the same annealing conditions, the roughness was less important in the thermal grown sample, due to the Si_3N_4 passivation layer.

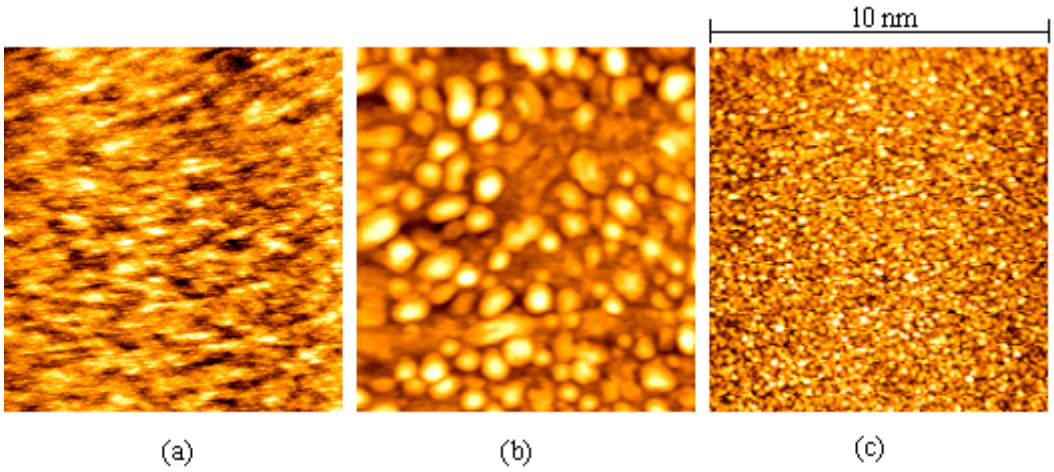

Figure III.3. *AFM images of (a) ununnealed sputtered $LaAlO_3$ (b) LaAl deposited on Si and annealed at 400 °C for 30 min in N_2 atmosphere (c) typical $LaAlO_3$ after flash annealing at 900 °C for 1 min in N_2 atmosphere.*

The annealing of the $Si/Si_3N_4/LaAlO_3$ structure needs a further discussion. In this case the annealing temperature was brought to 850 °C for 6 hours in an N_2 atmosphere. The reason of such a long annealing is because [Taspinar] has found that this is the time in order to form a crystalline rhombohedral (or pseudo cubic) $LaAlO_3$. In this case a slight interaction between the Si_3N_4 and $LaAlO_3$ was noticed. Increasing the annealing temperature resulted in a Si substrate-$LaAlO_3$ interaction. Again, for all annealing temperatures above 700 °C the roughness of $LaAlO_3$ film also becomes important.

From the annealing and oxidation studies we can make the following observations:

- As deposited sputtered $LaAlO_3$, anodic $LaAlO_3$ and thermal oxidized $LaAlO_3$ are amorphous
- Annealing over 700 °C always induces re-crystallization of the $LaAlO_3$ as well as provoking interaction among Si Al, O and La. Consequently the oxide becomes extremely rough.
- A Si_3N_4 layer between the Si substrate and LaAlO3 reduces the interaction between the oxide and the Si substrate.

NB: In Figure III.3c we show the surface of the LaAl deposited onto Si substrate and then annealed at 400 °C for 30 min ion N_2 Atmosphere. This sample result, after the XRD analysis, to be crystalline and actually the roughness of the surface (Figure III.3c) is

important. Futhermore we have oxidized in O_2 atmosphere at 800 °C the crystalline LaAl and we have found that the $LaAlO_3$ is amorphous. No interaction has been noted because we did not oxidize the entire LaAl. This is an important result. Indeed one expects that from a crystalline metal a crystalline oxide is formed. This is not true for Si and SiO_2 and it is not true for LaAl and $LaAlO_3$.

III.1.4. Characterization

In order to understand the electrical and physical properties of our $LaAlO_3$ we have characterized our oxides using different techniques already presented in chapter II. These characterizations should help us to understand the discrepancies among the various published values of k as discussed in chapter III.1.

a) AFM

The AFM was used to analyze the surface of the oxide sample. In Figure III.3 we show some results. As a general rule, all samples that received a thermal treatment over 700 °C present a very significant roughness. It is also notable that if one removes the annealed oxide, the Si substrate is also very rough. This is an indication that Si reacts with the oxide and not just that the oxide is re-crystallized.

b) Infrared absorption

The IR absorbance spectra were measured for all samples in order to determine the degree of crystallinity of the oxides, any possible formation of SiO_2 at the Si/oxide interface (chapter II and chapter III.1.2) and possible La-Si bond formation [Ono]. The common IR active modes have been presented in the literature [Saine] [Abrashev] [Busani]. In agreement with the published data, our deposited and grown samples show a broad absorbance band centered at 778 cm^{-1}. In Figure III.4a we show a typical IR spectrum of an amorphous $LaAlO_3$ film deposited on a Si substrate, before (black line) and after annealing at 800 °C for 1 min in N_2 atmosphere (red line). The amorphous structure presents a broad peak centered at 758 cm^{-1}. The annealed sample shows different narrow bands; each band is representative of vibration in a different structure as indicated in Figure III.4a. The vibration centered at 650 cm^{-1} can be associated with a pseudo-cubic structure of $LaAlO_3$. This peak has been

identified in the literature as the asymmetrical stretching of La with 2 nearest neighbor oxygens in the AlO_6 octahedra (Figure III.1) that form the $LaAlO_3$ cell. In Figure III.4b we show the IR spectra of the amorphous $LaAlO_3$ sample used to produce Figure III.4a subsequently annealed at 750 °C for 1 min in N_2 atmosphere.

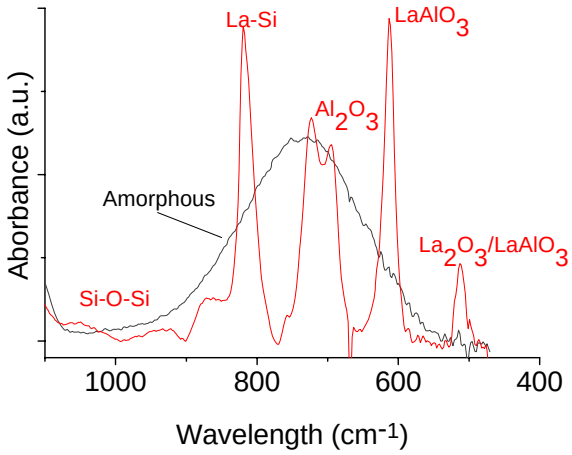

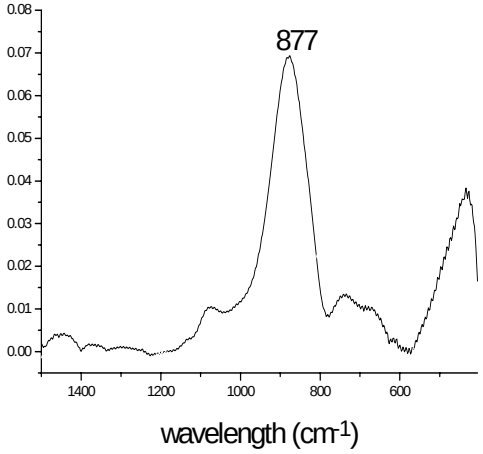

Figure III.4a. *Typical normal incidence IR spectra for amorphous LaAlO3 (black line) and annealed (red line) at 800 °C for 1 min in N_2 atmosphere.*

Figure III.4b. *Typical normal incidence IR spectra for $LaAlO_3$ annealed at 750 °C for 1 min in N_2.*

The peak at ~ 1100 cm^{-1} is due to the baseline subtraction problem (chapter II.3.2.3), the peak at 877 cm^{-1}, which is characteristic of the Si-La interaction, and the double peak in the region of 620-730 cm^{-1}. This is actually the same vibrational mode of O-La-O in the AlO_6 octahedra but split into LO and TO modes. The IR absorbance measurements were performed in normal incidence, so no LO mode is expected.

The reason of the presence of a LO mode in normal incidence has been investigated using some SiO_2 samples.

ba) Surface roughness and LO IR peak

A crude estimate of the roughness of the surface can be obtained using the LO absorbance. Basically when a normal incident beam is absorbed by a polished surface, only the TO vibrations are excited as outlined above. When the same beam is absorbed by a surface that has a finite roughness, the surface is not flat anymore, and so the beam can no longer be

considered to be perfectly normally incident (Figure III.5a) in certain areas of the surface. To demonstrate this effect we produced a regular pattern of grooves on a Si(100) substrate which was then oxidized so that a uniformly rough surface of SiO_2 was created. Figure III.5b shows the AFM image of 30 nm of SiO_2 grown on the patterned Si surface. The angle between the normal to the surface and the pattern was 55° corrsponding to the (111) direction of the crystallografic plane of the Si. This angle is produced by anisotropic etching used to make the pattern.

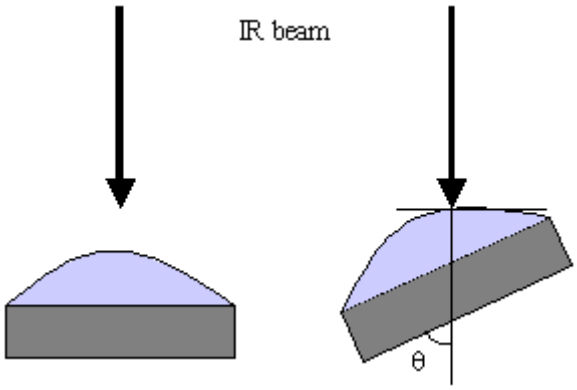

Figure III.54a. *Simple schema of an normal incident IR beam in a non-flat SiO_2 surface.*

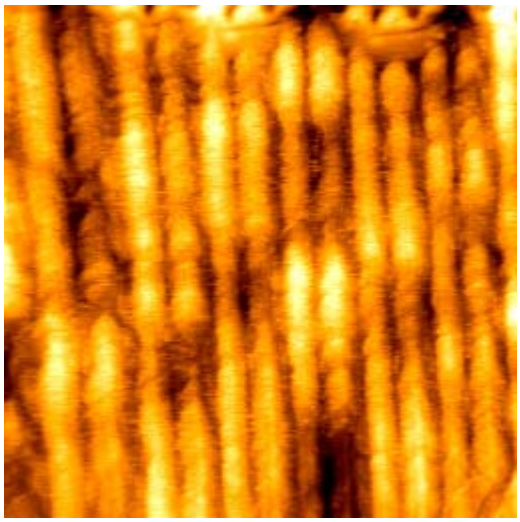

Figure III.5b. *AFM image of a regular SiO_2 patter grown on Si (100). The angle of each pattern is approximately 55°-75°.*

This effect of non-normal imcidence is evident in the IR spectra inn Figure III.6 where 3 different cases are represented. The spectra have beeen normalized to the same thickness so that it is easy to compare the relative amplitudes of the peaks. The black line refers to a normal incidence absorbance for SiO_2, the red line is the normal incidence for the SiO_2 with the regular pattern described above and the blue one is the oblique incidence (20°) for a polished SiO_2. The sample that has a regular pattern, produces a peak at 1258 cm^{-1} which is close to the LO value of 1255 cm^{-1}. The sample measured in oblique incidence of 20° also shows the same intense LO peak.

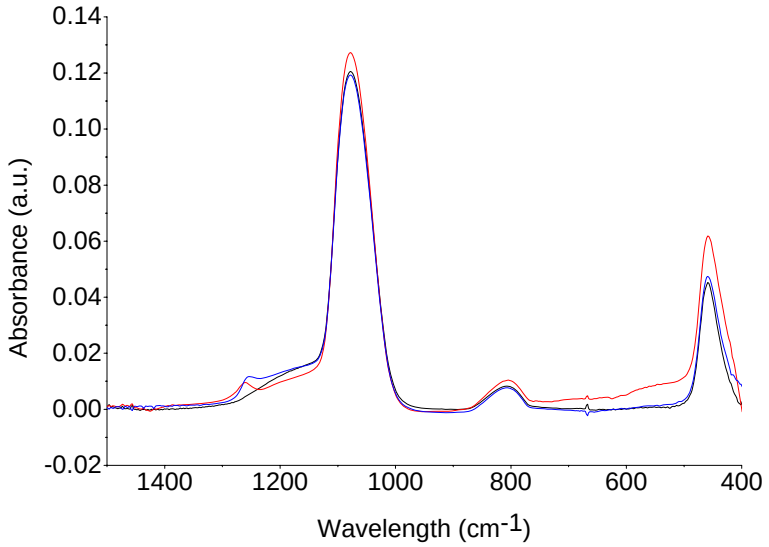

Figure III.6. *IR absorbance spectra for different SiO_2 samples. Black line: normal incidence absorbance for SiO_2. Red line: normal incidence for patterned SiO_2. Blue line: 20° oblique incidence on a regular, flat SiO_2.*

c) XRD and grazing incidence X-ray reflectivity

The XRD measurements were performed only on those samples which showed a form of crystallinity in the IR spectra. Some patterns were also obtained for the as deposited and as grown $LaAlO_3$ to confirm the results of the IR spectra. We already discussed the XRD properties of the $LaAlO_3$ in chapter II.3.4.1.3. Here we underline that the same conclusion obtained by IR absorbance analysis is retrieved.

The glazing incidence X-ray reflectivity was measured to study the surface roughness, the density of the oxide films and to confirm the oxide thickness. The raw data were fitted with the WINGIXA software provided by PANalytical Company. The results confirm that the thermal treatment increases the roughness overall. The density data are summarized in Table III.3

d) XPS and EDS

The composition of some oxides were analyzed in order to be sure about the stoichiometry of deposited and grown oxides. These results have been discussed by [Busani] and show that amorphous $LaAlO_3$ has a correct stoichiometry. The XPS profile measurements also indicate that the amorphous oxides are homogeneous through all their thickness. The annealed

samples, however, show the presence of Si in the oxide layer. This indicates that the Si interacts with the oxide upon thermal treatment and also that Si diffuses significantly into the oxide layer.

EDX measurements were used to study ex situ the LaAl composition. The instrument was calibrated with a single crystal $LaAlO_3$ and a polycrystalline sample of LaAl. The results are shown in Table III.3

e) Ellipsometry

Ellipsometry measurements were performed on all samples. The evolution of the refractive index was followed in order to see if changes occurred before and after annealing. Results are shown in Table III.2 and Table III.3. For the annealed sample (over 700 °C) and the thermally grown $LaAlO_3$ the roughness of the films resulted in exaggerated diffusion of light from the sample surface such that measurements were meaningless. For those samples we do not obtain any reasonable data. The higher index value for the anodic oxides corresponds to that of samples that do not show any evidence of an interfacial SiO_2 layer. These values should be compared to that of the single crystal that we also measured. Unfortunately we did not find values of n for amorphous $LaAlO_3$ published in the literature.

f) *Electrical measurements*

In order to test the electrical quality of the interface and the oxide C(V) and I(V) measurements were performed. The k values obtained by measurements of the oxide capacitance in accumulation are represented in the Table III.3. For the annealed samples, the roughness was clearly a limit for these measurements, the C(V) curve shapes were extremely deformed and unusable. So a Metal-Oxide/Insulator-degenerated-semiconductor capacitor was built in order to measure the value of the absolute dielectric constant of the oxide. For the annealed samples we were unable to make sensible measurements because of the annealing induced destruction of the oxide stochiometry and morphology.. A further note should be made about thermal oxides. These oxides are rough but there is not interaction between Si and $LaAlO_3$ because of the low temperature oxidation process and Si_3N_4 passivation layer. However their morphology with the encapsulated nitride layer generates problems in understanding the exact value of k. So we have extrapolated the value of k considering also the thin layer of Si_3N_4.

Hysteresis was very important for all sputtered samples. The flat band voltage moved from –10 V to –1.5 V after applying a bias electric field of +(-) 1 MV/cm for a period of 1-10 minutes then sweeping the voltage from positive (negative) to negative (positive). C(V) curves were very distorted after annealing in an inert atmosphere at 400 °C. This indicates that sputtering develops damage at the Si/oxide interface that can enhance the Si oxide interaction during annealing processes [Busani]. The anodized $LaAlO_3$ shows a smaller hysteresis (0.74 V), which indicates the presence of a mobile positive charge [Busani2].

Table III.3. *Main parameters derived or measured for different $LaAlO_3$ oxide films. IR and XRD Crystalline (C) or Amorphous (A) indications are given. The high thickness of single crystal did not allowed absorbance measurements. .The ratio of La/Al and La/O are given. In this case both XPS and EDS measurements were performed. The error was estimated to be ~5%. The dielectric constant k and the refractive index n are given for that sample we were able to measure. The k value for the single crystal was taken by general literature. The densities ρ was measured within ± 0.3g/cm³ error.*

Type of $LaAlO_3$	IR	XRD	La/Al La/O	n	*k*	ρ
As-deposited sputtered	A	A	0.98-0.3	1.75-1.801	13-15	4.20
Annelead sputtered	A+C	A+C	Irregular	-	-	
Anodic	A	A	0.95-0.33	1.75-1.92	8.7-13	4.4
Annelead Anodic	A+C	A+C	Irregular	-	-	
Thermal grown	A	A	0.95-0.38	-	22	
Single Crystal (bulk)	-	C	1-0.33	2.01	28	6.51

Finally the I(V) measurements at ± 1 MV/cm show very low leakage currents of the order of 10^{-7}-10^{-8} A/cm^2.

III.1.5. Relation between k, n and ρ[1]

One of the data sets shown in Table III.3 is the dielectric constant k of different $LaAlO_3$. In the first instance, we notice that the value of k for crystalline $LaAlO_3$ is much higher than for amorphous $LaAlO_3$. We also notice that as k decreases n and ρ decrease as well. It is evident

[1] The formula and the physical constants and units are expressed in CGS system. We did not use the SI system because the equations that we will discuss usually are known in CGS.

that a relation should exist between these parameters. In order to understand the reason that lead to such significant differences in the dielectric constant of the same material, it is necessary to understand the physical background of these constants.

The equations of Clausious-Mossotti and Lorentz-Lorenz relate the dielectric constant k, the density ρ (i.e. the inverse of the molar volume V_m), the refractive index n and the polarizibilities α of a material [Bunget]:

$$\frac{k-1}{k+2} = \frac{4\pi}{3}\frac{1}{V_m}\left(\alpha_{vib} + \alpha_{elec}\right) \qquad \text{III.1}$$

$$\frac{n^2-1}{n^2+2} = \frac{4\pi}{3}\frac{1}{V_m}\left(\alpha_{elec}\right) \qquad \text{III.2}$$

The vibrational polarizability α_{vib} involves the variation of the bond distance between two atoms, or a variation of the bond force. The atoms move with respect to the central positions due to internal effects. The electronic polarizability (α_{elec}) the electronic charge around the nuclei and it is therefore, to first order, independent of the matrix in which the atoms/ions find themselves. The vibrational polarizability α_{vib} is the polarizability term which reflects the bonding between the atoms/ions in the network. Generally if an external electric field E is oscillating at a very high frequency the vibrational component of the polarizability cannot respond and only the electronic term is sensed. From Equations III.1 and III.2 one concludes that in this limit $k = n^2$. In this case one also defines $k = k_\infty$ where the symbol ∞ indicates that the dielectric constant is measured for an infinite frequency of the electromagnetic wave. The electronic term is consequently relevant for optical properties (for example, the refractive index) because the vibrational part cannot follow the associated high frequency fields. This can be written:

$$\alpha_{elec.} = \frac{2\sum\left[\left\langle 0\middle|e\sum x_i\middle|j\right\rangle\left\langle j\middle|e\sum x_i\middle|0\right\rangle\right]}{\sum\left(Wi - Wo\right)} \qquad \text{III.3}$$

where W_i is the energy of the i state and the sums run over all electrons (defined by i) and all states defined by j. To a first approximation the vibrational part of the polarizability, α_{vib} for a diatomic chain can be written:

$$\alpha_{vib.} = \frac{e^2}{\left(\mu_c \omega_0^{\ 2}\right)} \qquad \text{III.4}$$

where μ_c is the reduced mass and ω_o is a characteristic vibrational frequency of the chain. In Eq. III.4 the denominator is essentially the insulator band gap and this should decrease with the vibrational frequency. Indeed the density or the "atomic packing" may have an influence on the polarizability through $\omega_{o,}$ because ω_o is a proportional to V_m: one can understand that the phonon frequency is lowered when the inter-atomic distance increases ("weaker bonds"). This would lead to a decrease in polarizability with decreasing density. From Eq. III.4 the vibrational part of the polarizability should also decrease when the density decreases so that both polarizability contributions are expected to decrease as the network density decreases.
In Eq. III.1 and III.2 we also notice that a variation of the molecular volume influences the dielectric constant and the refractive index. We remember that from V_m we can also calculate the density of the material. In fact as V_m increases, the density ρ decreases so does the dielectric constant. Among the typical reasons that contribute to variations of the molecular volume we remember

- The coordination increases (or decreases) the number of atoms per unit cells so that the structure is more dense (lower molecular volume). In simple terms a 4 fold coordinate cell is more "open" than a 6 fold coordinate. This has been clearly demonstrated in calculations for $Zr_xSi_{1-x}O_2$ ternary oxides [Kurtz]. Experimentally one can appeal to the example of SiO_2 polymorphs where for the four fold coordinated, amorphous phase the density is typically 2.21 g cm^{-3} whilst for the 6 fold coordinated stishovite phase, the density increases to 4 – 4.4 g cm^{-3}.
- The atoms can be closer to each other
- Porosity

In Figure III.7 we shows the dependence of n and k on α/V_m

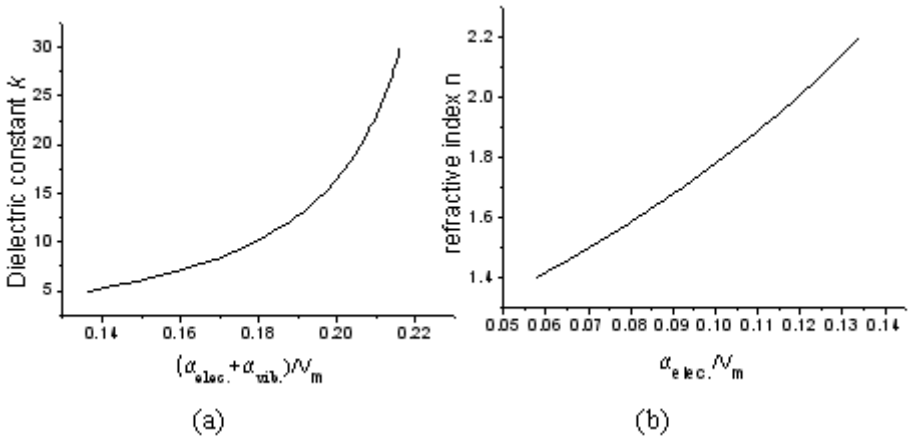

Figure III.7. *Variation of n and k calculated from equations III.1 and III.3.*

It is interesting and relevant to notice how, for a material that has a high dielectric constant or a high refractive index a small variation of α or V_m can have a dramatic effect on k and n. Furthermore it is significant to understand the role of the polarizabilities in the material to understand the behavior of the dielectric constant.

III.1.6. Discussion

Using Table III.3 we obtain $((n^2-1)/(n^2+2))/((k-1)/(k+2))= 0.56$ for the single crystal and for sputtered amorphous $LaAlO_3$ and anodic $LaAlO_3$, 0.52-0.59. These values are quite close and, considering the experimental errors, we can conclude that the same ratio is found for the crystal and for the amorphous. This implies that for this material the polarizability does not change significantly with molar volume.

We analyzed now the porosity of the oxide film. As we already said in the chapter III.1.5 this can influence the density of the material, so that a misinterpretation of the results can lead to a misunderstanding of the role that the molar volume plays. We note first that the refractive index of the film is directly related to its density Eq. II.2 and that for our deposited samples with and without substrate bias, the refractive indices are close. It is generally assumed that one of the roles of substrate bias is to ion-assist the deposition of the film and that this usually leads to a more densified form. Since there is little difference in our case this may support the hypothesis that our films are already densified i.e. not porous. Secondly, we have

performed measurements on anodized LaAl. Not only are the refractive indices obtained very close to the sputtered $LaAlO_3$ values but so are the dielectric constants and the density. It is known from anodization experiments [Martinet] on Si that anodic oxides are not usually porous and that they may even be denser, sometimes, than their thermal counterparts. It is therefore a reasonable assumption that the sputtered $LaAlO_3$ and anodized LaAl films are not porous. Therefore the experimental data are consistent with the equations III.1 and III.2 in the sense that $LaAlO_3$ is expected to be less dense and to have a lower refractive index in the amorphous phase.

We now discuss the influence of the polarizibilities on the structure. Usually the polarizibilities can be calculated with the additivity model [Shannon]: the dielectric constant of a complex oxide can be expressed as a sum of the contributions from the individual molecules through the weighted sum of their polarizibilities (Eq. III.5)

$$(\alpha_{vib} + \alpha_{elec.})M_A M_Q O_{(B+P)} = c(\alpha_{vib} + \alpha_{elec.})M_A O_B + (1-c)(\alpha_{vib} + \alpha_{elec.})M_Q O_P \qquad \text{III.5}$$

where c is the effective concentration of M_AO_B molecules and (1-c) the concentration of M_QO_P molecules. It is a tacit assumption of the additivity model that as the concentration is changed, the only variable is the molecular volume of the composite molecule $M_AM_QO_{B+P}$.

The polarizibilities can be determined using the equations III.1 and III.2 once the dielectric constant and the refractive index are known. The molecular volume can be obtained using the X-ray reflectivity data, while the bulk values are taken from the literature. To our knowledge there are no density data for amorphous $LaAlO_3$ available in the literature. The results from our experiments are shown in Table III.4 [Busani2]. If the value of k or n cannot be measured, it is possible to use the value of α_{elec} from [Grimes]. However, it must be noted that [Busani3] has demonstrated for different materials that the experimental data and the published [Grimes] data for α_{elec} differ consistently by a factor of 2.

Table III.4. *Polarizibilities in $LaAlO_3$ oxides. For simplicity k of 13 was used for amorphous $LaAlO_3$*

Structure	α_{elec} [Å^3]	(α_{elec} + α_{vib}) [Å^3]	α_{vib} [Å^3]	V_m [Å^3]
Crystal	(6.53-6.88)	11.61	(5.1-4.73)	54.45
Amorph.	(8.3-8.8) ±0.6	16.14±1.1	7.59±2.0	84.5 ± 6

From Table III.4 we notice how the molecular volume is consistently lower in the crystalline phase than in the amorphous samples. Magic angle spinning nuclear magnetic resonance measurements [Iuga] on amorphous and crystallized, bulk $LaAlO_3$ show clear evidence for the fact that in the amorphous phase, the Al atoms are fourfold coordinated with oxygens. In the crystalline phase, the coordination increases to 6. Also the polarizibilities, α_{elec} and $(\alpha_{elec}+ \alpha_{vib.})$, as expected, are smaller in the crystalline phase than in the amorphous phase. Therefore both electronic and vibrational polarizibilities terms decrease as the molecular volume decreases (Figure 5 [Busani2]). The variation of the polarizability with molecular volume has been the subject of various publications [Piper] [Busani2]. It also been shown that the same dependence exits between temperature dependence measurements of polarizibilities and molecular volume.

It is clear, therefore, that one should not neglect possible variations in the electronic and/or vibrational components of the overall polarizibilities as a function of the molecular volume. Thus invariance of $(\alpha_{el} + \alpha_{vib})$ with change in molecular volume cannot be assumed as the additivity rule assumes.

In conclusion, the analysis of the data obtained from amorphous and crystalline $LaAlO_3$ shows clearly that density, which can be expressed in terms of molecular volume and polarizibilities, prevents the increasing of the dielectric constant for $LaAlO_3$ amorphous oxides. The knowledge of both refractive index and dielectric constant are indispensable to understand the behavior of the material and more they can help to predict that behavior. The thermodynamic instability of $LaAlO_3$ with Si, finally forces to use low temperature processing, which results in the formation of an amorphous oxide. Thus the dielectric constant of 28 seems not to be achievable.

It is still not understandable how people could have found a dielectric constant higher than 20 for amorphous $LaAlO_3$ deposited onto Si substrate. Some of these works has deposited $LaAlO_3$ with different techniques but always using a substrate temperature higher than 700 °C [Park] [Park1] [Sukuzi]. In these cases the stability of the $LaAlO_3$ for post annealing processes over 850 °C ws not studied, but most likely, has we have demonstrated, the La may react with Si, deteriorating the Si/oxide interfacial properties.

III.2. RARE EARTH OXIDES: Pr_2O_3 AND Nd_2O_3

Generally, there are two groups of possible candidates for epitaxial growth on silicon: perovskite-type structures and binary metal oxides. In paragraph III.1 we have studied an example of a ternary RE (Rare Earth) oxide with a promising dielectric constant. We also have demonstrated that interaction and density problems limit the application of such alloys. Generally, studies over the past years have shown that RE based oxides usually reacts with Si forming a silicide [Ono] or just a thin SiO_2 layer due to the segregation of the oxide into the metal and oxygen. These effects have a negative impact on the overall dielectric constant of the gate capacitor. The most reliable data about the electrical properties appears to be that on the crystalline RE_2O_3 films grown on Si since here it is most likely that an amorphous SiO_2 interfacial barrier is not formed. Other problems such as anisotropy in the dielectric constant in the crystalline phase and hygroscopy have been reported. Furthermore not much if we take the case of two specific examples, Pr_2O_3 and Nd_2O_3 not much information is available on their amorphous oxides.

The reason why these oxides are so popular is the reasonable band gap (4-6 eV [Rozhkov]) and the high dielectric constant (in the crystalline state) and very low leakage currents. For example [Osten] reported that in the case of Pr_2O_3 leakage current densities were 10^{-8} A/cm^2 at 1 MV/cm which is 10^4 lower than the observed value for HfO_2 and ZrO_2 films having the same EOT of 1.4 nm [Lee][Qi]. Furthermore Pr_2O_3 has a valence and conduction band offset with respect to Si (100) which is of the order of 1 eV.

As a general rule the RE oxides, based on elements with atomic number $Z > 62$, form in a cubic crystalline phase with a dielectric constant which may range from 12.5 to 14.3 [Busani3]. It has been demonstrated that for the oxides based on the RE elements with an atomic number $Z< 62$, the so called "light" rare-earths, two crystalline phases can be obtained (cubic and hexagonal) and in consequence two different values of dielectric constant are anticipated. However the hexagonal phase occurs at temperatures < 1000 °C, so that this is the most common phase for microelectronics applicatiosn. A good example for a RE oxide with $Z < 62$ is Pr_2O_3 while for $Z > 62$ it is Gd_2O_3. Gd_2O_3 has a typical stable cubic phase and its dielectric constant is ≤ 14 [Busani3]. Pr_2O_3 in its cubic phase also has a dielectric constant of 15 [Jeon], which increases to 23-25 in the hexagonal phase (as observed for polycrystalline samples [Busani3][Lo Nigro2]. That Pr_2O_3 has a higher dielectric

constant than Gd_2O_3 is not, in fact, surprising since it has been demonstrated [Busani3] that the molecular volume for the hexagonal phase is smaller than for the cubic phase leading directly to a larger molar permittivity.

It is interesting, therefore, to analyze the RE oxides and see what correlation exists between the dielectric constant and the phase transition, to clarify the published data and to understand the importance of the network structure.

III.2.1. Structure and physical properties of Pr_2O_3 and Nd_2O_3

The RE_2O_3 system shows polymorphism with the change of R^{3+} ionic radii with temperature [Yokogawa]. They are known to belong to one or more of hexagonal, monoclinic and cubic forms. In the hexagonal form usually the metal atoms are 7 fold coordinated, in the monoclinic form they are 6 or 7 fold coordinated and in the cubic form are 6 fold coordinated. There are also two other forms depending on the atomic radii and there is another hexagonal phase that occurs at high temperature. This differs from the other hexagonal form by a shift in the position of the diffraction lines in the XRD spectra. The cubic structure is usually obtained at 600 °C [Dulepov], while increasing the temperature up to 900 °C results in the hexagonal phase [Brauer]

Praseodymium oxides may have different P/O compositions and form either stoichiometric compounds of PrO_2 and Pr_2O_3 or non stoichiometric phases [Eyring]. The PrO_2 phase has the CaF_2 structure while Pr_2O_3 has the sesquioxide structure of manganese oxide (Mn_2O_3) or a structural hexagonal phase (a= 0.3851 nm and c= 0.612 nm) related to lanthanum oxide.

Neodymium oxide is very similar to Pr_2O_3. It presents the same cubic or hexagonal phase. Usually for thin films the hexagonal phase is stabilized at 750 °C [Lo Nigro]

III.2.2. CHA Pr_2O_3 and Nd_2O_3 deposition

Praseodymium oxides and Neodymium oxides were deposited onto Si (100) substrates using the CHA evaporator described in the chapter III.1.2

For all samples the 4“ Si substrates were prior rinsed in 50:50 HF:H_2O, then blown dry. This is to remove most of the surface contaminants and also the native oxide. During deposition

a typical pressure in the chamber was ~ 10^{-7} torr, and during deposition O_2 gas was introduced in the chamber so that the pressure was controlled at 2.5 x 10^{-5} torr.
For all samples the uniformity of the film was typically of 4".

a) Pr_2O_3

Commercially available powder of Pr_6O_{11} was used as a source for electron beam evaporation. It is known that the CHA evaporation causes the formation of the sub-stoichiometric oxide because of excessive O loss and this is why the starting material was not stoichiometric Pr_2O_3. The samples were deposited with the Si substrate temperature close to room temperature. The deposition rate was 0.05 nm/s in order to not cause excessive evaporation of the Pr_6O_{11} powder when the electron bean hits it. Particular attention has been taken to avoid this problem
Typically the total thickness of the oxide deposited film was 110 nm.

b) Nd_2O_3

Single crystal Nd_2O_3 was used for electron beam evaporation. Three sets of sample were deposited: one at room temperature with a deposition rate of 0.2 nm/s, one at 280 °C with a deposition rate of 0.2 nm/s and one at 280 °C with a deposition rate of 0.4 nm/s. The variation of the deposition rate and the temperature was studied in order to be able to crystallize or densify the deposited oxides prior post annealing processes. This will be discussed later. Typically the thickness of the oxide film was 88 nm.

III.2.3. Thermal annealing

a) Pr_2O_3

Annealing of Pr_2O_3 deposited films was performed in a temperature range of 200-500 °C in an O_2 atmosphere for different annealing times. Oxygen was used in order to re-oxidize the oxide in the event of sub-stoichiometry. We observed that the samples annealed at 400 °C and 500 °C do not show any structural, optical or electrical differences. So in this thesis we report only the results for the samples annealed at 400 °C for 50 minutes.

b) Nd_2O_3

The three different types of samples were also annealed in the range of temperature of 400-600 °C in an O_2 atmosphere and then at 800 °C for 30 minutes in an N_2 atmosphere. It appeared that annealing at 600 °C for 3 hours in an O_2 atmosphere saturated the optical indices so that only this annealing temperature was considered for further studies. The N_2 gas, for high temperature annealing, was used to minimize possible oxidation of the Si at the dielectric /Si interface while the lower temperature O_2 anneal was used to ensure re-oxidation the Nd_2O_3 if by chance it was sub-stoichiometric in the as-deposited state.
Further annealing at 900 °C showed interaction between the Si and the Nd, as we will demonstrate in the IR section of chapter III.2.4.

III.2.4. Characterization

a) XRD

XRD was a powerful tool in the characterization of Nd_2O_3 and Pr_2O_3 because these oxides were found to be a mixture of different phases depending upon different experimental conditions (Table III.5).

aa) Pr_2O_3

The as-deposited room temperature Pr_2O_3 showed no sharps peaks consistent with the films being amorphous. Further annealing at 400 °C in O_2 for 50 min induced a few narrow peaks indicating that hexagonal crystalline Pr_2O_3 is formed (Figure 1 of [Busani3]).

ab) Nd_2O_3

The sample deposited at room temperature does not show any XRD line, which is an indication of its amorphous structure. Once annealed at 600 °C for 3 hours, the structure of cubic polycrystalline Nd_2O_3 appears in the XRD pattern (Figure 4 of [Busani7])). Lines at 34.45° (411) and at 41.77° (431) are quite imperceptible and can be easily mistaken with the noise. If we do not consider these 2 lines, the XRD pattern can be misinterpreted since cubic NdO_2 presents a similar pattern compared to the Nd_2O_3, just slightly shifted of 0.4° towards lower 2 theta. Such a small shift could easily have resulted in our case because of poor alignment of the instruments.

We now consider the samples that were deposited at 280 °C with a deposition rate of 0.2 nm/sec. From Figure III.8a we observe that as-deposited samples at 280 °C (black curve in Figure III.8a) show a cubic structure. It also seems that a small peak (h(002)) due to hexagonal phase of Nd_2O_3 appears. Further annealing at 600 °C in O_2 followed by annealing at 800 °C in N_2 for 30 minutes (red line in Figure III.8a) removed the hexagonal components and resulted in a pure cubic Nd_2O_3 phase, similar to the one described for the room temperature sample annealed at 600 °C for 3 hours.

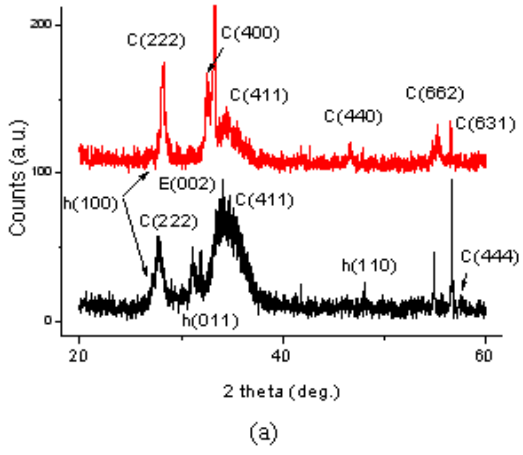

Figure III.8a. *X ray diffraction pattern for Nd_2O_3 deposited at 280 ºC at 0.2 nm /s (black curve) followed by 600 ºC annealing for 3 h in O_2 and then at 800 ºC for 30 min in N_2 (red curve). The hexagonal and cubic phase diffraction lines are indicated with an "h" or a "c" [Busani7].*

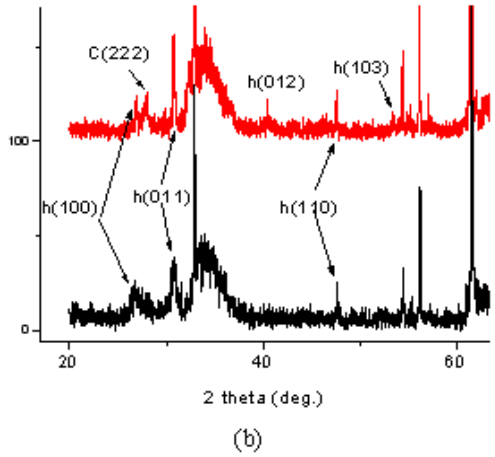

Figure III.8b. *X ray diffraction pattern for Nd_2O_3 deposited on Si(100) at 280 ºC at 0.04 nm /s (black curve) followed by 600 ºC annealing for 3 h in O_2 and then at 800 ºC for 30 min in N_2 (red curve). The hexagonal and cubic phase diffraction lines are indicated with an "h" or a "c" [Busani7].*

These results are interesting. It has been reported that nano-powders of Nd_2O_3 are cubic at 600 °C but transform to hexagonal in the 850 – 1000 °C range [Dong] suggesting that high temperature treatment should lead to formation of the hexagonal phase.

Finally we consider the sample that was deposited at 280 °C at 0.04 nm/s (Figure III.8b). The as-deposited Nd_2O_3 (red curve in Figure III.8b) presents a strong hexagonal line (h(011)) which becomes more intense followed by annealing at 600 °C in O_2 for 3 hours and then at 800 °C for 30 min in N_2. The hexagonal phase was not present in the other samples,

suggesting that the combination of deposition temperature and deposition rate plays an important role.

b) Ellipsometry

All Nd_2O_3 and Pr_2O_3 samples were characterized with the ellipsometry to determine the refractive index and the thicknesses of the samples. The refractive index values were indispensable to understand the evolution of the oxide structure as a function of different deposition conditions and post annealing processes. Typically the error in the refractive index is ± 0.005.

ba) Pr_2O_3

The refractive index of as deposited room temperature films was typically 1.80 and after annealing at 400 °C for 50 minutes it rose to 2.025. The increase of the refractive index usually followed a decrease of the oxide film thickness of the order of 20%.

We also noticed that the Pr_6O_{11} powder melted under e-beam evaporation and that the Pr_6O_{11} became sub-stoichiometric. The refractive index of the Pr_2O_3 deposited with a "new" Pr_6O_{11} powder source was observed to be 1.85. This value decreases to 1.80 after a few depositions, and this is a clear indication of the change in the Pr_2O_3 oxygen stochiometry resulting from a change in the source stoichiometry. This conclusion justifies the annealing in O_2 atmosphere and the introduction of a small quantity of O_2 during the deposition process. In literature stoichiometric electron beam Pr_2O_3 evaporated using a Pr_6O_{11} source has been reported [Osten2] without the use O_2 gas.

bb) Nd_2O_3

The measured refractive index of the as-deposited material at room temperature was 1.76. Following annealing at 600 °C the refractive index increased to 1.93 ± 0.02. Finally, after annealing at 800 °C in N_2, the refractive index stabilized at 1.92 ± 0.02.

The measured refractive for as deposited samples at 280 °C with a deposition rate of 0.2 nm/s was 1.80-1.82, it remained similar after annealing at 600 °C. This value is significantly lower than the value of 1.93 observed for similarly annealed films which were initially deposited at room temperature. Following a further anneal at 800 °C the refractive index

stabilized at 1.84, again lower than the value for the annealed, initially amorphous films. The overall behavior of the density and the refractive index strongly points to the conclusion that deposition at 0.2 nm/s combined with the temperature effect (280 °C substrate temperature) results in less dense films, perhaps columnar or porous, than we obtain if the initial films are deposited at room temperature

The measured refractive index for as-deposited films at 280 °C with a deposition rate of 0.04 nm/s shows clear evidence for the hexagonal phase with a refractive index of 1.83. The refractive index of hexagonal Nd_2O_3 is expected to be ~ 2.11 suggesting that the film is indeed composed of amorphous and hexagonal material. Upon annealing at 600 °C in oxygen followed by 800 °C in N_2, the refractive index increases to 1.91-1.94, still lower than 2.11.

NB: Assuming a heterogeneous mixture with an amorphous material of index 1.76, we estimate the film would be composed of 80% amorphous phase and 20% hexagonal. Note, however, that the amorphous values were determined for room temperature deposited films whilst the films discussed here were deposited at 280 °C.

c) FTIR

Fourier transform infrared absorption (FTIR) spectra, in the absorbance mode using normal incidence or oblique incidence, was measured in the range of 400-1500 cm^{-1}. The primary peak for Pr_2O_3 and Nd_2O_3 was lower then 400 cm^{-1} and therefore not accessible for our instrument. However, as demonstrated in the chapter II.3.2.3, FTIR can be used to semi-quantitatively estimate the amount of interfacial SiO_2 (if present) by observation of the transverse optic asymmetric stretch mode appearing at ~ 1070 cm^{-1} (depending upon film thickness) or the longitudinal optical mode at ~ 1260 cm^{-1}. This measurement was carried out for the three types of samples and no evidence was found for any significant SiO_2 layer at the dielectric/Si interface. We quantify this to mean that any such interlayer was less than 1 nm thick.

FTIR was also used to discern a possible RE-Si interaction. We present in the Figure III.9 the IR spectra for Nd_2O_3 deposited at 280 °C (a) and then annealed at 900 °C for 15 minutes in N_2 atmosphere (b).

The two spectra differ by a broad peak located at ~ 900 cm^{-1}. This absorbance region has been discussed in the IR section of the chapter III.1.4 and is attributable to RE-Si bonds [Ono].

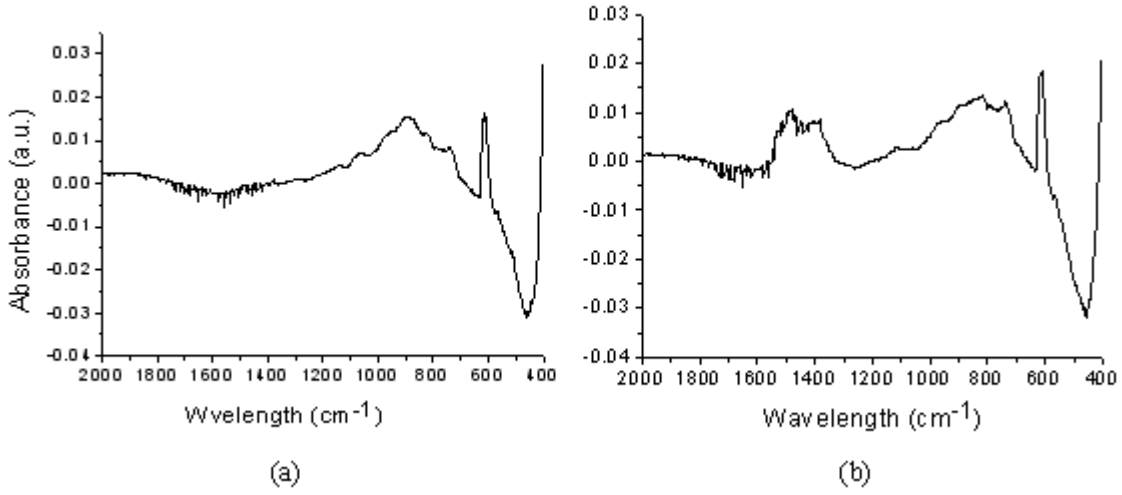

Figure III.9. *Nd_2O_3 normal incidence absorbance IR spectra. (a) deposited at 280 °C and (b) annealed at 900 °C for 15 min.*

d) Grazing incidence X-ray reflectivity

The density of Pr_2O_3 as deposited and annealed were respectively 6.42 and 7.08 g/cm^3 as shown in Figure 2 of [Busani3]. The roughness was in the range of 1.2-1.4 nm for both annealed and unannealed sample.

The results of reflectivity measurements for Nd_2O_3 samples are given in Figure 1, Figure 2 and Figure 3 of [Busani7] and in Table III.5. Here we just make the following observations:

- Amorphous Nd_2O_3 has a density value of 6.42 g/cm^3
- Sample deposited at room temperature and then annealed at 600° C had density value from our fitting of 6.7 g/cm^3, which is consistent with but slightly larger than the cubic phase value quoted in the [JADE] database of 6.57 g/cm^3, and lower than the value of 6.97 g cm^{-3} reported for bulk c-NdO_2. This indirect measurement gives further credence to the assumption that the 600 °C annealed sample was indeed polycrystalline, cubic Nd_2O_3.
- Samples deposited at 280 °C at 0.2 nm/s were a mixture of amorphous, hexagonal and cubic phase, so that the density data cannot be interpreted. Following annealing at 600 °C in oxygen, density was ascertained to be 6.5 g/cm^3 which is slightly lower

than the value of 6.7 g/cm^3 value determined for the annealed, amorphous material (i.e. cubic Nd_2O_3).

- Samples deposited at 280 °C at 0.04 nm/s and then annealed at 600 °C in O_2 for 3 hours then at 800 °C in N_2 for 30 min showed a density of 7.02 g/cm^3 which is slightly smaller than the bulk value (7.14 g/cm^3)
- The roughness of all samples was in the range of 1.2-1.5 nm, which confirms the relatively low roughness found for Pr_2O_3 samples.

e) Electrical measurements

Metal oxide semiconductor (MOS) capacitors were manufactured by depositing 0.00196 cm^2 Al dots on the oxide film surface. Details can be found in Table III.5.

For the Nd_2O_3 sample deposited at room temperature, which appears amorphous from the X-Ray diffraction patterns, we measured a dielectric constant (current density) in the range 11-12 (10^{-7} A/cm^2 at 1 MV/cm) whereas for the samples that were mainly composed of c-Nd_2O_3 we obtained 13-15 (10^{-4} A cm^{-2} at 1 MV/cm). The samples, which were a mixture of c-Nd2O3 and h-Nd2O3, gave a dielectric constant in the range of 17-18 and a current density of 10^{-4} A/cm^2. The value for the amorphous samples is slightly smaller than a previously reported amorphous value (12.9 [Jeon]) and this suggests that our films may be less dense than those obtained by others. More details can be found in [Busani7]

The dielectric constant of as deposited Pr_2O_3 samples at room temperature was 15-17. A high level of hysteresis was also found in the C(V) curves. The annealed samples were very rough and a metal-insulator-metal structure was made to determine the dielectric constant that was 24.7-25.1.

From the characterization we conclude the following:

- The deposition temperature and rate has a significant effect on the structure of the as-deposited films and on their behavior as a function of annealing temperature.
- Pr_2O_3 and Nd_2O_3 were deposited in amorphous and in a crystalline phase.

- The different crystalline phases were obtained with no interaction between the Si substrate and the RE oxide.

Table III.5. *Summary of the most important physical parameters measured or calculated for Pr_2O_3 and Nd_2O_3. The thickness of the oxide (d_{ox}) is measured with an error of ± 0.5 nm, the flat band voltage with a typical error of ± 0.2 V, the density ρ with an error of ± 0.2 g/cm³. The column called "Phase" refers to Amorphous (Am), Cubic (C) and hexagonal (H) phases of RE-oxide. The table is divided into 4 sections, which correspond with the different colors. Each color refers to the same as-deposited sample that received a different annealing process.*

Sample name	d_{ox} (nm)	n	*k*	ρ (g/cm³)	Phase	Rough (nm)	V_{FB} (V)
Pr_2O_3	113	1.80	15-17.04 [a]	6.42	Am	< 1.4	-
Pr_2O_3 ann 400 °C	85	2.025	24 -26.1 [a]	7.08	H	< 1.4	-
Nd_2O_3	97.8	1.76	11-12.7[a]	6.4	Am	< 1.4	-
Nd_2O_3 ann. at 600 °C O_2 6 h.	75.7	1.92	13.6-15.4	6.7	C	< 1.4	- 2.3
Nd_2O_3 280 °C at 0.2 nm/s	86.8	1.80	-	-	Am+H+C	< 1.4	
Nd_2O_3 ann. 600 °C in O_2 for 6 h	85.9	1.827	13-15 [a]	6.55	C	< 1.4	
Nd_2O_3 ann. 600 °C in O_2 for 6 h then 800 °C N_2	87	1.842	13-15.4 [a]	6.57	C	< 1.4	
Nd_2O_3 280 °C at 0.04 nm/s	99.5	1.83	11-11.7 [a]	-	Am+H	< 1.4	
Nd_2O_3 ann. 600 °C in O_2 for 6 h then 800 °C in N_2	88.0	1.91-1.94	17.7-18.7	7.02	Not pure H	< 1.4	- 1.5

a = from metal-oxide-metal structure

III.2.5. Discussion[2]

We remember that typically the heavy RE oxides crystallize in the cubic phase, whilst the light RE oxides crystallize in the hexagonal structure [Lanthanide] [www].

We also observe that the dielectric constants of light crystalline RE's are significantly larger than in the heavier crystalline RE oxides (Table I of [Busani3]). Furthermore we notice from Table III.5 that Pr_2O_3 has a larger dielectric constant as compared with Nd_2O_3 and that the k of Nd_2O_3 increases until the hexagonal phase is reached. Pr are Nd have close atomic number so that the behavior of the dielectric constant may at first seem unpredictable and inconsistent. In this section we try to understand these inconsistencies.

We start by considering the variation of the molecular volume for different RE oxides. In Table I of reference [Busani3] are shown some values found in the literature for the dielectric constant and the molecular volume of the crystalline RE oxides. We have plotted in Figure III.10a the molecular volume as a function of the RE ion. It is evident that for those RE oxides that are typically hexagonal a smaller molecular volume is found compared with the heavier RE cubic oxides.

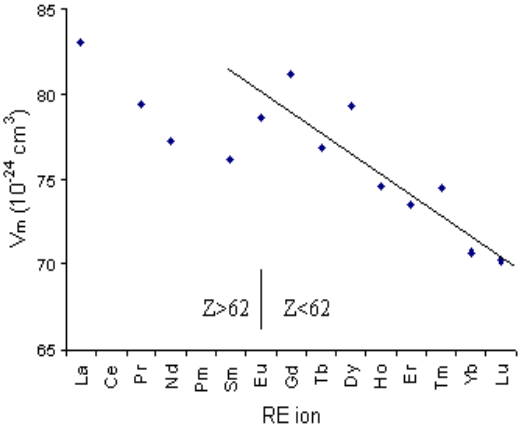

Figure III.10a. *Molecular volume as a function of the RE ion in the series* RE_2O_3.

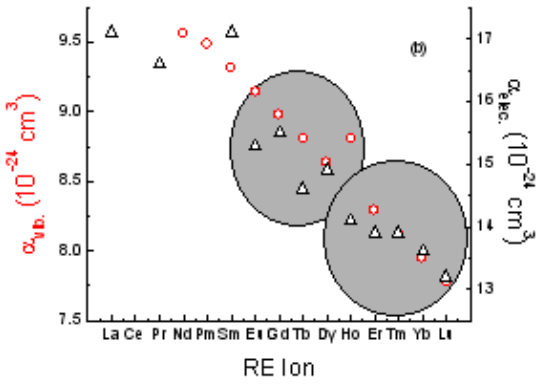

Figure III.10b. *Variation of* $\alpha_{vib.}$ *for crystalline* RE_2O_3 *compounds (O) and* $(\alpha_{elec} + \alpha_{vib})$ *calculated from Eq. III.1 and using measured dielectric constants [Busani3]* (Δ).

[2] The additity rule described in Eq. III.5 will not be used, since it is specifically for mixed oxides.

We also notice that in the transition region a step of a possible monotonic behavior is found which corresponds to phase change of the RE oxide from hexagonal to cubic. As evidenced in equation III.1, if one does not change the molecular polarizability ($\alpha_{elec} + \alpha_{vib}$) an increase of k is expected with reduced molecular volume.

Therefore we investigate the molecular polarizibilities of these oxides. Unfortunately we did not find direct measurements of the polarizibilities in the literature, so that using the k values presented in the Table I of the reference [Busani3] and introducing them into Eq. III.1 we have calculated the value of ($\alpha_{elec} + \alpha_{vib}$). In this case we accept that the polarizability is a function of the dielectric constant and the molecular volume as well. It is interesting that a linear behavior is observed without any non-monotonic step in the transition region (Figure 4a [Busani3]). This is also true if one consider the series of $RE_3Ga_5O_{12}$ [Shannon]. So we can conclude that the step in the dielectric constant results primarily from a change in the volume of the RE_2O_3 network due to the phase change.

We calculate now the single components of the polarizability. The monotonic decrease of ($\alpha_{elec} + \alpha_{vib}$) can be expressed by the Eq. III.6

$$\left(\frac{3V_m}{4\pi}\right)\left(\frac{k-1}{k+2}\right) = \left(\alpha_{vib} + \alpha_{elec}\right) = 2\alpha_{RE^{3+}} + 3\alpha_{O^{2-}} + F_0^{-1}\left(Z - Z'\right)^2 \qquad \text{III.6}$$

where the term $F_0^{-1}\left(Z - Z'\right)^2$ is defined by [Sangster] and it is related to the relative displacement of the RE and O ions in the network. So we can assume an additive model for the vibrational component of the polarizability (α_{vib}) and calculate it using the Eq. III.7

$$\left(\frac{3V_m}{4\pi}\right)\left(\frac{n^2-1}{n^2+2}\right) = \left(\alpha_{vib}\right) = 2\alpha_{RE^{3+}} + 3\alpha_{O^{2-}} \qquad \text{III.7}$$

($\alpha_{elec} + \alpha_{vib}$) and of α_{vib} have been calculated by [Busani3] and we show the values in Figure III.10b. As evidenced by the grey circles, the vibrational polarizability and the molecular polarizability follow the same linear law in the region of heavy RE ions. Then when we approach to the transition region there is a reduction of the polarizability. Comparing the

Eq. III.6 and Eq. III.7 this reduction in the transition region suggest that some variation in the term related to the relative displacement may also be occurring.

Now we consider the Pr_2O_3 that we have deposited. The as deposited samples are amorphous and using the values from Table III.5 for an average *k* of 16 we obtain V_m = 85.6x10^{-24} cm^3 $\alpha_{elec.}$ = 17x10^{-24} cm^3. We compare these values to the hexagonal $V_{m\ hexa}$ = 78.1x10^{-24} cm^3 and to the hexagonal polarizability $\alpha_{elec\ hexa}$ = 16.6x10^{-24} cm^3. These values fit perfectly on Figure III.10 and so the large Pr_2O_3 dielectric constant is indeed expected. Furthermore the differences in the molecular volume between amorphous and crystalline Pr_2O_3 lead us to conclude that the primary driver in varying the dielectric constant is the density of the network through its atomic structure.

The Nd_2O_3 cubic phase is completely known, and in fact the molecular volume ($V_{m\ cubic}$ = 83.4x10^{-24} cm^3) and the polarizibilities ($\alpha_{elec\ cubic}$ = 16.4x10^{-24} cm^3) fit in Figures III.10a and III.10b. However it is not possible to measure the real value of the dielectric constant of the hexagonal phase because, as shown in Table III.5, we never formed pure hexagonal Nd_2O_3 film. However with the help of the cubic refractive index and dielectric constant k values, using ellipsometry data in order to determine the relative concentration of the hexagonal phase in the oxide, [Busani7] has determined that the dielectric constant for the hexagonal Nd_2O_3 is in the range of 21-27. The value of 27 was determined under the approximation that (α_{elec} + α_{vib}) is not molecular volume dependent. This range of values is approximately consistent with the values of 20–27 reported for hexagonal La_2O_3 and 25–25.4 reported for hexagonal Pr_2O_3

In conclusion we can confirm that the behavior of the experimentally observed dielectric constants across the crystalline RE_2O_3 series can be entirely determined in terms of the structure of the oxide network and the variation of the ionic contribution ($2\alpha_{RE^{3+}} + 3\alpha_{O^{2-}}$).

III.3. TiO_2 AND SiO_2-TiO_2 SYSTEMS

In Chapter II we analyzed the different problems that one should take into consideration in the quest for new microelectronics materials. As anticipated in the celebrated "semiconductor roadmap", a dielectric with k ≥ 25 must be found to enable the technologies

of the year 2016 or even earlier. As mentioned previously, permittivity is not the only criterion for the dielectric. Amongst the numerous requirements we recall that the dielectric should preferably be amorphous to eliminate electrical leakage along grain boundaries, its optical bandgap should be large and it should be thermodynamically stable with respect to Si. Finally the dielectric/Si substrate interface should have interface state densities comparable to those of the Si/SiO_2 interface. Many binary oxides have been studied but it seems so far that none match all the requirements, in particular because almost everything reacts with Si upon post deposition thermal treatment.

In the short term industry appears to have adopted [Triyoso] a "patch" involving the use of $Hf_xSi_yO_2$ or $Hf_xSi_yO_pN_q$ which has a dielectric constant ~ 12. The basic premise appears to be that a silicate based material will have a low interactivity with the Si substrate and an acceptable electronic band gap. Furthermore, it may remain amorphous to high temperatures where dopant activation anneals are typically carried out. In any event, it is understood that the criteria for 2014 generation devices will not be met even with this insulator. Another long term alternative is required. One dielectric which appeared to satisfy most of the requirements is HfO_2 although, whilst the dielectric constant of the crystalline phase is ~ 25 [Kukly], the amorphous state has a value ~ 15 [Okada]. Furthermore, interaction with the Si substrate has been evidenced [Puthenkovilakam] as well as a rather low recrystallization temperature 450 °C [He].

In order to satisfy some of the requisite conditions outlined one might logically start from the basis of dissolving a strongly polarizable molecule in SiO_2 and profit from the stability of the SiO_2/Si interface as was the case of Hf in SiO_2. The low frequency molecular polarizability of HfO_2 is ~ 7.1 x 10^{-24} cm^3 which is much larger than that of SiO_2 (~ 4.9 x 10^{-24} cm^3). Since one obtains a k ~ 12 for diluted Hf in SiO_2, one clearly needs to look for a much more polarizable ion.

From tabulated polarizability values, TiO_2 which has a value ~ 15.6 x 10^{-24} cm^3 might be a solution, so that mixing SiO_2 and TiO_2 could be the right choice. Although the electronic bandgap in TiO_2 is relatively small (~ 3.5 eV) [Wallace], the dielectric constant of the crystalline rutile phase is ~ 114 [Tang] in the amorphous phase it drops to ~31-33 [Busani4] [Scarel] which is still substantially larger than for amorphous HfO_2. One must ask if alloying TiO_2 and SiO_2 will cause the relatively high amorphous dielectric constant to reduce too drastically (e.g. $Hf_xSi_yO_2$) and thereby render this mixed dielectric also unusable. This would

be true if one assumes that the dielectric constant varies linearly with the concentration of the SiO_2. In the case of ZrO_2 which has a crystalline phase constant ~ 26, the dielectric constant for the stoichiometric compound $ZrSiO_2$ is quoted as [Lucovsky] 12 indicating that the variation between pure SiO_2 and the stoichiometric compound must be supra-linear [Lucovsky] [Neumayer]. For the compound $Zr_{0.15}Si_{0.85}O_2$, the dielectric constant is 11 whilst the linearly extrapolated value for this concentration should have been ~ 6. The origin of this enhancement has been much discussed but it turns out that the most probable cause is the network structure [Kurtz]. Initial arguments suggested that Zr simply replaced Si in the SiO_2 network and that the O coordination around the Zr was 4. However, detailed X ray absorption fine structure measurements [Mountjoy2] provide evidence that in dilute mixtures of ZrO_2 and SiO_2, the coordination of the Zr ion is > 7. Figure III of the reference [Busani5] shows the change in the molecular volume as a function of the Zr coordination.

HfO_2-TiO_2 systems has also been investigated by [Honda]. The results report linear behavior of the dielectric constant for concentration of TiO_2 < 50 %. These results, combined with the ZrO_2-SiO_2 and Ta_2O_5-SiO_2 data indicate that the behavior of the dielectric constant of a mixed oxide system depends upon different variables, and cannot be simply anticipated.

For the TiO_2-SiO_2 system [Henderson] has studied the coordination of Ti in the mixed oxide, for low Ti concentration. He has found that for Ti % < of 3.9 % the Ti is 4 fold coordinated, whilst for Ti % > 3.9 Ti it is 5 fold coordinated. Unfortunately their SiO_2-TiO_2 samples were prepared using the sol-gel method and the role of the OH- bonds, in developing the coordination, was not investigated [Henderson]. It is known that, for example, H and OH can play an important role in modifying the coordination [Houssa]

The dielectric constant of TiO_2 mixed SiO_2 alloys has not been investigated in the literature. A few studies have been performed on the refractive index [Wang] but typically mixtures of high % of TiO_2 seem not to have been considered. Thus mixing TiO_2 with SiO_2 would be interesting in order to if network coordination could be engineered to induce supralinear behavior of the dielectric constant as for the $Zr_{0.15}Si_{0.85}O_2$ case.

We have therefore studied the electrical and physical properties of TiO_2 and the mixed oxides, $Ti_xSi_yO_2$.

III.3.1. The TiO_2 structure

TiO_2 presents 3 possible crystalline phases: rutile, anatase and brookite. Rutile's basic structural unit is a TiO_6 octahedron, which is slightly distorted so that it forms a chain of edge sharing octahedra with its neighbors. Rutile with the highest density is the most desired phase in term of transparency and index value, but it also has the highest birefringence, with n_0=2.9 and n_e=2.6. The birefringence is reflected in the dielectric constant, which make this material electrically and optically anisotropic. The rutile dielectric constant, in fact, is defined by $\varepsilon_{\parallel} = 90$ and $\varepsilon_{\perp} = 180$ [Tobar], so that from Eq. III.8

$$\varepsilon = (\varepsilon_{\perp} + 2\varepsilon_{\parallel})/3 \qquad \text{III.8}$$

we obtain an average dielectric constant of 120.

Anatase, in the same way, is formed of TiO_6 octahedra but it is less birefringent and typically has a refractive index of 2.3-2.5. Both phases are tetragonal with lattice constants, a and c, of 0.4594 nm and 0.2958 nm for rutile [Cromer] and 0.3785 nm and 0.9514 nm for anatase [Baur], they differ in coordination. Anatase is only 8 fold coordinated whilst rutile is 10 fold coordinated. The fundamental cell has tetragonal geometry as shown Figure III.11. Compared to rutile, there is a significant degree of buckling associated with O-Ti-O bonds in anatase. The buckling reduces the crystal symmetry and results in larger unit cells dimensions in the (001) direction. Each of these TiO_6 is more distorted than in the case of rutile, such that four O-Ti-O angles deviate form 90°.

Finally brookite, an instable rhombohedral structure, is rarely observed in thin films.

Although all 3 phases are possible at room temperature, they transform in rutile phases for temperature higher than 800 °C [Gonzalez].

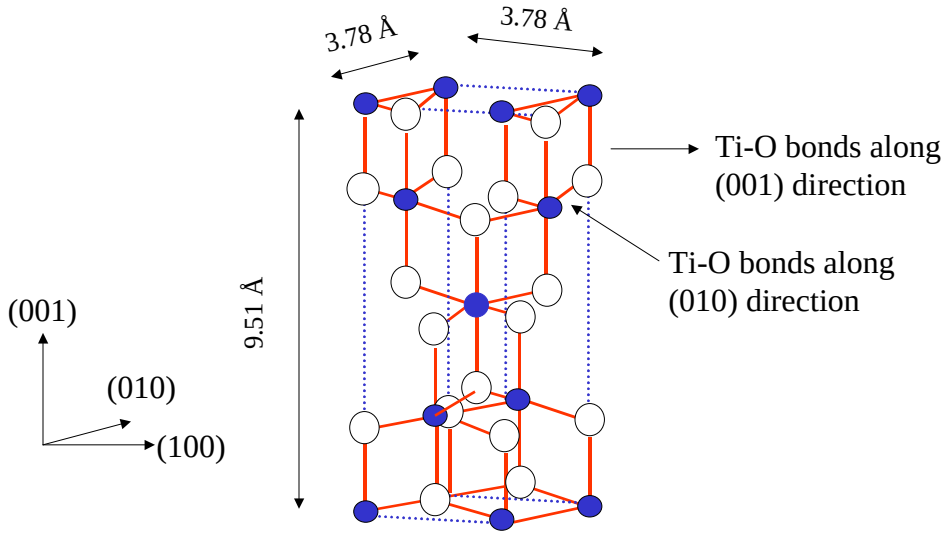

Figure III.11. *Unit cell parameters of anatase: the blue and white circles represent respectively the Ti and the oxygen atoms.*

III.3.2. TiO_2 and TiO_2-SiO_2 deposition details

TiO_2, SiO_2 and TiO_2-SiO_2 were deposited on p-type crystalline Si (100) substrates and also Si (111) using the ECR reactor described in chapter II.1. Differences were not observed in using one Si orientation or the other so here we report only the conclusions for oxides deposited onto Si (100) substrates.

For all samples the Si substrate was initially rinsed in 50:50 HF:H_2O, then blown dry. This removes most of the surface contaminants and also the native oxide. Prior to deposition the gases lines were evacuated (~ 10^{-7} Torr).

For all samples the uniformity of the film was typically limited to the central 2" region.

b) TiO_2 Plasma Enhanced Chemical Vapour Deposition

Several problems have been encountered in depositing TiO_2 primarily related to the uniformity of the oxide on the Si substrate. The reactor (Chapter II.1) was then modified. Actually the RF target was removed and a conical steel inox line was introduced as the

entrance for the Ti precursor gas (Chapter II.1, Figure II.1). This modification has several advantages:

- the substrate/gas entry distance of the precursor gases can be changed
- the precursors gases and the oxidants (O_2) are mixed only inside the chamber
- the precursors gases and the oxidants (O_2) are symmetrically distributed compared with Si substrate.

O_2 and $TiCl_4$ were used as precursor gases. $TiCl_4$ was used because of its very high partial pressure at low temperature (Figure III.12), so that the risk associated to deposition of TiO_2 inside the delivery lines was minimized. The vapor pressure was calculated using the Eq. III.9

$$\log_{10}(P) = A - (B / (T + C)) \qquad \text{III.9}$$

where A, B, C, are constants determined by [Luchinskii] and T is the temperature expressed in K. P is the vapor pressure in bar.

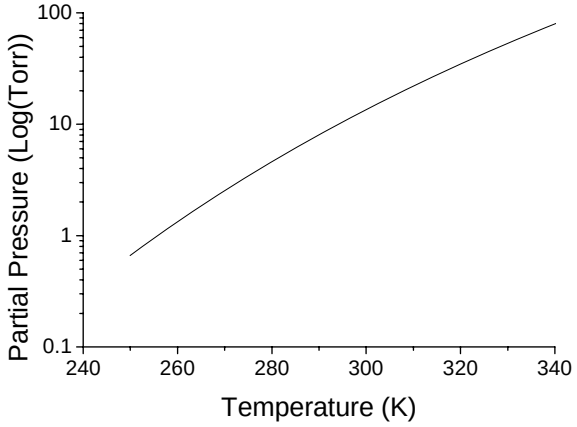

Figure III.12. *$TiCl_4$ vapor pressure calculated from Eq. III.9 using [Luchinskii] data for the A, B and C constants.*

The partial pressure of the oxidant and the precursor was optimized in order to obtain a stoichiometric and uniform TiO_2 film. Two deposition modes were used, both with the substrate temperature maintained close to room temperature (< 65 °C).

- **"floating" potential** with no substrate bias.

- **– 41 V substrate bias** was applied using radio frequencies (rf) biasing of the substrate. This method has been demonstrated [Mizutami] to enable densification of the film in the case of deposited SiO_2 and to enable crystallization of TiO_2 [Busani4].

O_2 was first introduced, then the plasma was ignited and finally the $TiCl_4$ was allowed in the chamber. This procedure was established because $TiCl_4$ is extremely reactive with O_2, so that it can easily deposit in the reactor or onto Si substrate. Samples of typical thickness of 250 nm were so obtained. In Table III.6 we show the "best" operating conditions [Busani6]. We observe that the TiO_2 deposited with – 41 rf bias has a very low deposition rate compared to all other samples presented in the Table III.6. This may be because the ions in the plasma contribute to densification of the material and also sputter the surface of the oxide.

Table III.6. *Summary of the deposition conditions used for the different samples described in this thesis. The sample identifiers are related to the expected concentration of the Si or Ti in the mixed oxide film. For example the $Ti_{0.5}Si_{0.95}O_2$ corresponds to a mole fraction of 5% of TiO_2 in the film [Busani6].*

Sample name	Partial gases pressures (10^{-3} Torr)		Thickness (nm)	Deposition rate (nm/min)
	O_2+SiH_4	$TiCl_4$		
SiO_2	3	0	84	3.35
$Ti_{0.5}Si_{0.95}O_2$	20.40	0.04	118	4.81
$Ti_{0.15}Si_{0.85}O_2$	9.52	0.04	119	4.63
$Ti_{0.25}Si_{0.75}O_2$	4.03	0.04	242	8.05
$Ti_{0.5}Si_{0.5}O_2$	4.03	0.11	278	9.22
$Ti_{0.75}Si_{0.25}O_2$	4.03	0.30	259	8.63
TiO_2	7.90	0.18	255	2.22
-41 RF TiO_2	7.90	0.18	220	1.1

b) SiO_2 Plasma Enhanced Chemical Vapor Deposition

Oxygen and SiH_4 were used as precursor gases. SiH_4 was diluted with Argon gas in the ratio of 20:1, to assure safety. The procedure followed was the same of that for TiO_2 deposition. In these conditions the refractive index of the deposited films was 1.46±0.003, they were homogenous across a 4" wafer and the dielectric constant was 3.75-3.85. These values can be considered the same as thermally grown oxide. We have also performed some rf bias voltage

assisted deposition as we did for TiO_2 samples. The results show that the refractive index increases slightly to 1.61. The small difference in these values allowed us to use the deposited non-assisted SiO_2 for our TiO_2-SiO_2 mixed oxides.
The experimental conditions that insure uniform distribution of the SiO_2 on silicon surface are summarized in the Table III.6.

b) TiO_2– SiO_2 or $Ti_xSi_yO_z$ Plasma Enhanced Chemical Vapour Deposition

Different concentrations of TiO_2 and SiO_2 were deposited onto Si(100). The deposition parameters (Table III.6) were adjusted in order to form desirable stoichiometric $Ti_xSi_yO_z$ For the lowest concentrations of Ti, working pressures of O_2 + Ar/SiH_4 were necessarily elevated so that the relative partial pressure of $TiCl_4$ could be reasonably adjusted. The partial pressure values were also determined to influence the uniformity of the deposited film. These values were chosen to optimize this. We underline, in particular, that the uniformity of the film varied significantly with the concentration of Ti in the plasma. It is not obvious to us why the greatest non-uniformity occurred for the highest Ti concentrations, it may in part be due to the distribution system for the precursor gas, $TiCl_4$.

III.3.3. Thermal annealing

Annealing was performed an all samples in order to be able to stabilize the pure material into either the rutile or the anatase phases. Annealing was also used to study the thermodynamic stability of the amorphous oxides bearing in mind that at 800 °C TiO_2 [Fukada] interacts with Si.

a) TiO_2

"Floating" plasma deposited TiO_2 was annealed over the temperature range of 20-600 °C. Typical annealing was performed for 30 min in a N_2 atmosphere. As we will describe in the following section, at 250 °C the amorphous oxide films start to form the anatase phase of TiO_2. At 600 °C the films seem to be completely transformed into anatase. The phase transformation depends upon the annealing time and the annealing temperature. Annealing at 400 °C for 65 h in N_2 was also performed: the results are the same for the sample annealed at 600 °C for 30 min.

–41 V substrate bias films were annealed in the same temperature range and for the same times as described for the "floating" plasma deposited TiO_2. It is relevant to remark that in the as deposited biased sample, anatase, rutile and amorphous phases coexist. Annealing at 600 °C results in a mixed anatase-rutile phase.

b) $TiO_2 – SiO_2$ or $Ti_xSi_yO_z$

The mixed TiO_2-SiO_2 samples were annealed up to 400 °C for 30 min in an N_2 atmosphere. In this range of temperatures they were amorphous, the annealing is performed, then, only for electrical characterization purposes.

In the following paragraphs we refer only to TiO_2 annealed at 250 °C and 600 °C and to $Ti_xSi_yO_z$ annealed at 400 °C.

III.3.4. Characterization

In this section we will discuss only TiO_2 and SiO_2 — TiO_2 samples. As already mentioned deposited silicon oxide film results are similar to thermal silicon oxides, so their properties are well known in literature.

a) XRD

The XRD data on TiO_2 samples are shown in (Figure 3 [Busani4]). We recall that as deposited samples without substrate bias applied show an amorphous structure. Once these samples were annealed up to 600 °C the anatase (101) peak increases in intensity and saturates after 30 min annealing at 600 °C or after 65 hours at 400 °C.

The biased deposited TiO_2 samples reveal the formation of anatase and rutile structures already for room temperature as deposited samples. Further annealing at 600 °C in N_2 shows that the residual amorphous structure of the as deposited oxide transforms into anatase and rutile. Unfortunately we were not able to stabilize the pure rutile phase, which occurs at temperatures > 800 °C [Tobar]. We cannot determine, using the XRD patterns, the relative concentration of the rutile and the anatase in these samples.

Preferred orientation in the deposited films was also investigated (Chapter II.3.4.1.3) and we conclude that there was no evidence for this effect.

The XRD data for $Ti_xSi_yO_z$ shows that as deposited and annealed samples at 400 °C for 30 min in N_2 atmosphere are amorphous, so no curves are reported.

NB: Our data contrast with those obtained on thin films of TiO_2 deposited using ion assistance of an O ion beam of energy 400 eV [Pecharroman]. In this case no evidence was found for rutile formation in the as-deposited films, only the anatase phase. Comparison with our data suggests that the energy of the ions assisting deposition may play a crucial role in determining if rutile/rutile "precursors" will be formed during the deposition process

b) Ellipsometry

Ellipsometry data on TiO_2 and mixed TiO_2-SiO_2 samples have been reported by [Busani4] and [Busani6]. In Table III.8 we show results for all sample considered for this thesis. We essentially notice that

- For TiO_2 deposited at room temperature without applied bias, further annealing causes an increase of the refractive index as well as the dielectric constant. This is consistent with the decreasing thickness, due to densification effects when the amorphous phase transforms into anatase.
- For TiO_2 deposited with –41 V bias the refractive index and the dielectric constant increase but the oxide thickness does not seem to change.
- In the case of mixed oxides, the refractive index seems to follow a linear regime as a function of the concentration of Si or Ti in the mixed oxide. This regime is plotted in Figure 3 of reference [Busani6] and the data presented in the Table III.8 are taken from this publication [Busani6]. The linear behavior also indicates that the TiO_2-SiO_2 compounds are well mixed and no segregation occurs. Indeed previous studies on xerogel titania silicates [Mountjoy] showed that for a concentration of at least 40 % of TiO_2 the mixed TiO_2-SiO_2 segregates into SiO_2 and TiO_2. Finally our data are consistent for what has been reported in the literature [Wang] [Boyd] for Ti concentrations > 40%. Unfortunately we did not find published data for lower Ti concentrations.

The linear variation of n with concentration confirms the analysis obtained using the IR peaks (following section).

c) FTIR

ca) TiO_2

Biased and unbiased, as deposited and annealed samples were analyzed using IR absorbance spectroscopy described in the Chapter II. A typical IR spectrum has shown in Figure III.13.

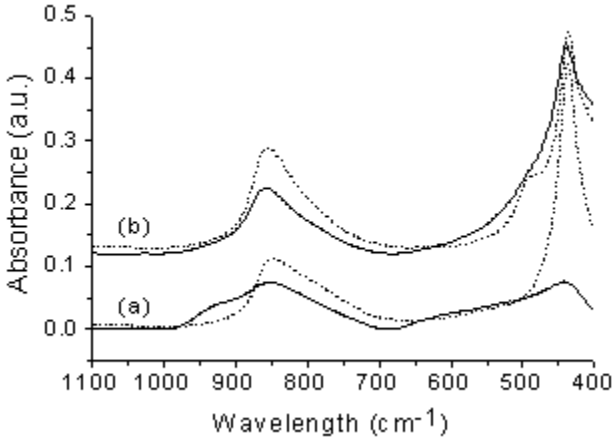

Figure III.13. *IR absorption spectra taken at 65 ° incidence angle. The solid lines always refers to as-deposited TiO_2 and the dashed lines are for the same samples annealed at 600 °C in an inert atmosphere. (a) Oxide deposited in "floating" bias conditions, (b) Oxide when a –41 V rf bias was applied [Busani4].*

The lower curves (a) are the IR spectra for those samples deposited in "floating" bias. The solid line is the absorption for as-deposited TiO_2. The broad peaks in the region of 400-600 and 700-950 cm^{-1} are due respectively to TO and LO vibrations of the Ti-O bonds: they evidence the amorphous structure of the oxide film. After annealing at 600 °C, (dashed line in Figure III.13a), two narrow intense peaks clearly appear at 432 and 853 cm^{-1} and can be assigned to the TO and LO modes for the anatase phase [Pecharroman] [Scarel]. Observing the solid curve in Figure III.13b, the same vibrations are found for the as-deposited TiO_2 when –41 V substrate bias was applied. We also observe the beginning of a peak at 493 cm^{-1} that becomes evident after annealing at 600 °C for 30 min in N_2 atmosphere (dashed line). This last peak is a Ti-O vibration in rutile [Peng] and indicates that the sample is a mixture of anatase and rutile. Unfortunately, due to the wavelength limit of the instrument, we cannot

measure with precision the full width of the half maximum for the TO peaks, and we are unable to estimate the degree of crystallinity of the oxides.

Using the 1070 cm^{-1} absorbance of the Si-O stretching vibrational mode for Si-O bonds we can ascertain the importance of a possible Si-O-Si interfacial layer. [Busani4] concluded that both annealed and deposited samples are stable in contact with Si or no relevant interfacial layer is formed during the early stages of the deposition.

No evidence of chlorine has been detected with IR since an absorbance peak at 600 cm^{-1} should be evident in Figure III.13 if Ti-Cl bonds were present.

cb) $TiO_2 – SiO_2$ or $Ti_xSi_yO_z$

Normal incidence IR spectra of mixed oxides was measured for all samples and the results are presented in the Figure III.14. As reported in the literature the Si – O – Ti^{4+} bonds should introduce an absorbance band at ~ 900 cm^{-1} [Kotami] [Brassard]

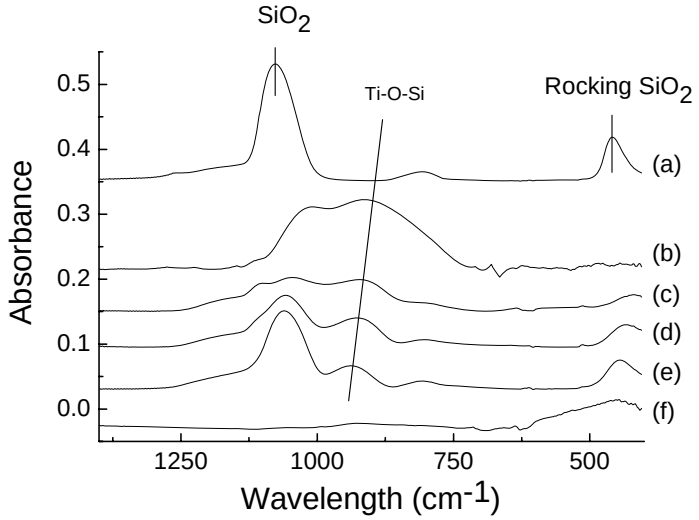

Figure III.14. *Normal incidence IR absorbance for different $Ti_xSi_yO_z$. (a) Pure SiO_2, (b) $Ti_{0.75}Si_{0.25}O_2$ (c) $Ti_{0.5}Si_{0.5}O_2$ (d) $Ti_{0.25}Si_{0.75}O_2$ (e) $Ti_{0.15}Si_{0.85}O_2$ (f) amouphous TiO_2 [Busani6].*

From Figure III.11 we notice that, once the TiO_2 is introduced into the SiO_2 matrix, a peak in the region of 900-950 cm^{-1} appears which becomes increasingly important for higher Ti concentrations. This peak moves from 903 cm^{-1} for the highest Ti concentration ($Ti_{0.75}Si_{0.25}O_2$) to 935 cm^{-1} for the lowest Ti concentration ($Ti_{0.15}Si_{0.85}O_2$)

Using the relative intensities of these peaks it is possible to approximately estimate the concentration of the Ti-O-Si and Si-O-Si bonds, hence the concentration of Ti in the mixed oxide. This method has been described in detail by [Busani6] so we show only the results in Table III.7.

The results for the annealed samples do not show visible differences in the spectra so they have not been reported. This confirms the absence of crystalline centers in the films which might have resulted from the annealing process.

d) EDS-RBS

Energy Dispersive X-ray spectroscopy (EDS) and Rutherford-Backscattering (RBS) were performed on all $Ti_xSi_yO_2$ samples. EDS was carried out soon after mixed oxide deposition in the CHTM clean room facility (Chapter II.4) using a JEOL JSM 5800 system that combines the Scanning Electron Microscope (SEM) and EDS. A maximum 8-inch diameter wafer can be loaded in the chamber and full 7-inch diameter area can be observed. The acceleration voltage can be widely varied from 0.3 to 30 keV with a 100 V steps, the work distance (WD) spans from 8 to 48 mm, for a minimum resolution of 50 nm. The zoom mode is 18 X for a WD of 48, until 300.000 X. The probe current is from 10^{-12} to 10^{-6} A. Image and EDS acquisition is finally accomplished using Oxford Windows software, which allows X-ray line identification (qualitative analysis), quantitative analysis (elements concentration) and X-ray mapping. For flat, polished homogeneous samples, quantitative analysis can provide a relative accuracy of 1-3% when appropriate standards are available. For elements with $Z < 5$ the sensitivity is lower than 1% so that it is almost impossible to detect low atomic weight elements.

For this measurement TiO_2-SiO_2 mixed oxides were deposited onto GaAs substrates for few reasons. First we cannot clearly ascertain the concentration of Si in the TiO_2-SiO_2 film if the substrate is composed of Si. Second the Si substrate always has a high concentration of oxygen (Czochralski) as we demonstrated in Chapter II.3.2.3, which confuses determination of the O concentration in the film. Third to minimize the substrate effect. For example the K_{α_1} emission for As and Ga is respectively 10.54 and 9.51 keV, much larger than that of Ti (4.51 keV) and Si (1.74 keV). Finally thin film corrections requires to introduce the ratio of the measured energy peak area and the standard energy area peak in the GMRFILM free software. The standards used for Ti and Si energy peak were 500 nm samples of SiO_2 and

TiO_2. More details can be found in [Busani6]. Here, in Table III.7 we simply show the results.

RBS was performed by X. Yu and Hye-Won Seo at the University of Huston in Texas. Details about the experimental procedure are described in [Busani6]. In Table III.7 we also show the results of analysis drawn from these measurements and the statistical Ti-O-Si bond distributions calculated using our Monte Carlo algorithm.

Table III.7. *Percentage Ti concentration in TiO_2-SiO_2 mixed oxides. The first column refers to "expected" concentration from the partial gas pressure during the deposition, the second and third columns refers to the bond distribution calculated using a MonteCarlo simulation (Figure 2 in [Busani6]), and the last 3 columns refer to the concentration measured using different techniques.*

	Si-O-Si	Ti-O-Si	FTIR	EDS	RBS
SiO_2	100	0	100	100	100
$Ti_{0.05}Si_{0.95}O_2$	0.9026	0.0949	-	8	5.24
$Ti_{0.15}Si_{0.85}O_2$	0.8089	0.1802	11	10	9.4
$Ti_{0.25}Si_{0.75}O_2$	0.5625	0.3751	34	34	31.7
$Ti_{0.5}Si_{0.5}O_2$	0.25	0.4999	50	60	55
$Ti_{0.75}Si_{0.25}O_2$	0.0624	0.3751	87	90	79

Table III.7 contains relevant information in order to calibrate the deposition conditions such as the gas pressure of the precursors required to obtain a desired $Ti_xSi_yO_2$ concentration. Once, the approximate value of the composition of the mixed oxide was determined via deposition gas partial pressures, it was enough to use the ellipsometry measurements (quick and non destructive). Our results appear to indicate that a linear relationship exists between the Ti concentration and the refractive index.

e) Electrical measurements

The dielectric constant was measured for TiO_2 and mixed oxides. In Table III.8 we summarize the information obtained from these measurements.

As deposited without – 41 V bias TiO_2 usually shows a dielectric constant ~ 38-33 as determined from C(V) measurements. An example is shown in Figure III.15a. The red C(V) curve is characteristic of as deposited TiO_2. The curve is not "stretched out" and the flat

band voltage is situated at 0.93 V. The oxide thickness was 117.4 nm and the Al metal contact surface was 0.00198 cm^2. Hysteresis was observed when a constant bias was applied. The green and black lines are representative of a positive bias electric field of 1 MV/cm applied for 1 min and then 10 minutes. We see that the V_{FB} is considerably shifted towards a positive value of 4.85 V corresponding to negative charge trapping in the dielectric. Then a negative bias electric field of –1 MV/cm was applied for 10 minutes. The V_{FB} (blue curve) is now shifted towards negative value of –3.39 corresponding to positive charges being present in the dielectric. The sample was then annealed at 600 °C for 30 min, so that almost entirely anatase phase was observed (XRD and IR sections of this chapter). The dielectric constant rose to 74-80 and the hysteresis was eliminated (Figure III.15b red and blue curve). Unfortunately the leakage currents rose from 10^{-8} A/cm^2 for the as deposited samples to 10^{-3} A/cm^2 for the annealed films (1 MV cm^{-1} electric field).

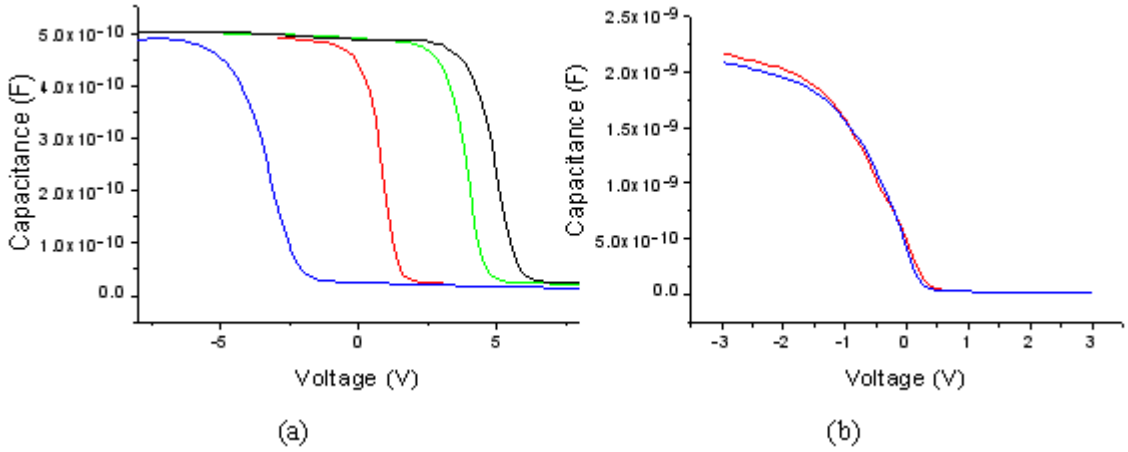

Figure III.15. *(a) C(V) for unbiased as deposited TiO_2 and (b) for the same sample annealed at 600 °C for 30 min in N_2.*

TiO_2 deposited with –41V substrate bias was also characterized electrically in the same way as we described for the unbiased sample. We show the results in the Table III.8. The as deposited samples are a mixture of anatase, rutile and amorphous TiO_2. The C(V) curves were so stretched out that it was not possible to determine the dielectric capacitance. So a metal-insulator-metal (MIM) structure was constructed in order to measure the absolute value of the dielectric constant, it was 78-85 for the as deposited – 41 V biased samples and 105-123 for the sample annealed at 600 °C for 30 min in N_2.

Mixed TiO_2-SiO_2 MOS capacitors yielded maximum values of k~ 38 for high concentrations of TiO_2 and this value decreased as the SiO_2 concentration increased as shown in Figure 3 of [Busani6] and as indicated in Table III.8. For mixed $Si_{1-x}Ti_xO_2$ compounds the value of the dielectric constant is higher than that which has been reported [Brassard] for nano-crystalline and much higher than the typical value of 10-15, which has been reported for other silicates [Wilk]. We also observe that the *k* seems to behave linearly as a function of the Ti concentration, as was observed for the refractive index. Current density versus voltage (I(V)) measurements at 1 MV cm^{-1} for all the deposited, mixed films show acceptable insulator behavior: the sample with the highest Si concentration has a typical value of j =10^{-7} A/cm^2, which decreases to 10^{-8} A/cm^2 for the samples with the highest Ti concentration.

f) AFM

AFM measurements were performed only to confirm the change in roughness upon thermal treatment. It was already told that the diffusion of the laser spot, during ellipsometry measurements, is an indication of the presence or absence of roughness and/or the crystallinity of the film. The SiO_2- TiO_2 mixed oxide usually presents a very small roughness even after low temperature annealing at 400 °C in N_2. This confirms the amorphous nature of these oxides, and the crystalline structure of the annealed and bias deposited TiO_2.

Table III.8. *Summary of the most important physical parameters measured or calculated for TiO_2 and mixed TiO_2-SiO_2. The thickness of the oxide d_{ox} is measured with an error of ± 0.5 nm, the flat band voltage with a typical error of ± 0.2 V, the density ρ with an error of ± 0.2 g/cm^3. The dielectric constant is an average of the anisotropic value or of the measured value. The column called "Phase" refers to Amorphous (Am), Anatase (A) and Rutile (R) phases of TiO_2.*

Sample name	d_{ox} (nm)	n	*Average k*	ρ (g/cm^3)	Phase	Rough (nm)	V_{FB} (V)
Rutile	-	2.5-2.7	117[c]	4.2[b]	R	-	-
Anatase	-	2.4	45[d]	3.8[b]	A	-	-
SiO_2	85	1.46	3.85	2.35	Am	-	-
$Ti_{0.05}Si_{0.95}O_2$	116	1.482	5.5		Am	-	0.1
$Ti_{0.15}Si_{0.85}O_2$	170	1.512	6.9		Am	-	-0.2-0.3
$Ti_{0.25}Si_{0.75}O_2$	138	1.658	19		Am	-	-0.6-0.7
$Ti_{0.5}Si_{0.5}O_2$	268	1.821	28		Am	-	-0.2-0.4

$Ti_{0.75}Si_{0.25}O_2$	283	2.23	38		Am	-	-0.5-0.6
TiO_2	130	2.25	33-35	3.25	Am	1.2	0.9-1.1
TiO_2 ann 250 °C	2.55	2.3			Am+A		
TiO_2 Ann 600 °C	2.37	2.48	74-84	3.62	A	6.51	0.24
-41 rf TiO_2	198	2.3-2.46	85-78[a]	-	Am+A+R		-
-41 rf TiO_2 Ann 600 °C	202	2.5-2.7	105-123[a]	3.85	A+R	7.45	

a= from Metal-oxide-metal structure b=[Tang2] c=[Tang] d=[Mikami]

From all these results we finally conclude:

- Rutile precursors were found in pure TiO_2 at room deposition temperature
- Anatase forms at 250 °C. Pure rutile was not obtained due to the high temperature Ti-Si reaction which coincides with its formation temperature.
- Refractive indexes and dielectric constants shows linear behavior as a function of the Ti content in mixed TiO_2-SiO_2.
- SiO_2 was diluted with different Ti concentrations and no evidence of TiO_2 or SiO_2 segregation was noted.
- Combining IR, RBS, EDS, ellipsometry and Monte Carlo data we found a non destructive method to measure the Ti or Si content in the SiO_2-TiO_2 mixed films.
- amorphous samples show a dielectric constant of 33, low leakage current density ($\sim 10^{-8}$ A/cm^2) but very significant hysteresis.

III.3.5. Discussion

[Shannon] suggested that for a large number of ternary and more complex oxides an additivity rule may be applied to estimate the dielectric constant of an oxide mixture. The assumption is that the molecular polarizability of the mixture is given by Eq. III.5.
The limit of this model, as already explained in Chapter III.1.6 , it is that the model itself ignores any changes in the vibrational component of the polarizability.

In the case of SiO_2 polymorph and SiO_2 Stishovite [Devine2] has clearly shown how both electronic and vibrational components of the polarizability increase with the molecular volume (or with decreasing of the density).

TiO_2 polarizibility behavior for the samples described in this thesis has been investigated by [Busani6] [Devine2]. If we know the dielectric constant, the refractive index and the molecular volume (i.e. the density) we can calculate the value of $(\alpha_{vib} + \alpha_{elec})$ and α_{elec} Introducing the dielectric constant and the densities given in the Table III.8 into the Eq. III.1 and introducing the refractive index into eq III.2 we obtain the polarizibility values for the Ti oxides studied. These results are shown in Figure 4 and 5 of reference [Busani6] and show how the polarizibilities increase whilst the density decreases. Moreover the samples containing anatase and rutile (deposited using –41 V rf bias and also annealed at 600 °C) and the sample containing mostly anatase (as deposited and annealed at 600 °C) showed much higher vibrational polarizibilities than one can predict. The electronic component seems not to vary significantly. Indeed this would be expected since α_{elec} derives from the electronic structure of the component ions (O^- and Ti^+) which may remain relatively constant from phase to phase. The vibrational component α_{vib} clearly depends upon the structure and bonding of the Ti and the O [Bunget] i.e. the structure of the TiO network (chapter III.1.5).

We now make the assumption (as the additivity rule supposes) that when the oxide changes from one phase to another, the term $(\alpha_{elec} + \alpha_{vib})$ does not change. Then we consider amorphous TiO_2, which has a dielectric constant of 33 and a molecular volume of 41.07 x 10^{-24} cm^3 ($\rho = M/V_m$). From the equation III.1 we derive the value of the polarizability, which is 8.96 x 10^{-24} cm^3. Now we examine the case of rutile. Using the additivity rule we can consider that the molecular volume varies with the phase transition from amorphous to crystalline rutile. Using the density value for rutile given in Table III.8 (i.e. V_m= 31.4 x 10^{-24} cm^3) and the polarizability of the amorphous phase (8.96 x 10^{-24} cm^3) one can determine the value of the dielectric constant for the rutile. This value is ~ -17, which is considerably different from the value calculated using the Eq. III.5. If the polarizability changes slightly from 8.96 x 10^{-24} cm^3 to 9.5 x 10^{-24} cm^3 the dielectric constant should be –13.53. Finally we note that the vibrational component α_{vib} should increase if the molecular volume decreases (Eq. III.4) whereas experimentally the inverse is true. We are thus led to conclude that a reduction of ω_0 results as a function of molecular volume through variation of the force

constants. This reduction must override the variation due solely to molecular volume variation.

On the basis of this analysis we conclude that both electronic and vibrational components of the polarizability increase with increasing molecular volume in the network. This variation shouldn't be neglected. In fact even the electrical polarizability doesn't vary dramatically. These small changes can considerably influence the dielectric constant. Again as we already demonstrated for the $LaAlO_3$ films, the additivity should be used with some caution.

Mixed TiO_2-SiO_2 has demonstrated to have a linear behavior with respect to dielectric constant and refractive index. The announced increasing of the density (i.e. Zr silicate) does not occurs because, even TiO_2 is much more polarizable ion than silica, Ti diluted in the SiO_2 tents to replace Si in the tetrahedral coordination. This is maybe due to the similarity in the SiO_2 and TiO_2 structures.

We did not measure the optical band gap. For SiO_2 it is 9 eV and for TiO_2 it is 3.5 eV. From Eq. III.4 the band gap is related to the vibrational component of the polarizability. If we assume that the band gap follows a linear relationship with Ti concentration, for the case of $Ti_{0.5}Si_{0.5}O_2$ the band gap should be 6.25 eV. For that mixture the dielectric constant was measured to be 28 (Table III.8) so that the combination of the band gap and the dielectric constant could make this mixed oxide attractive. Unfortunately, due to the high Ti concentration, such mixed oxide might not be stable on Si when high temperature processing occurs.

REFERENCES

[Abrashev] Abrashev, M.V.; Litvinchuk, A.P.; Iliev, M.N.; Meng, R.L.; Popov, V.N.; Ivanov, V.G.; Chakalov, R.A.; Thomsen, C., Phys. Rev., **B 59**, 4146 (1999)

[Baur] V. W. H. Baur, Acta Crystallogr., **14**, 214 (1961)

[Boyd]

[Brassard] D. Brassard, D. K. sakar and M. A. El Khakani, J. Vac. Sci. Technol. A, **23**, 851 (2004)

[Brauer] G. Brauer and B. Pfeiffer, Z. Anorg. Allgem. Chem. **341**, 237 (1965)

[Bunget] Bunget, I. And Popescu, "M. Physics of Solid Dielectrics", Chapt. 1 Elsevier, New York (1984)

[Busani] T. Busani and R. A. B. Devine, Proc. Mat. Res. Soc. Symp. **786** (2004)

[Busani2] T. Busani and R. A. B. Devine J. Appl. Phys., 6642, **96**, (2004)

[Busani3] T. Busani and R. A. B. Devine, J. Appl. Phys. **98,** 044102 (2005)

[Busani4] T. Busani and R. A. B. Devine, Semicond. Sci. Technol.. **20,** 870 (2005)

[Busani5] H. Edwards, T. Busani, R. A. B. Devine and A. Pineda, NATO Science Series II: Mathematics, Physisc and Vol. 220 (2005)

[Busani6] T. Busani and R. A. B. Devine, J. Vac. Sci. Technol. A, **24**, 369 (2006)

[Busani7] T. Busani, R. A. B. devine and P. Gonon, ECS **1**, 331 (2006)

[Cromer] D. T. Cromer and K. Herrington, J. Am. Chem. Soc. **77**, 4708 (1955)

[Devine] R. A. B. Devine, J. Appl. Phys. **93** 9938 (2003)

[Devine2] R. A. B. Devine and T. Busani, Appl. Phys. Lett. **86**, 062902 (2005)

[Dong] X. Dong, G. H ong, D. wang and Y. Cui, Proc. SPIE . **2897**, 210 (1996)

[Dulepov] E. V. Dulepov and S. S. Batsanov, Zhurnal Strukturnoi Khimii, **13**, 935 (1972)

[Eyring] L. Eyring and N. C. Baenziger, J. App. Phys. **33**, 429 (1962)

[Fukuda] H. Fukuda, S. Namioka, M. Miura, Y. Ishikawa, M. Yoshino and S. Nomura, Japan. J. Appl. Phys. **38**, 6034 (1999)

[Goldschmidt] V. Goldschmidt, Geochemistry, Oxford University Press (1958)

[Gonzalez] R. J. Gonzalez, R. Zellen and H. Berger, Phys. Rev. B, 55, 7014 (1997)

[Grimes] N. W. Grimes and R. W. Grimes, J. Phys. Condens. Matter **10**, 3029 (1998)

[He] G. He, M. Liu, L.Q. Zhu, M. Chang, F. Fang and L.D. Zhang, Surf. Sci.

516, 67 (2005)

[Henderson] G. S. Henderson, X. Liu and M. E. Fleet, Mineralogical Magazine, 67, 597 (2003)

[Honda] K. Honda, A. Sakai, M. Sakashita, H. Ikeda, S. Zaima and Y. Yasuda, Japanese J. Appl. Phys. **43,** 1571 (2004)

[Houssa] M. Houssa, M. De Gent, J. L. Autran, G. Groeseneken and M. M. Heyns, Appl. Phys. Lett, **85**, 2101 (2004)

[Iuga] D. Iuga, S. Simon, E. de Boer and A. P. M. Kentgens, J. Phys. Chem. **B103,** 7591 (1999)

[jade] Material Data Inc. 1224 Concannon Blvd.Livermore, California 94550

[Jeon] S. Jeon, K. Im, H. Yang, H. Lee, H. Sim, S. Choi, T. Jang and H. Hwang, Proc. IEDM, 20.6.01 (2001)

[Kang] S-K. Kang and H. Ishiwara, Jpn. J. Appl. Phys. **41 Pt. 1** 6899 (2002)

[Kotami] Y. Kotani, A. Matsuda, M. Tatsumisago, T. Minami, T. Umezawa and T. Kogure, J. Sol-Gel Sci. and Tech., **19**, 585 (2000)

[Kulkly] K. Kukly, J. Ihanus, M. Ritala amd M. Leskela, Allp. Phys. Lett. **68**, 3737 (1996)

[Kurtz] H. Kurtz and R. A. B. Devine, Appl. Phys. Lett. **79**, 2342 (2001)

[lanthanide] "A lanthanide Lanthology Part 1, A-L", Molycorp. Inc., Mountain View, California (1993)

[Lee] B. H. Lee, L. Kang, W. J. Qi, R. Nieh, Y. Jeon, K. Onishi and J. C. Lee, IEDM Tech. Dig., **133** (1999)

[Lo Nigro] R. Lo nigro and R. G. Toro, Adv. Mater., **15**, 1071 (2003)

[Lo Nigro2] R.L. Nigro, V. Ranieri, C. Bongiorno, R. Toro, G. Malandrino and I. G. Fragala, Appl. Phys. Lett. **83**, 129 (2003)

[Lu] X-B. Lu, Z-G. Liu, Y-P. Wang, Y. Yang, X-P. Wang, H-W. Zhou and B-Y. Nguyen, J. Appl. Phys. **94** 1229 (2003)

[Luchinskii] G.P Luchinskii, Zh. Fiz. Khim., **40**, 593 (1966)

[Lucovsky] G. Lucovsky and G. B. Rayner, Jr. Appl. Phys. Lett. **77**, 2912 (2000)

[Martin] P. J. Martin, A. Bendavid and H. takikawa, J. Vac. Sci. Technol. A **13**, 596 (1999)

[Martinet] C. Martinet, R. A. B. Devine and M Brunel, J. Appl. Phys. **81**, 6996 (1997)

[Mikami] M. Mikami. S. Nakamura, O. Kaito and H. Arakawa, Phys. Rew. B, **66**, 155213 (2002)

[Mizutami] T. Mizutami, Mat. Res. Soc. Symp. Proc. **284**, 265 (1993)

[Mountjoy] G. Mountjoy, M.A. Holland, P. Gunawidjaja, G.W. Wallidge, D.M. Pickup, R.J. Newport and M.E. Smith, J. Sol-Gel Sci. and Tech., **26**, 161 (2003)

[Mountjoy2] G. Mountjoy, D. M. Pickup, R. Anderson, G. W. Wallidge, M. A. Holland, R. J. Newport and M. E. Smith, Phys. Chem. Phys., **2**, 741 (1998)

[Neumayer] D. A. Neumayer and E. Cartier, J. Appl. Phys. **90**, 1801 (2001),

[Okada] T. Okada, M. Shajahan, K. Sawada and M. Ishida, Jpn. J. Appl. Phys. **44,** 2320 (2005)

[Ono] H. Ono and T. Katsumata, Appl. Phys. Lett. **78**, 1832 (2001)

[Osten] H. J. Osten, A. Fissel, H. J. Mussig U. Schwalke, K. Boye, K Aberle, R. Heller, G. hess, G. Muller, T Ruland and G. Tzcholckel, ESSD ERC, **407** (2002)

[Osten2] H. J. Osten, E. Bujiel, J. Dabrowki, A. Fissel, T. Guminskaya, J. P. Liu, H. P. Mussig and P. Zaumseil, IWGI Tokyo (2001)

[Park] B. E.Park and H. Ishiwara, Appl. Phys. Lett. **82** 1197 (2003)

[Park1] B. E. Park and H. Ishiwara, Appl. Phys. Lett. **79** 806 (2001)

[Pecharroman] C. Pecharroman, F. Gracia, JP. Holgado, M. Ocana, AR. Gonzalez-Elipe, J. Bassas, J. Santiso and A. Figueras, J. Appl. Phys, **93**, 8, 4634 (2003)

[Peeters] J. Peeters and Li Li, J. Appl. Phys. **72**, 719 (1992)

[Peng] GW. Peng, SK. Chen and HS. Liu, Appl. Spectroscopy, **49**, 11, 1646 (1995)

[Puthenkovilakam] R. Puthenkovilakam, Y-S Lin, J. Choi, J. Lu, H-O Blom, P. Pianetta, D. Devine, M. Sendler and J.P. Chang, J.Appl. Phys, **97,** 023704 (2005)

[Qi] W. J. Qi, R. Nieh, B. H. Lee, L. Kang, Y. Jeon, K. Onishi, T. Ngai, S. Banerjee, J. C. Lee, IEDM Tech. Dig. **145**, (1999)

[Ramirez] A. P. Ramirez, J. Phys. Cond. Mat. **9**, 8171 (1997)

[Rango] C. De Rango, G. Tsougaris and C. Zelwer, Acta crystallogr. **20**, 590 (1966)

[Rozhkov] V. A. Rozhkov, A. Yu. Trusova and I. G. Berezhnoy, Thin Solid Films, **325**, 151 (1998)

[Saine] M.C. Saine, E. Husson, and H. Brusset, Spectrochimica Acta **73A**, 985 (1981)

[Samara] G. A. Samara, J. Appl. Phys. **68**, 4214 (1990)

[Sangster] M. J. L Sangster and A. M. Stoneham, Phil. Mag. B, **43**, 597 (1981)

[Scarel] G. Scarel, C. J. Hirschmugl, V. V. Yakovlev, R. S. Sorbello, C. R. Aita, H. Tanaka and K. Hisano, J. Appl. Phys. **91**, 1118 (2002)

[Shannon] R. D. Shannon, J. Appl. Phys. **73**, 348 (1993)

[Srim] The TRIM software is available for free download on: www.srim.gov

[Sukuzi] M. Sukuzi, M. Tomita, T. Yamaguchi and N. Fukushima, IEDM, Tech. Dig., 445 (2005)

[Tang] H. Tang, K. Prasad, R. Sangines, PE. Schmid and F. Levy, J. Appl. Phys., **75**, 2042 (1994)

[Tang2] H. Tang, H. Berger, PE. Schmid, F. Levy and G. Burri, Solid State Commun. 87, 874 (1993)

[Taspinar] E. Taspinar and A. C. Tas, J. American Chem. Soc. **80**, 133 (1997)

[Tobar] M. E. Tobar, J. Krupka, E. N. Ivanov and R. A. Woode, J. Appl. Phys., **83**, 1604 (1998)

[Tryoso] D. H. Triyoso, M. Ramon, R. I. Hegde, D. Roan, R. Garcia, J. Baker, X. D. Wang, P. Fejes, B. E. White and P. J. Tobin, J. Electrochem. Soc. **152**, G203 (2005)

[Wallace] R. M. Wallace, Appl. Surf. Sci. 231-232, **543** (2004)

[Wang] Z. M. Wang, Q. Fang, J. Y. Zhang, J. X. Wu, Y. Di, W. Chen, M. L> Chen and I. W. Boyd, Thin Solid Films, **453**, 167 (2004)

[Wilk] G. D. Wilk and R. M. Wallace, Appl. Phys. Lett. **76**, 112 (2000)

[www] www.matweb.com

[Xiang] W. Xiang, H. Lu, L. Yan, H. Guo, L. Liu, Y. Zhou, J. Jiang, H. Cheng and Z. Chen, J. Appl. Phys. **93**, 533 (2003)

[Yogogawa] Y. Yokogawa, M. Yoshimura and S. Somiya, J. Mater. Sci. Lett. **10**, 509 (1991)

[Derighetti] B. Derighetti, J. E. Drumheller, F. Laves, K. A. Muller and F. Waldner, Acta crystallogr. **18**, 557 (1965)

CONCLUSION

In modern microelectronics the need for knowledge of materials science is becoming dominant. The necessity to achieve the objectives established as Moore's law is demanding that technology be able to make transistors based on almost nano-scale dimensions. There are essentially two types of materials of interest: metals and insulators. For the insulator, the main technological problem is to find a replacement for SiO_2. Such a material is known as high-k. We demonstrated the large number of variables that play a role in technological processes and that these variables are somewhat related each other. For gate oxides we can summarize the technological issues into three main categories: first the oxide should have a high permittivity value, second it should have a significant optical band gap to avoid electron injection from Si or the gate electrode material into the oxide, third it should be stable in contact with Si. These variables can be considered separately but never out of the context of the one another. For an insulator material in contact with Si we have therefore tried to understand how the structural properties of the oxide are correlated with its optical and physical properties and how this correlation influences the microelectronic application. It is obvious that this analysis can be extended to other materials.

We have considered different oxides, and we have deposited or grown them using plasma based methods such as PECVD, sputtering and plasma anodic oxidation. Also electron beam evaporation and thermal dry oxidation were used. We chose to work in a class 1000 clean room in order to minimize the possibility of Si surface contamination prior to oxide deposition. In this way we removed some possible variables during the sample manufacture process.

The characterization of the oxides was carried out using a variety of tools and techniques. The importance of these techniques resides in the necessity to determine all the fundamental structural and physical parameters of the oxide. The structural properties of the materials were studied using techniques such as, X-ray diffraction and reflectivity, EDS, FTIR, AFM, XPS and RBS. Finally information about the macroscopic variables (i.e. dielectric constant and refractive indices) was obtained by electrical and ellipsometry measurements.

Ternary $LaAlO_3$ oxide was studied because of its high dielectric constant and because of its stability with silicon. We have demonstrated that the high-k phase (the one with $k = 28$) is only achievable for crystalline oxides. Indeed, although the polarizibilities of the crystalline and amorphous phases are not very different the major change in the dielectric constant is due to variation of the molecular volume (i.e. density). Crystalline $LaAlO_3$ is more dense than the amorphous phase. Unfortunately this phase forms at temperature higher than 800 °C. Much effort has been expended in order to obtain such a phase, but all annealing processes > 700 °C contribute to deteriorate the Si/oxide interface, and so degrade the electrical properties of MOS structure. This clearly limits the use of these oxides for MOSFET applications.

Pr_2O_3 and Nd_2O_3 rare earth oxides were obtained in both amorphous and crystalline phases. The interaction between the oxide and Si substrate was limited at 900 °C. The dielectric constant of the amorphous phase appears to be remarkably inferior as compared with the crystalline oxides. We have noted that these oxides can essentially form two different crystalline phases: cubic and hexagonal. The formation of one or the other of these structures depends upon the atomic number of the rare earth metal. The relationship between the density and the structure was evidenced and its influence on the macroscopic properties of the insulator was underlined. Finally the formation and the stability of these phases depends upon the process used to deposit the oxide, which is very relevant from a technological standpoint in microelectronic chip fabrication.

Mixed SiO_2 - TiO_2 films were deposited with a range of different Ti concentrations. Pure titanium oxide was initially deposited and characterized. It shows a thermodynamic instability with respect to the Si substrate at high temperatures and also a finite anisotropy in the macroscopic properties. A dielectric constant of 33 was determined for amorphous TiO_2. Crystalline rutile and anatase were also obtained, but the crystalline phases are very sensitive to thermal treatment below temperatures of 200 °C. The mixed oxides did not show any TiO_2 crystalline phase or amorphous SiO_2 or TiO_2 segregation for temperatures < 600 °C. Macroscopic variables such as the dielectric constant and the refractive index seem to behave linearly with a maximum (pure TiO_2 value) and a minimum (pure SiO_2 value). As an example

$Ti_{0.5}Si_{0.5}O_2$ alloys had a dielectric constant of 27 with an estimated optical gap of 6.25. However, annealing of these alloys at temperatures higher than 600 °C results in segregation of SiO_2 and TiO_2 and possible formation of rutile and/or anatase nano-crystals.

Replacing SiO_2 is not easy, but is not impossible. We have discussed most of the issues related to this problem, and we have clearly understood that a) an ideally amorphous gate oxide is not achievable with a dielectric constant higher than 25 b) almost all the possible high-k candidates form a small interfacial layer at the Si/oxide interface. This is considered disastrous for future technological evolution, especially when the EOT is expected to be less than 1 nm. Suppose, for example we consider two oxides: one with a k = 12 and one with a k value of 25. An oxide with k =12 is what microelectronic companies are able to process at the present time. It is instructive to plot the EOT versus the real thickness of the oxide (figure I).

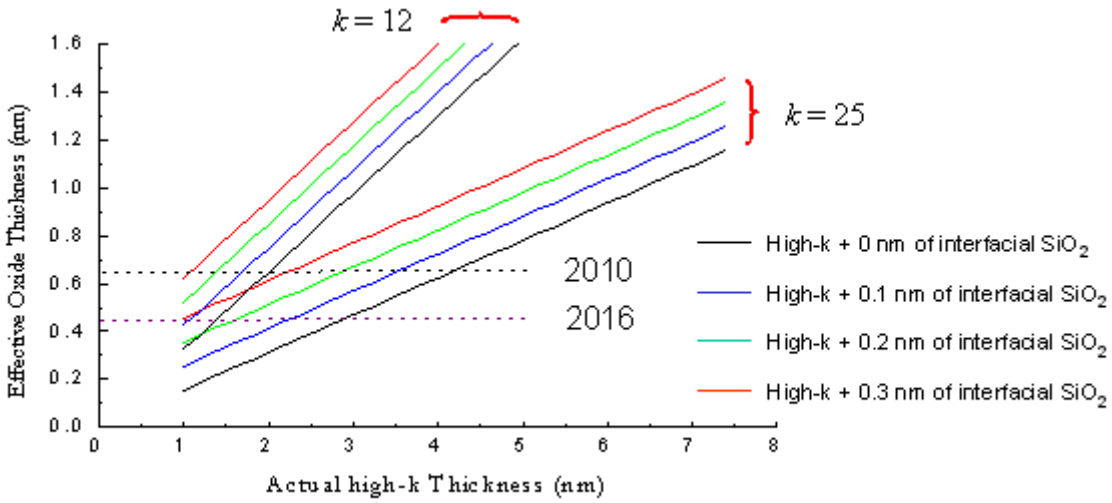

Figure I. *EOT versus the real oxide thicknesses. Different lines refer to different interfacial SiO_2 thicknesses at the interface high-*k/Si:

In a more realistic case a small amount of interfacial SiO_2 will almost surely form between the Si channel and the gate oxide. The results are shown in figure I. The black lines refer to the case in which no interfacial oxide is present, and the blue, green and red lines are associated respectively to the case of 0.1, 0.2 and 0.3 nm of SiO_2 interfacial oxide. It is

evident that for the year 2010 a "perfect" oxide could be produced, with a physical thickness of 2.5 nm. But, in 2016, using the same oxide, with a physical thickness of less than 2 nm should be produced. If a layer of only 0.3 nm of SiO_2 is formed at the interface between he Si and the gate oxide, in 2010 and 2016 the physical thicknesses of the oxides with k = 25 and k = 12 should be respectively less than 2 nm and less than 1 nm, the latter being certainly technologically infeasible. In fact, even if physically a high-k of 1 nm is producible in a laboratory setting, it is not feasible for standard manufacturing processes.

The microelectronics industry seems to be conscious of this problem. It is not surprising, actually, that John Mestemacher, marketing manager for emerging materials at Air products & Chemicals, notes that hafnium-based dielectrics were first expected to debut with the 65-nm generation of computer chips and then with the 45-nm generation. Now, based on the state of development at Air Products' customers, Mestemacher expects the industry won't adopt them even at 45 nm. More recently, on October 2005, David Lammers from INTEL, on Eetimes online, said: "It now appears extremely doubtful that high-k oxides can be inserted into the 45-nm node". IBM's Paul Agnello, manager of its 45-nm high-performance device and integration program, said "Threshold voltage scattering is a killer…. the high-k community needs to further improve before high-k oxides can be introduced into manufacturing".

APPENDIX A

We consider a flat interface between 2 media and a light beam passing through these 2 mediums as indicated in Figure A.1. The 2 media are transparent, homogeneous, isotropic and semi-infinite. The incidence plane is the one formed using the normal vector to the interface and the vector that describes the incident electromagnetic wave.

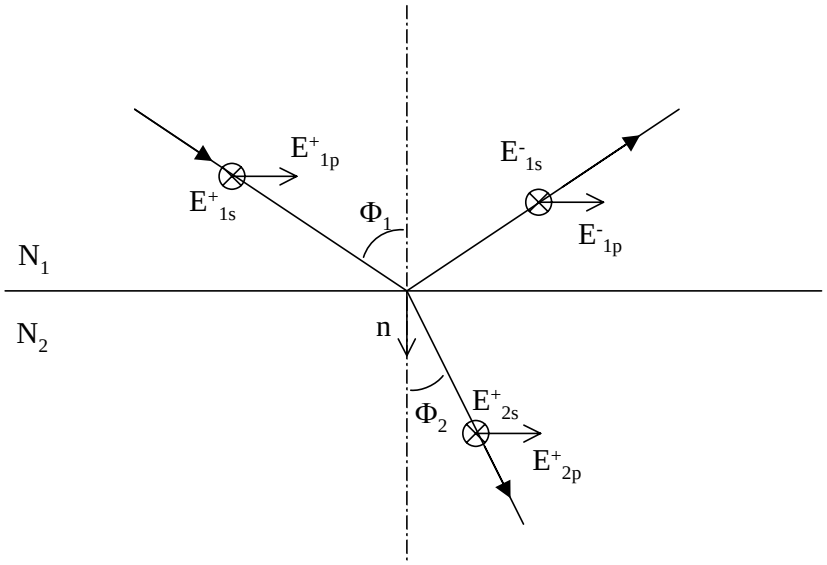

Figure A.1. *Light reflecting from and passing through an interface between a material (medium) 1 and material 2, respectively characterized with N_1 and N_2 refractive indices.*

The parameter we use to describe the interaction of light with the material is the complex index of refraction N, which is a combination of a real part and an imaginary part and is given as:

$$N_1 = n_1 + ik_1 \qquad \text{A.1}$$

$$N_2 = n_2 + ik_2 \qquad \text{A.2}$$

n is known as "the real part of the refractive index" or just "refractive index" and k is the extinction coefficient and is a measure of the absorbed light. Materials that are transparent to a certain frequency light have k = 0. Φ_1 and Φ_2 are respectively the angle of incidence and the angle of the of the transmitted electromagnetic wave

The law of reflection says that the angle of incidence is equal to the angle of reflection. The part of the light beam that enters in the material at an angle Φ_1 does not continue in the same direction, but it is refracted with a different angle Φ_2. The law of refraction is named after Snell and Descartes's and is given by:

$$N_1 \sin\Phi_1 = N_2 \sin\Phi_2 \qquad \text{A.3}$$

Two different reflection indices, also known as Fresnel indices, are defined: r_{12p} is associated with the value of the parallel electric field and r_{12s} is associated with the perpendicular electric field of the wave respects to the incidence plan. Their expression is given by equations A.4 and A.5.

$$r_{12p} = \frac{E_{1p}^-}{E_{1p}^+} = \frac{N_2 \cos\Phi_1 - N_1 \cos\Phi_2}{N_2 \cos\Phi_1 + N_1 \cos\Phi_2} \qquad \text{A.4}$$

$$r_{12s} = \frac{E_{1s}^-}{E_{1s}^+} = \frac{N_1 \cos\Phi_1 - N_2 \cos\Phi_2}{N_1 \cos\Phi_1 + N_2 \cos\Phi_2} \qquad \text{A.5}$$

which can also be written as:

$$r_{12p} = \left|r_{12p}\right| \exp(i\delta_p) \qquad \text{A.6}$$

$$r_{12s} = \left|r_{12s}\right| \exp(i\delta_s) \qquad \text{A.7}$$

We now define ρ as the ratio between the Fresnel coefficients:

$$\rho = \frac{r_{12p}}{r_{12s}} = \tan\Psi \cdot \exp(i\Delta) \qquad \text{A.8}$$

where

$$\tan\Psi = \frac{\left|r_{12p}\right|}{\left|r_{12s}\right|} \qquad \text{and} \qquad \Delta = \delta_p - \delta_s \qquad \text{A.9}$$

Ψ is the angle whose tangent is the ratio of the magnitudes of the total reflection coefficients and its value can be from 0 to 90°. Δ is the change in phase differences that occurs upon reflection and its value can be from 0 to 360°.

Using equations A.3, A.4, A.5 and A.6, we obtain the expression required to calculate the index of refraction of the medium 2:

$$\frac{N_2}{N_1} = \sin\Phi_1 \sqrt{1 + \left(\frac{1-\rho}{1+\rho}\right)^2 \tan^2\Phi_1} \qquad \text{A.10}$$

Obviously if N_1 and Φ_1 are known, N_2 can be easily calculated.

Ψ and Δ are the quantities measured by the ellipsometer and information about the sample are contained in the Fresnel indices. The model used in this chapter is a semi-infinitive medium. In chapter I.1.3.1 we have seen a real example. The measured quantities of Ψ and Δ in both cases will be correct, but if we apply the wrong geometry, the model will lead to wrong values for n and k.

APPENDIX B

Stretching: Change in the inter-atomic distance along the bond axis

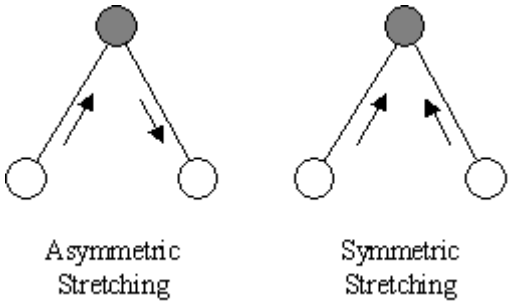

Bending: Change in angle between two bonds. There are four types of bend:

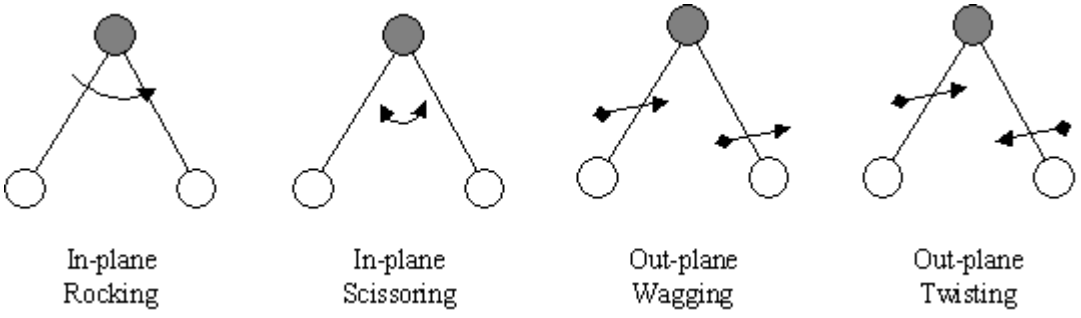

Figure B.1. *Representation of stretching and bending vibrations for a tri-atomic molecule.*

A molecule consisting of n atoms has a total of 3n degrees of freedom, corresponding to the Cartesian coordinates of each atom in the molecule. In a non-linear molecule 3 of these degrees are rotational 3 are translational and 3 correspond to the fundamental **vibrations.** In a linear molecule 2 degrees are rotational and 3 are translational. So for example the CO_2 molecule is linear and has 4 (3n-5) possible vibrations.

The asymmetric stretching modes are typically the most intense modes in IR spectroscopy because it requires more effort to change the symmetric relative positions of the atoms in the

molecule. Hooke's law can be used to approximate the stretching frequency of a bond. In this approximation, two atoms and the atomic bond are treated as a simple harmonic oscillator composed of 2 masses (atoms) joined by a spring.

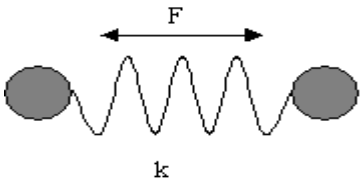

Figure B.2. *Schema of a simple harmonic oscillator.*

According to Hooke's law the frequencies of vibration of the spring are related to the force constant of the spring k by the following relationship:

$$\nu = \frac{1}{2\pi}\sqrt{\frac{k}{m}} \qquad \text{B.1}$$

Where m is the mass of the atom and ν is the frequency of the vibration. In the classical harmonic oscillator the energy of the oscillation is $E = 1/2\ kx^2 = h\nu$ where x is the displacement of the spring. The vibrational motion of a molecule is due to the phonons, thus is quantized. From quantum mechanics:

$$E = h\nu\left(n + 1/2\right) \qquad \text{with} \qquad n = (1,2,3,....) \qquad \text{B.2}$$

where n is the fundamental quantum number. The difference between the quantum oscillator and the classical oscillator then that: the phonons can interact and be absorbed only for certain vibrational frequencies of the molecule: and those frequencies should be determined by Eq. B.2.

There are some selectivity rules, which forbid some of the vibrational modes to be IR active. In order for a mode to have an allowed IR transition, the mode must involve a change in the electric dipole moment of the molecule: if the mode is associated with a time varying dipole, the mode can interact with infrared electromagnetic energy to produce a vibrational energy transition. A permanent dipole moment is *not* required.

In a diatomic molecule the equation B.1 becomes:

$$\nu = \frac{1}{2\pi c}\sqrt{\frac{f\left(m_1 + m_2\right)}{m_1 m_2}} \qquad \text{B.3}$$

Where ν is the vibrational frequencies expressed in cm^{-1}, m_1 and m_2 are the masses of the 2 atoms of the diatomic molecule and c is the velocity of the light. Eq. B.3 shows the relationship between the atomic mass, the bond strength and the wavenumber at which a molecule will absorb IR radiation. As the force constant f increases, the vibrational frequencies increase and the wavenumber also increases. This equation is for diatomic molecules but is also valid for more complex structures. Any time we want to consider a vibration between a very heavy atom bonded to a light atom, the heavy atom can be considered "as static" and only the light atom is allowed to have small movements (vibrations) with respect to the center of mass. This is possible because the center of mass is very close to the heavy atom. For example in La_2O_3 or $LaAlO_3$, the stretching of the oxygen compared to the La can be expressed by the Eq. B.3.

It is empirically possible to determine the force constant using a different model. If we apply Eq. B.3 to a Columbic model (the magnitude of the force is inversely proportional to the square of the distance betweens the atoms), we can estimate the frequency of the vibration within 20% of the measured value.

APPENDIX C

In order to understand the diffraction patterns and the various terms used it is now necessary to introduce some geometrical rules to identify the crystal structure as different faces or polyhedral planes composing a crystal. First we take a geometrical orthorhombic ternary of axis XYZ or **crystal axes** and for each axis we define the fundamental vector unit (or **crystal units**) **a**, **b**, **c**. This space is the lattice space. In the XYZ space we can trace the position of the atoms or the molecule, as is represented by small circles in Figure C.1.

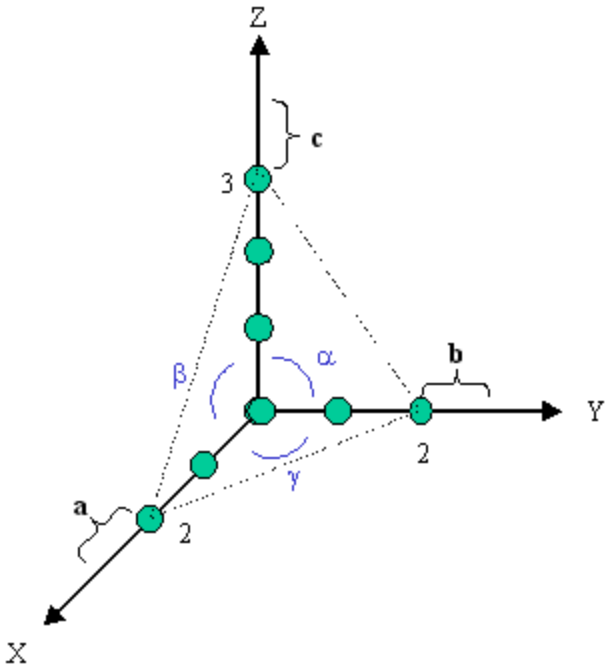

Figure C.1. *Crystal axes, atom or molecule positions in a crystal lattice space XYZ. The dotted line represents one of the possible lattice faces.*

The fundamental units are chosen arbitrarily for each crystal using a plane, which intercepts all XYZ axes.

A single plane is so define using the fundamental vector (dotted line in Figure C.1). Once the choice of the unit plane is made, due to the symmetry and the periodicity of the crystal, the equation of all other planes is given by:

$$m\vec{a} + n\vec{b} + p\vec{c} = \cos t \qquad \text{C.1}$$

where m, n and p are integer and are the intercepts on the axes. These 3 numbers can have values up to infinity, which is troublesome in certain mathematical calculations. For this reason we define the Miller indices as

$$h \propto \frac{1}{m}, k \propto \frac{1}{n}, l \propto \frac{1}{p} \qquad \text{C.2}$$

so that if m, n or p tends to infinity the Miller indices h, k or l have the value of zero. The Miller indices are integers without a common divisor. For example, referring to Figure C.1 the plane that intercepts the axes in 2, 2 and 3 is defined in the lattice space as [2a, 2b, 3c]. In the reciprocal axes its equation is [1/2, 1/2, 1/3]. The common divisor is 6, so that the Miller indices that identify that plane are (332). It must be remembered that the crystal axes are axes of reference, hence they extend in both negative and positive directions from the origin.

It is now evident that if we know the distances of the atoms (or the molecule) from the origin we can assign a better physical meaning to the a, b and c crystal unit. For Miller indices (hkl) the distance between the origin of the axes to the plane is d_{hkl} and its expression depends with the crystal symmetry. In Table C.1 we give the mathematical expressions of d for some crystal geometries.

Table C.1. *Formula for calculating interplanar spacings d_{hkl} for some common crystal geometries.*

Crystal geometry	d_{hkl}	Axial translation and angles
Cubic	$\frac{a}{\sqrt{h^2+k^2+l^2}}$	$a = b = c$ $\alpha = \beta = \gamma = 90°$
Tetragonal	$\frac{1}{\sqrt{\frac{h^2}{a^2}+\frac{k^2}{a^2}+\frac{l^2}{c^2}}}$	$a = b \neq c$ $\alpha = \beta = \gamma = 90°$
Orthorombic	$\frac{1}{\sqrt{\frac{h^2}{a^2}+\frac{k^2}{b^2}+\frac{l^2}{c^2}}}$	$a \neq b \neq c$ $\alpha = \beta = \gamma = 90°$
Rhombohedral	$\frac{1}{\sqrt{\frac{4a^2}{3}\left(h^2+k^2+hk\right)+\frac{l^2}{c^2}}}$	$a = b \neq c$ $\alpha = \beta = 90°, \gamma = 120°$

The Miller indices have no physical meaning but they are introduced to explain the concept of the "**Reciprocal Lattice**" [Ewald]. The reciprocal lattice is just a geometrical aid with no physical meaning. The great utility of the concepts lies in the ease with which it permits the investigator to visualize the crystal planes, their slope and their spacing.

In Figure C.2 we show how to graphically generate the reciprocal lattice for a monoclinic crystal.

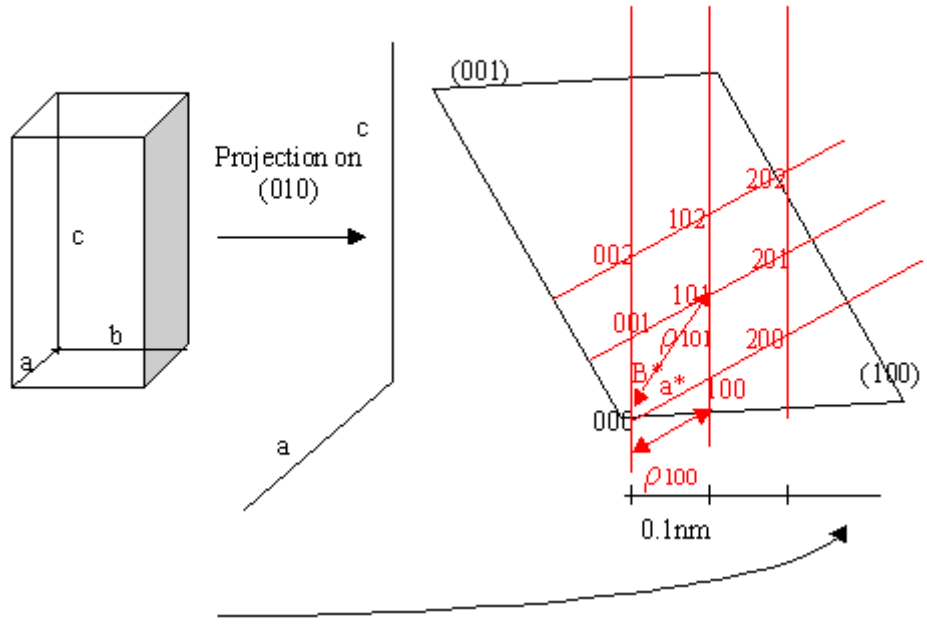

Figure C.2. *Projection of a simple monoclinic lattice on (010) and a portion of its reciprocal lattice (red).*

The relation between the reciprocal space and the lattice space is given by the equation C.3:

$$\rho = \frac{k^2}{d_{hkl}} \qquad \text{C.3}$$

where k is a constant and ρ is the distance from the origin in the reciprocal lattice. Typically k^2 is equal to λ, the wavelength of the **incident x**-ray beam.

NB: the real lattice is given by the a, b and c primitive translation and the ternary that identify the translation (ma,nb,pc) is a plane. The ternary that identifies that plane in the reciprocal lattice is the (hkl) (the Miller indices) and is a single point.

a) the Bragg equation for the real lattice

The easiest interpretation of the x-ray diffraction in terms of reflection was given by Bragg. Bragg considered a crystal formed by a stack of parallel atomic planes and an electromagnetic wave of a certain intensity and wavelength λ incident on those planes with a certain angle θ.

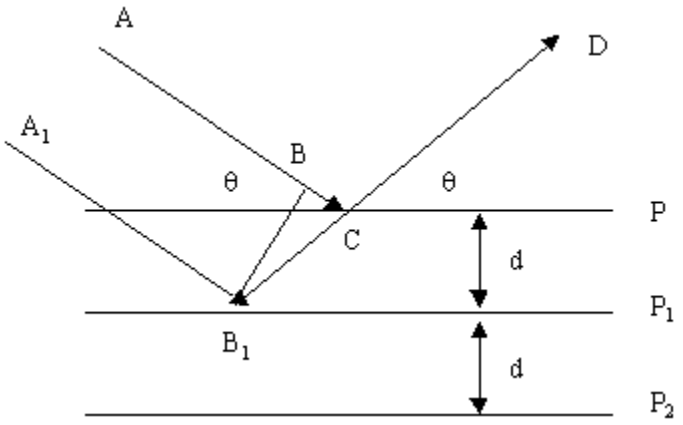

Figure C.3. *Geometry of Bragg* ***reflection.***

In Figure C.3 we consider the planes p, p_1, p_2 and so on to represent a stack of planes with a constant interplanar spacing d. AB, A_1B_1 is the array of incident x-rays which are reflected off in the direction CD. For the reflected wavelet from B_1 to reinforce the one reflected at C it must arrive at C in phase with the wave ABC. This will be the case if the path difference is a whole number of wavelengths, that is, if

$$B_1C - BC = \frac{d}{\sin\theta} - \frac{d}{\sin\theta}\cos 2\theta = n\lambda \qquad \text{C.4}$$

which becomes, using simple trigonometry, the most common Bragg equation or Bragg law [Alonso].

$$n\lambda = 2d\sin\theta \qquad \text{C.5}$$

For a crystal of a given d spacing and a given wavelength λ, the various orders n of reflection occur only at the precise value of θ which satisfies equation I.33. Similarly results are obtained when considering an electron beam or a neutron beam.

b) the Bragg equation for the reciprocal lattice

As we said earlier, x-ray diffraction cannot be explained or demonstrated using the reciprocal space because this space has no physical meaning. However, it is possible to rearrange Eq. C.5 using the Miller indices and give the expression of the Bragg law in the reciprocal space.

$$\sin\theta_{(hkl)} = \frac{\lambda}{2d_{(hkl)}} \qquad \text{C.6}$$

An interesting result is now obtained by substituting the value of $d_{(hkl)}$ from Eq. C.4 in Eq. C.6 including also the substitution $k^2 = \lambda$:

$$\sin\theta_{(hkl)} = \frac{\rho_{(hkl)}}{2} \qquad \text{C.7}$$

For each plane (hkl) the Bragg angle θ is an angle whose sine is equal to half its ρ value. Because the sin can have values between – 1 and 1, ρ cannot exceed the value of 2. This means that no point outside a sphere of radius 2 around the origin can ever give a reflection for a given wavelength so that some conditions are necessary in order to obtain diffraction from a (hkl) plane.